ALMA MATER STUDIORUM
UNIVERSITÀ DI BOLOGNA

DOTTORATO DI RICERCA IN

SCIENZE E TECNOLOGIE DELLA SALUTE

Ciclo XXXVII

Settore Concorsuale: 05/H2 – Istologia

Settore Scientifico: BIO/17 – Istologia

Design Synthetic 3D Scaffold for Skeletal Muscle Tissue Differentiation

Presentata da: ***Serafina Pacilio***

Coordinatore Dottorato:
Prof. Igor Diemberger

Supervisore:
MED: Prof. Giovanna Cenacchi
Co-supervisore:
TECH: Prof. Maria Letizia Focarete
MED: Prof. Francesco Alviano

Esame finale anno 2025

Abstract

Skeletal muscle (SKM) loss is largely irreversible, and current therapeutic options to restore muscle mass remain limited. Despite the regenerative capacity of SKM due to resident satellite cells, *in vitro* and *in vivo* studies using stem cells have shown low regenerative and self-renewal properties. Conventional 2D monolayer culture systems, commonly used for myoblast expansion and maintenance, fail to replicate the *in vivo* environment due to the lack of cell-cell and cell-matrix interactions, often resulting in misleading outcomes. New strategies are needed to address the limitations of current tissue repair and regeneration methods. Tissue engineering (TE) has emerged as a promising approach for SKM tissue renewal both *in vitro* and *in vivo*. TE combines scaffolds, cells, and regulatory signals to create a temporary biomimetic extracellular matrix (ECM), supporting cell attachment and proliferation. In this study, we evaluated a poly (L-lactic acid)-co-poly-(ε-caprolactone) (PLCL) electrospun scaffold coated with type I collagen to support SKM fabrication *in vitro*, focusing on its role during myogenesis. While several studies have explored the utility of electrospun scaffolds in SKM development, we examined the specific factors influencing myoblast behavior and differentiation in response to the external environment. Our results demonstrated that the PLCL scaffold supported myoblast attachment, elongation, and myotube formation, offering new insights into the development of 3D tissue-like structures. To further investigate SKM functionality, we employed Atomic Force Microscopy (AFM) to monitor real-time contractile activity on the PLCL scaffold, simulating the excitation-contraction coupling mechanism observed in SKM. This novel approach provided a more accurate representation of SKM physiology. Additionally, we developed a 3D bioprinted scaffold using collagen as the primary ECM component, along with laminin and fibronectin, to mimic the native SKM environment. This model allowed us to investigate the differentiation of myoblasts from both healthy (CTRL) and Limb-Girdle Muscular Dystrophy Type D2 (LGMDD2) conditions, using conventional techniques and omic approaches to analyze gene and protein expression. In particular, we studied the role of Myogenic Regulatory Factors (MRFs) and MEF2C isoforms, as well as splicing factors like SRSF1 and RBM4, which are cargoes of the TNPO3 protein involved in LGMDD2 pathology. Finally, to assess SKM contractility in LGMDD2, we utilized a micropillar system to measure muscle contraction dynamics. This platform revealed early-stage alterations in cell differentiation, highlighting functional impairments caused by TNPO3 mutations that affect myogenic commitment and SKM functionality. Our findings underscore the utility of TE-based models not only in advancing our understanding of skeletal muscle (SKM) development but also in elucidating the pathogenic mechanisms underlying muscle disorders, particularly LGMDD2. By

employing PLCL electrospun scaffolds and 3D bioprinted matrices in conjunction with real-time functional assays, such as Atomic Force Microscopy (AFM) and micropillar systems, we developed a physiologically relevant platform that replicates *in vivo* SKM architecture and functionality. Future analyses and studies will focus on further characterizing our TE models to gain a deeper understanding of both SKM development and LGMDD2 pathology. Given the significant unmet clinical need for effective treatments in LGMDD2, our 3D model presents a valuable tool for investigating drug repurposing and high-throughput screening, offering a cost-effective and ethically sound alternative to traditional models. By refining these TE platforms, we aim to establish a robust framework for targeted therapeutic exploration, ultimately contributing to the advancement of accessible and efficient approaches for addressing muscular dystrophies.

INDEX

Introduction

Striated Skeletal Muscle Anatomy

Skeletal muscle, the most abundant tissue in the human body, is essential for maintaining posture, generating movement, and contributing to energy homeostasis. Striated skeletal muscle, which comprises 35% to 45% of total body mass (Dumont et al., 2015), exhibits notable plasticity and regenerative potential. The regenerative capacity is mediated by satellite cells, a population of muscle stem cells critical for muscle repair and renewal (Motohashi et al., 2014). Through these mechanisms, skeletal muscle plays a pivotal role in both mechanical function and metabolic regulation (Frontera & Ochala, 2015; Gillies and Lieber, 2011; Zhang et al., 2021). Skeletal muscle is a highly structured tissue composed of bundles of multinucleated muscle fibers, known as myofibers, and associated connective tissue. The entire muscle is encased in a layer of connective tissue called the epimysium, while fiber bundles within the muscle are surrounded by the perimysium. A single muscle fiber, measuring approximately 100 μm in diameter and 1 cm in length, is enclosed by the sarcolemma, the plasma membrane of the muscle cell. The muscle fiber contains thousands of myofibrils, which are made up of billions of myofilaments. These myofilaments form the sarcomere, the basic contractile unit of skeletal muscle. (FIG.1). Skeletal muscle fibers are also characterized by their metabolic heterogeneity, allowing the distinction between white and red fibers. Slow-red type I fibers are rich in mitochondria and myoglobin, enabling prolonged contraction, while fast-white type II fibers are larger, with fewer mitochondria and myoglobin, capable of fast and intense contractions (Frontera and Ochala, 2015).

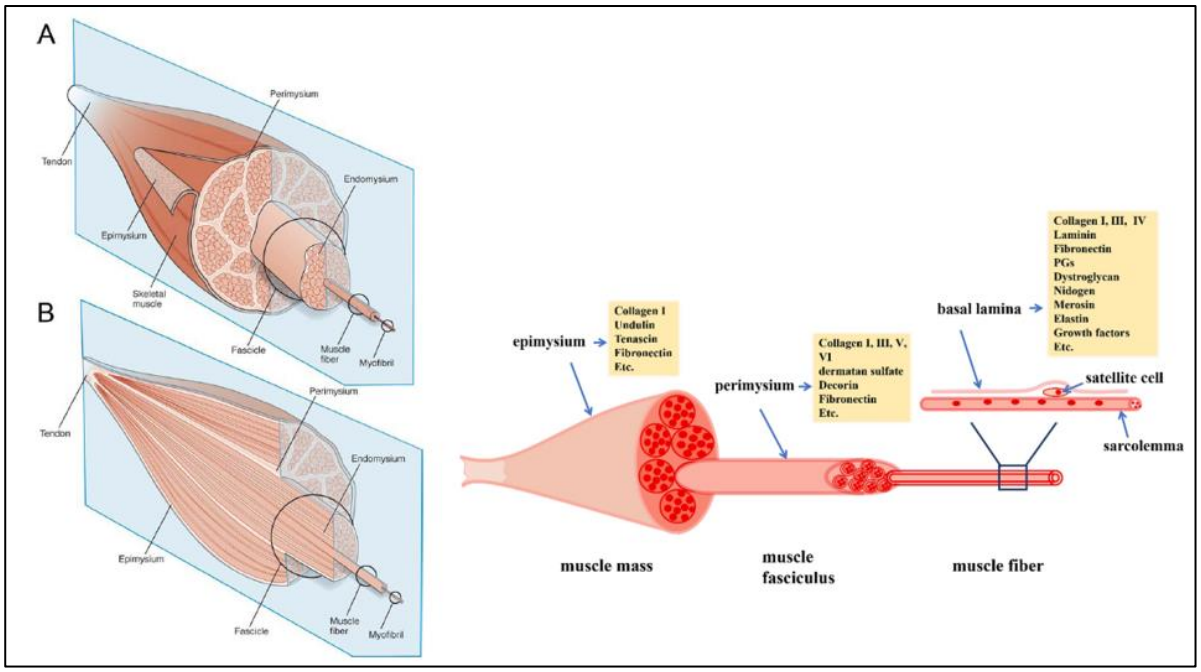

Figure 1. Schematic diagram of the gross organization of muscle tissue and muscle ECM–tendon organization. (A) Muscle ECM can be categorized as epimysium (surrounding the muscle), perimysium (surrounding muscle fascicles), and endomysium (surrounding muscle fibers). (B) Cross-section of muscle tissue indicating that the perimysium may be continuous with the tendon, whereas endomysium is contained within the muscle fascicles (Gillies and Lieber, 2011). (C) Skeletal muscle ECM three-layer structure diagram (Zhang et al., 2021).

The extracellular matrix (ECM) is a non-cellular macromolecular network made up of collagens, glycoproteins, proteoglycans, and elastin, providing physical scaffolding and biomechanical cues necessary for tissue homeostasis, morphogenesis, and differentiation (Frantz et al., 2010). The ECM regulates muscle formation, growth, and repair through interactions with other cells such as fibroblasts and immune system cells. It supports cell-matrix interactions that are fundamental for muscle cells to adapt to their microenvironment. Collagen and proteoglycans are the two main structural proteins that interact to maintain the structure and organization of the matrix. Collagen accounts for 1-10% of the ECM and is involved in forming large fibrillar structures, creating a three-dimensional network that maintains the structural organization of the matrix (Theocharis et al., 2016). Collagen types I, III, IV, V, VI, VIII, XI, XII, XIV, XV, and XVIII are expressed during skeletal muscle development, with types I and III being the most abundant, accounting for approximately 75% of total muscle collagen (Kovanen, 2002) (FIG.2). In normal skeletal muscle, enzymes responsible for ECM synthesis and their inhibitors are finely balanced. Matrix metalloproteinases, which are multidomain enzymes responsible for the catabolism of nearly all ECM molecules, play a crucial role in the turnover of the ECM, which is necessary for cell

migration, matrix reorganization, and myotube formation during muscle adaptation (Gillies and Lieber, 2011; Vihinen and Kähäri, 2002).

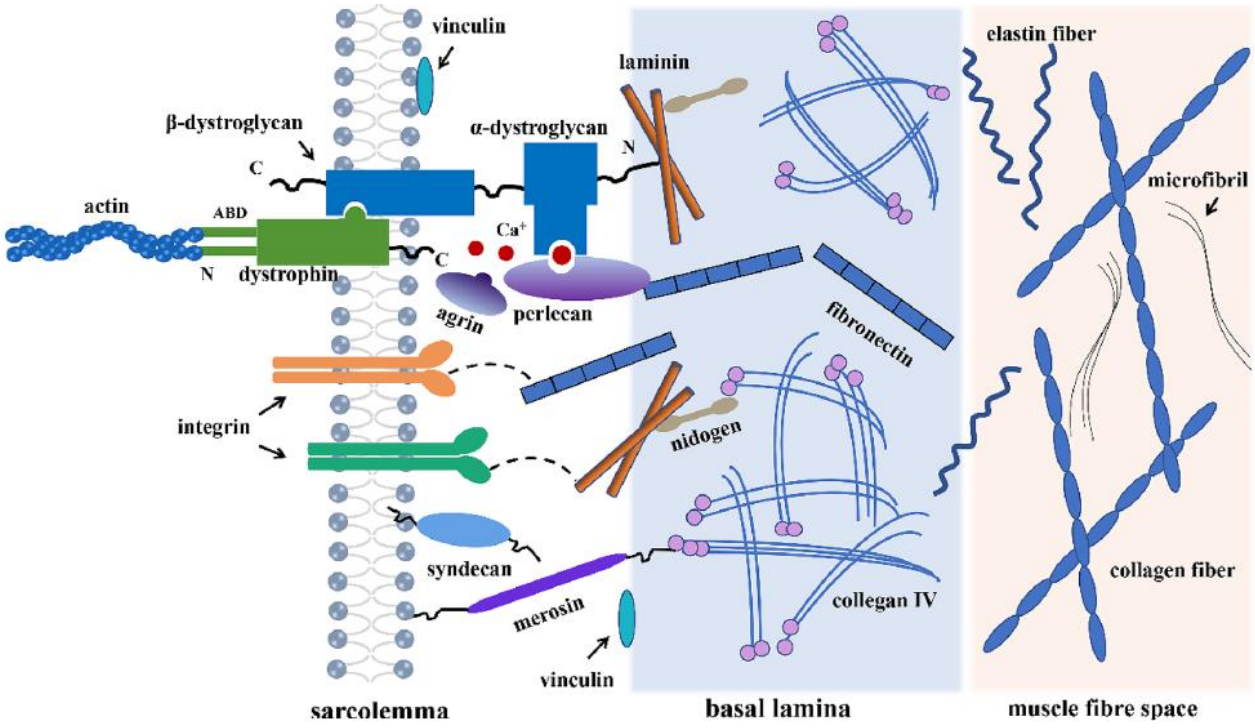

Figure 2.Ultrastructural diagram of extracellular matrix of skeletal muscle (Zhang et al., 2021).

Muscle fibers are organized into myofibrils, which are characterized by their cross-striation visible under the optical microscope. Myofibrils are composed of thick filaments made of myosin and thin filaments made of actin. Actin and myosin are the two most numerous myofilaments involved in muscle contraction. Regulatory proteins include tropomyosin and the calcium-dependent troponin complex, while mechanical support and sarcomere integrity are provided by titin and nebulin proteins. Additionally, proteins such as desmin link the Z disk to the sarcolemma and the ECM (Mukund and Subramaniam, 2020) (Figure.3)

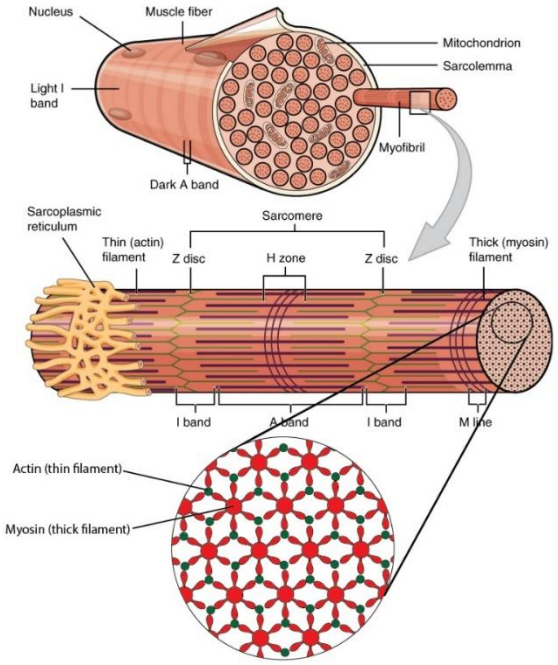

Figure 3. Skeletal muscle organization.

The contraction of skeletal muscle is triggered by a nervous stimulus. When an action potential occurs, the synaptic terminations release acetylcholine that binds to its receptors on the sarcolemma, leading to depolarization. This depolarization propagates inside the muscle fiber, inducing the release of calcium ions that break the bond between troponin and actin, allowing myosin heads to bind actin and initiate contraction. The process continues as long as the stimulus is present. Once the stimulus ends, the sarcolemma returns to its resting potential, calcium ions are sequestered by the endoplasmic reticulum, and tropomyosin blocks the actin-myosin bond to end the contraction (Figure 4)

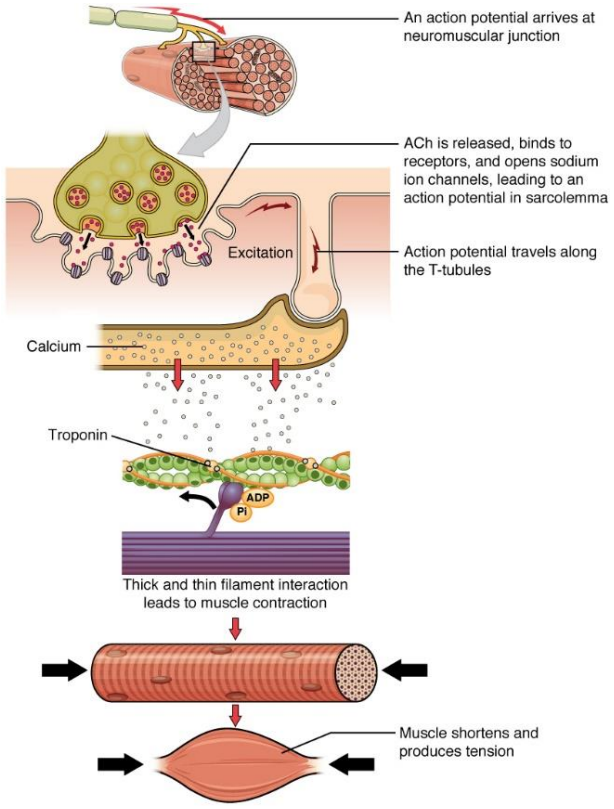

Figure 4. Muscle contraction illustration.

Myogenesis

Myogenesis is the process through which myogenic precursors differentiate into skeletal muscle fibers, beginning as early as the first week of embryonic development. This complex process unfolds in two distinct phases: an early embryonic phase and a later fetal phase (Tajbakhsh, 2009; Hernández et al., 2017). Myogenesis starts from somites, segmental structures of the paraxial mesoderm that line the neural tube and the notochord. Somites are divided into sclerotome and dermomyotome under the influence of signaling molecules such as Sonic Hedgehog (Shh), Wingless-related integration site (Wnt), and bone morphogenic protein (BMP) (Chal et al., 2017; Hernández et al., 2017). The dermomyotome, the dorsal portion of the somite, contains totipotent, fusiform, and mononucleate mesenchymal cells that serve as embryonic myogenic progenitors. These progenitors express the paired box transcription factors Pax3 and Pax7 and are regulated by muscle regulatory factors (MRFs), which include Myf5 (Myogenic factor 5), MyoD (Myoblast determination protein 1), MRF4 (Myogenic Regulatory Factor 4), and MyoG (Myogenin) (Buckingham and Rigby, 2014; Hernández et al., 2017). Pax3 and Pax7 are upstream regulators crucial for initiating myogenesis. Pax3 is essential for activating the expression of MRFs and determining embryonic skeletal myogenicity, while Pax7, although not essential for embryonic

muscle development, maintains muscle stem cells known as satellite cells (Seale et al., 2000; Rudnicki and Jaenisch, 1995). During early myogenesis, the dermomyotome gives rise to the myotome, which is composed of cells that express Myf5 and downregulate Pax3. These cells migrate and differentiate into mononucleated myocytes under the control of MyoG and MRF4 (Braun et al., 1989). In contrast, Pax3/Pax7-expressing stem cells trigger myotome formation from the central region of the dermomyotome, contributing to primary myofiber formation (Relaix et al., 2005). MyoD largely overlaps with Myf5 expression, further contributing to myotome formation and activating MRFs (Chal et al., 2017). Later, MyoD and MRF4 guide myoblast fusion into primary multinucleated myofibers, with MyoG playing a crucial role in this process (Moncaut et al., 2013; Zammit, 2017) (Figure 5)

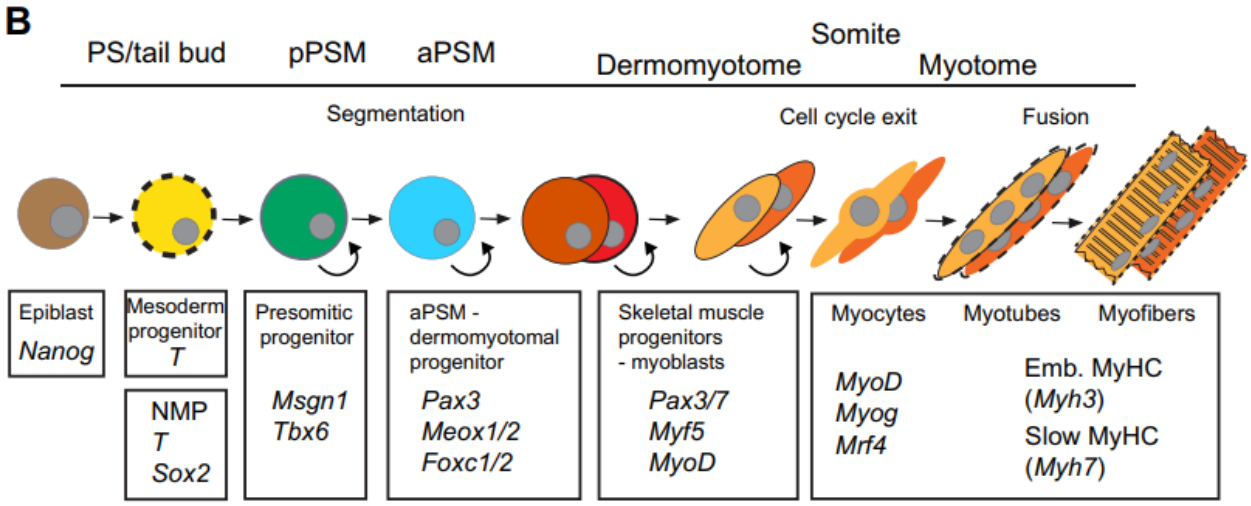

Figure 5. Schematic representation summarizing the differentiation of paraxial mesoderm toward skeletle muscle. From left to right, the intermediate cell types withe either marker genes (bottom) and the developmental sequence are represented. aPSM, anteriorpresomitic; pPSM posterior presomitic mesoderm; EMB, embryonic (Chal et al; 2017)

In the fetal phase of myogenesis, myoblasts either merge with existing primary myofibers or generate new secondary myofibers (Kozeka and Ontell, 1981). This phase involves a shift in the expression of MRFs, where MyoD, Myf5, and MRF4 act as myogenic determination factors, while MyoG regulates myoblast differentiation (de la Serna et al., 2005). MyoG and MRF4 are directly involved in the differentiation process, triggering the expression of myotube-specific genes, while MRFs can stimulate their own expression and that of MEF2 (Myocyte Enhancer Factor 2) proteins (Edmondson, 1994). MEF2 is central to the later stages of myogenesis, although it does not exhibit myogenic activity alone but rather amplifies differentiation through a feed-forward loop involving

bHLH genes like MyoG (Sandmann et al., 2006). Transcription factors involved in myogenic lineage progression operate through complex feedback and feed-forward networks. Initially, MRFs directly activate certain genes, which later require the involvement of earlier target gene products for their induction (Berkes and Tapscott, 2005). Furthermore, Myf5 represents the ancestral gene of the MRF family, with Myf5, MyoD, MRF4, and MyoG evolving through gene duplications to regulate myogenesis (Hernández et al., 2017). In the early embryonic phase, primary myofibers are produced and express slow Myosin Heavy Chain (MyHC) and Myosin Light Chain 1 (MyLC1). In the later fetal phase, Pax3-expressing progenitors start to express Pax7, downregulating Pax3, and fibers shift to express fast MyHC (Zammit, 2017) (Figure 6).

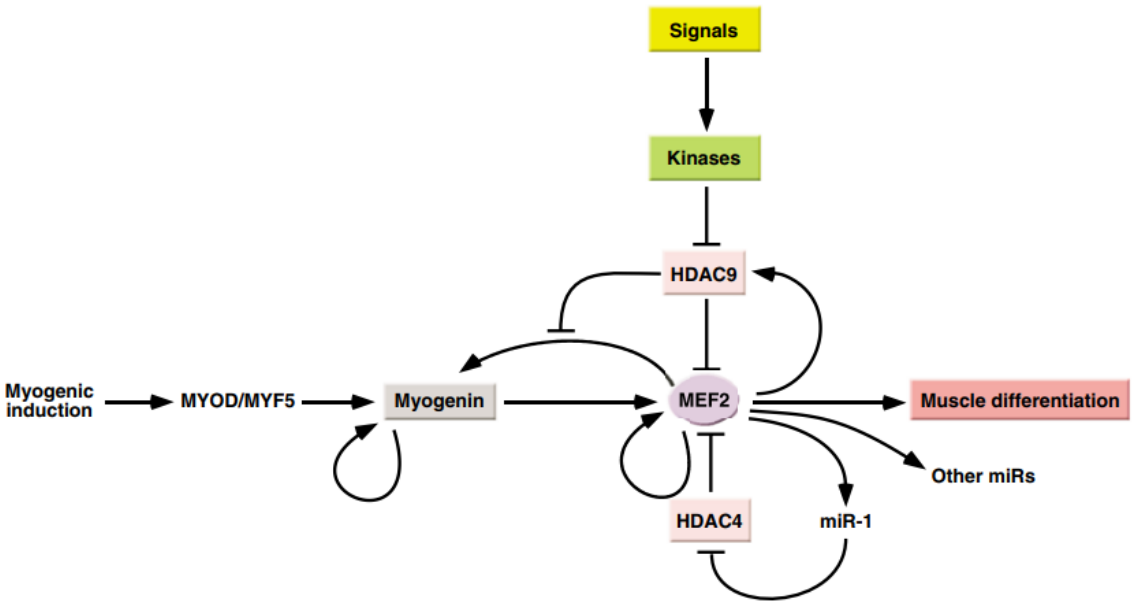

Figure 6. Graphic representation of a complex regulatory network involved in mammalian skeletal myogenesis, where inductive signals activate a series of transcription factors, feedback loops, and microRNAs to control muscle differentiation, maintaining a balance between positive and negative regulatory elements, in which HDAC9, HDAC4 and MEF2 have a central role. (Potthoff and Olson; 2007).

Satellite cells

Skeletal muscle has an extraordinary regenerative capacity, primarily driven by satellite cells, a population of adult stem cells (Bentzinger et al., 2012; Dumont et al., 2015). Satellite cells reside between the basal lamina and the plasmalemma of muscle fibers, constituting 2% to 10% of the total myonuclei (Dumont et al., 2015). They originate during the final stages of embryonic myogenesis (Seale et al., 2001) and occupy a specialized microenvironment known as the "stem cell

niche." This niche provides biochemical and biomechanical signals from extracellular matrix (ECM) components such as laminins, fibronectin, and collagens, which support satellite cell functions, including self-renewal, proliferation, migration, and differentiation. (Figure 7)

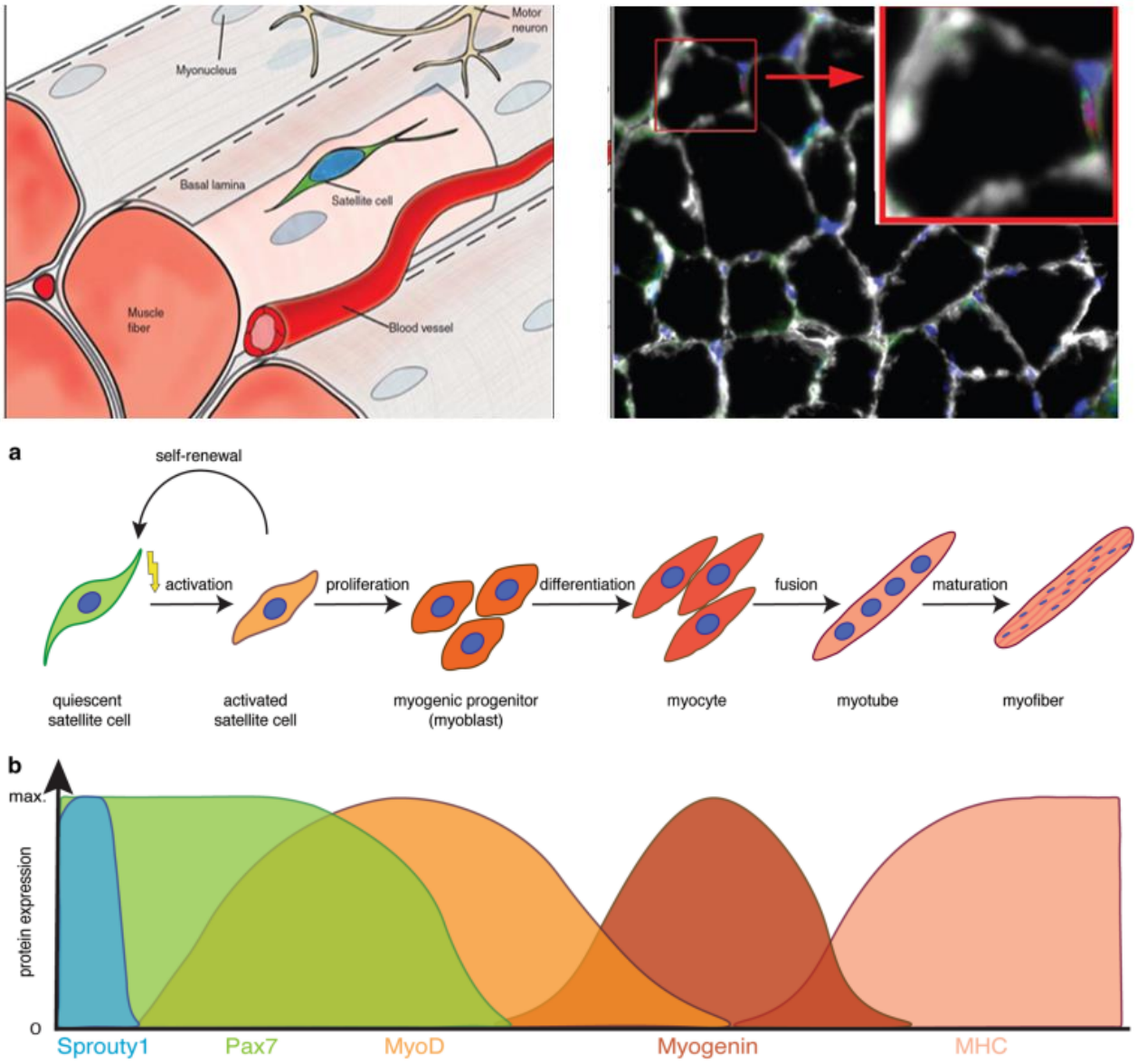

Figure 7. Myogenic lineage progression and expression profile of key myogenic regulators. 1 example of stem cells localization into muscle fiber (a) schematic illustration of the myogenic lineage progression. When satellite cells are activated start to proliferate, thus generating myogenic progenitor cells. Upon differentiation, myogenic progenitor cells differentiate into myocytes, which fuse to form myoutubes and mature into myofibers (b) Expression profile of key modulators of myogenic lineage progression (Schmidt et al; 20219)

In their quiescent state, satellite cells are characterized by a lack of cell cycling, low RNA content, and minimal metabolic activity. This state is maintained by Notch signaling, which inhibits satellite

cell activation (Dumont et al., 2015). Upon activation during muscle regeneration, satellite cells co-express Pax7 and MyoD, promoting differentiation into myocytes and eventually mature myofibers (Schmidt et al., 2019). Besides Pax7, other markers for satellite cells include Pax3, Myf5, M-Cadherin, VCAM1, CD34, and CALCR (Schmidt et al., 2019). The process of satellite cell self-renewal involves asymmetric cell division (ACD), a mechanism by which cellular components are unequally distributed between daughter cells during mitosis, determining their fate. Notch signaling, especially through Notch3 and Delta1, plays a key role in regulating ACD, along with the Par complex and p38α/β MAPK pathway, which controls MyoD transcription, thereby influencing satellite cell proliferation and commitment (Dumont et al., 2015).

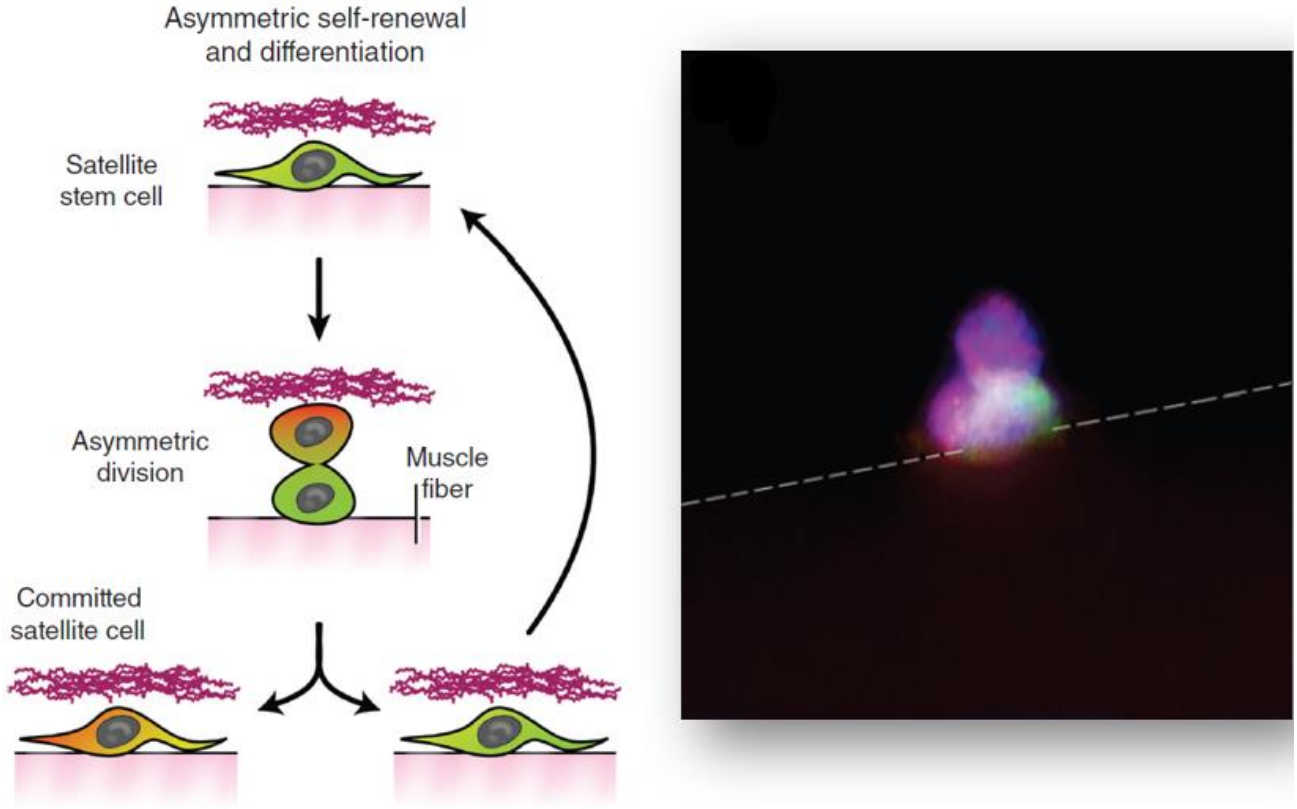

Figure 8. Asymmetric satellite cell division: apical-basal orientation (perpendicular to the myofiber). The daughter cell detached from the basal lamina up regulates Myf5 and the fluorescent lineage tracer YFP (green). Pax7 (red). Nuclei (blue, DAPI). The asymmetric self-renewal and differentiation allows the formation of one committed satellite cell that will participate in the myogenesis and one daughter stem cell for the maintenance of the original satellite stem cell (Dumont et al., 2015).

LGMDD2

Limb girdle muscular dystrophies are a group of heterogeneous disorders classified for the first time as a stand-alone clinical entity in 1954 (Angelini, 2020). In 2017, LGMD was redefined, leading to changes in the classification and naming of its subtypes based on inheritance pattern (D, dominant; R, recessive), the affected protein, and its order of discovery. Nowadays more than 30 different LGMDs subtypes have been identified, 5 autosomal dominant and 26 autosomal recessives (Georganopoulou et al., 2021). Overall, the prevalence of all LGMDs ranges from 1:14,500 to 45,000 depending on the geographical and ethnic origin (Nigro et al,2003; Norwood et al, 2009). The proposed definition of LGMD is a condition that primarily affects skeletal muscle, causing progressive, predominant muscle weakness and loss of muscle fibers, described in at least two unrelated families, with elevated CK levels and dystrophic changes in muscle histology. However, the clinical course and the expressivity may be variable, spanning from very mild forms to very rapid onset and severe ones. For each gene involved in LGMD hundreds of mutations have been identified, especially splice site, small deletions and missense mutations. (Nigro et al., 2011) Affected proteins in LGMD are located in the extracellular matrix, nucleus, sarcolemma and cytoplasm (Van Der Koi, 2017). The proteins involved perform three subcellular functions: glycosylation modification, mitochondrial dysfunction, and mechanical signaling (Barton et al., 2020). Glycosylation modification is associated with the signaling domain of the sarcoglycan complex. The functional cluster that relies on mitochondrial function includes proteins that may have a role in the activation of apoptosis pathways, calcium homeostasis and energy production: LGMD-causing genes are related to mitochondrial impairment, despite their role has not been elucidated yet. The third category includes proteins causing mechanical interference in skeletal muscle cells: MAPK proteins family, their phosphorylation pathway and in particular the sarcoglycan complex are emerging as key mechanosensors (Barton et al., 2020) (Figure 9). .

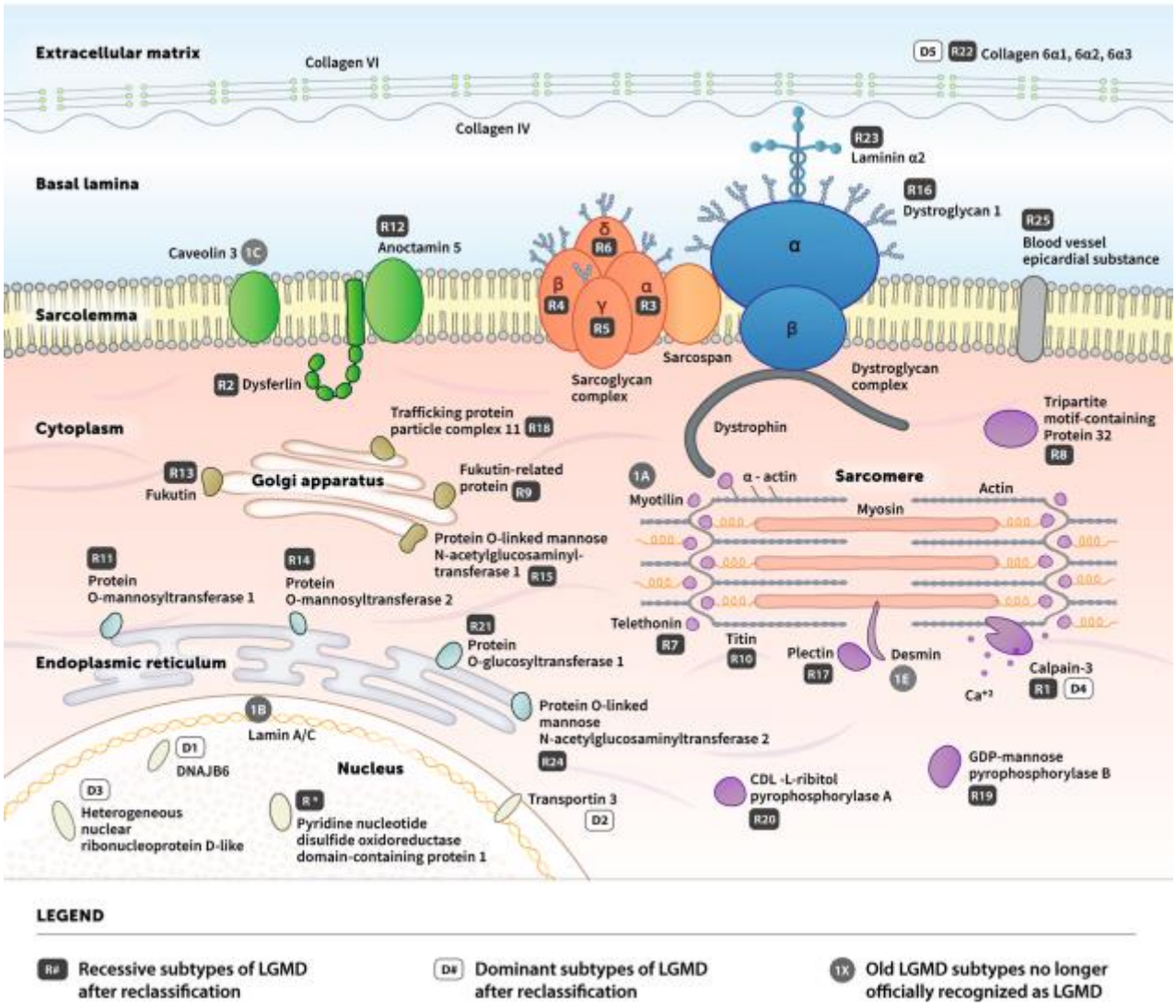

Figure 9. Schematic diagram of the different protein cellular localizations within the cytosol, nucleus and sarcolemma of myocites, each one related to a LGMD subtype. The top part of the diagram shows the extracellular space, including the ECM and basal lamina; the sarcolemma is in the middle; at the bottom, the nucleus and cytoplasm, including sarcomere, Golgi apparatus, and endoplasmic reticulum are located. (Georganopoulou et al., 2021)

LGMD D2 (1F)

Limb girdle muscular dystrophy type 1F or D2, is a rare LGMD subtype, first identified in an Italo-Spanish family in 2001 (Gamez et al., 2001). At present also other European families and 2 sporadic cases have been described. The gene responsible for the disease is located in the interval of 3.68 Mb on the novel chromosomal locus 7q32.1–32.2. (Torella et al., 2013) A whole genome sequencing approach enabled the identification of the causative mutation of the LGMDD2 in the termination codon of TNPO3, the gene encoding transportin 3. The pathogenic role of this mutation

was confirmed by morphological evidence as well as molecular results at DNA, RNA and protein level (Gibertini et al., 2018). Although there is proof of its presence in the skeletal muscle, its precise function is still unknown (Melià et al., 2013). Tnpo3 or Transportin-SR2 is implicated in translocation of splice regulators to the nucleoplasm, and HIV replication (Christ et al., 2008). Tnpo3 has several coding and non-coding transcript variants: the main one is NM_012470.4 and it encodes a protein of 923 amino acids long (NP_0366021) (Costa et al., 2022; Torella et al., 2013) identified two different spliced versions of a muscle gene, one (Figure 10, A) connecting exon 22 to exon 23 and the other (Figure 10, B) ending with exon 22, where the stop codon is located. A single nucleotide heterozygous mutation in the A form affecting the Italo-Spanish family causes the protein elongation by 15 amino acids (NM_012470.3: c.2771delA p.∗ 924Cext∗ 15 in exon 22). Form B may contain additional 95 amino acids. A Hungarian family carries a heterozygous frameshift variant [c.2767delC p. (Arg923AspfsTer17)] resulting in the same condition. The other European family, a Sweden one, is affected by a new heterozygous mutation (c.2757delC) whose consequence is a stop codon shifting. The final effect is nearly identical to the original TNPO3 mutation. A patient who was not familiar with neuromuscular disorders presented a heterozygous missense, so it is a sporadic case. A G>A heterozygous switch was found (c.G2453A) in exon 20. An arginine in position 818 is substituted with a glutamine in a highly conserved residue (Gibertini et al., 2018) (Figure 11).

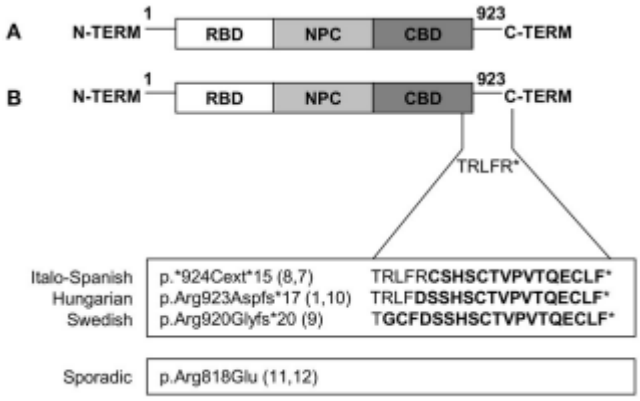

Figure 10. Graphic representation of wild-type TNPO3 protein showing the N-terminal RanGTP-binding domain (RBD), (A) C-terminal cargo-binding domain (CBD) and nuclear pore complex (NPC)-binding domain. (B). Graphic description of all described mutations (Costa et al; 2022)

The final impact of these mutations, except for the sporadic case, is final elongation of the protein C-terminal domain by 15 amino acids (Costa et al., 2022). TNPO3 wild type (WT) protein and the mutated one coexist, but the mutant form seems to have a dominant negative effect on the WT protein, altering its function as a transporter. The missense mutation is causing instead a reduction

in TNPO3 amount, modifying the messenger stability. These patients could extensively share the same pathological mechanism, though the variable onset and disease progression in time suggest the participation of several environmental and epigenetic modifiers that could highly influence it.

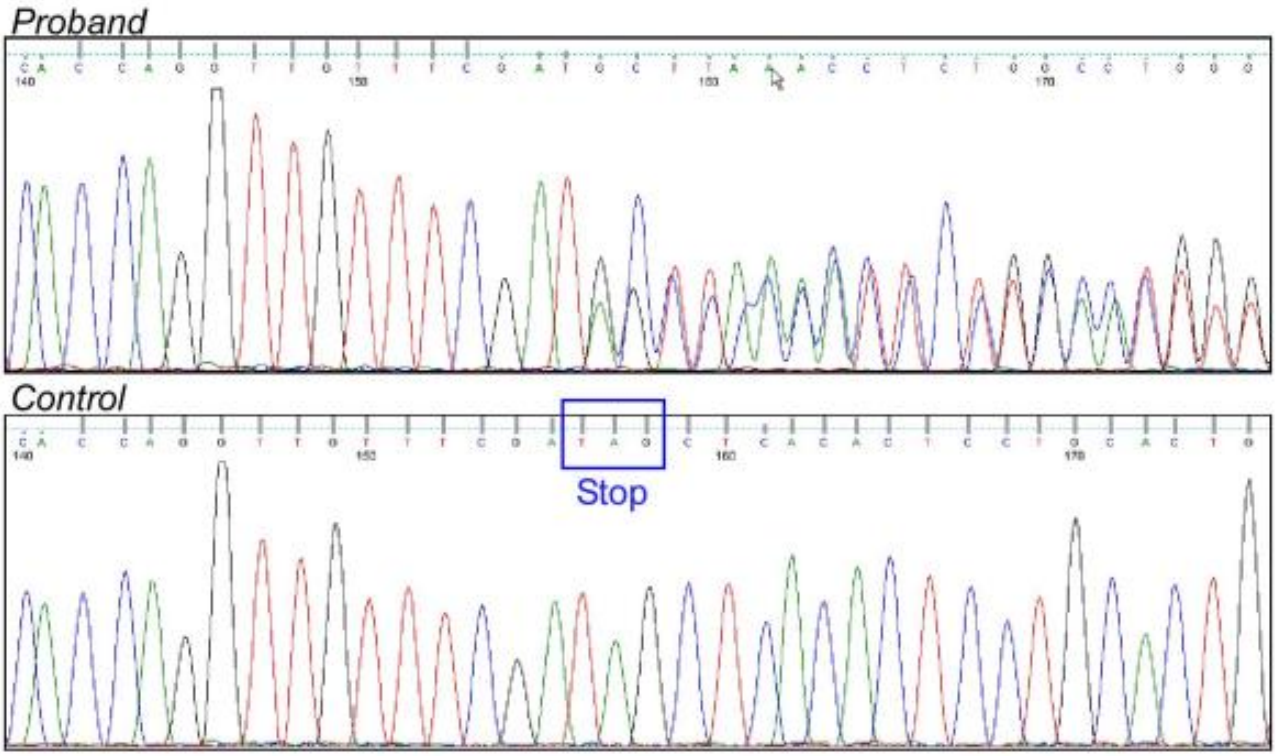

Figure 11. Heterozygous delA mutation in Exon 22 of the TNPO3 gene showed in the electropherogram (Torella et al., 2013).

TNPO3 function and its cargoes

Transportin-3 (TNPO3 or TNPO3-SR2) is a member of the importin-β superfamily, specifically the β-karyopherin protein family. In "S. cerevisiae", 14 members of this superfamily have been identified, with 9 functioning as importins and 4 as exportins (Görlich and Kutay, 1999). In mammals, over 22 members of this family are present. These proteins facilitate the translocation of their cargo through the nuclear pore complex (NPC) by binding to them. This process is regulated by the Ran GTPase, which exists primarily in its GDP-bound form in the cytoplasm and its GTP-bound form in the nucleus. Upon entry into the nucleus, Ran-GTP binds to importins, leading to the release of their cargo (Ström and Weis, 2001). Karyopherins recognize and bind their cargo by identifying specific tertiary or quaternary structures or a nuclear localization signal (NLS) (Cook et al., 2007). Nuclear localization signals (NLS) are sequences characterized by RS or RS-like

domains, consisting of Arg-Ser or Arg/Asp/Glu/Gly dipeptides, and are part of the Ser/Arg-rich (SR) protein family. These proteins also contain an RNA recognition motif (RRM), which is involved in mRNA processing, splicing, and transcriptional regulation. ASF/SF2, an SR protein encoded by the SRSF1 gene, functions as a critical splicing factor. SR proteins possess an RRM domain that undergoes phosphorylation on Ser residues by specific kinases (Aubol et al., 2003). The phosphorylation and dephosphorylation of these residues are essential for both nuclear import and the pre-mRNA splicing process (Cao et al., 1997). Transportin-3 (TNPO3) directly binds to ASF/SF2, facilitating its nuclear import. Phosphorylation of ASF/SF2 is thus required for TNPO3 to execute its function (Lai et al., 2001). In addition, colocalization between TNPO3 and SRSF1 (ASF2) was demonstrated in myoblasts during myogenic differentiation (Costa et al., 2022). It occurred mainly in the early differentiation stages, and it was almost localized in the nucleus of differentiated myotubes in the late stages. RNA- binding protein motif 4 (RBM4), as another TNPO3 cargo, shuttles continuously between the nucleus and the cytoplasm. It plays a hierarchical role in muscle cell differentiation and alternative splicing control (Lin J.C and Tarn, 2012). Both RBM4 and SRSF1 (ASF2) regulate the splicing of muscle-specific transcripts including Myocyte Enhancer Factors 2 C (MEF2C) factor and are involved in the differentiation of muscle cells. Specifically, the kinase downregulation mediated by shRNA *(Short hairpin RNA)* responsible for SRSF1 phosphorylation and activation in murine myoblasts, inhibits MEF2C α2 isoform splicing, which is seen to be involved in differentiation-promoting processes of myoblasts (Zhang et al., 2015).Similarly, transfection of a vector that mediates the RBM4 expression, in the same cell model, leads to a comparable result, which instead increases MEF2C α2 isoform exon. (Lin J. C.and Tarn, 2011).For what concerns its structure, TNPO3 is made up by 20 HEAT (Huntington, Elongation Factor 3, PR65/A, TOR) repeats. It acquires a toroidal shape causing N-terminal and C-terminal domains to face each other. HEAT repeats are a tandemly repeated 37-50 amino acid long modules forming a rod-like helical structure where two alpha helices interface each other by a loop of variable length (Maertens et al., 2014), enabling protein-protein interactions activities.

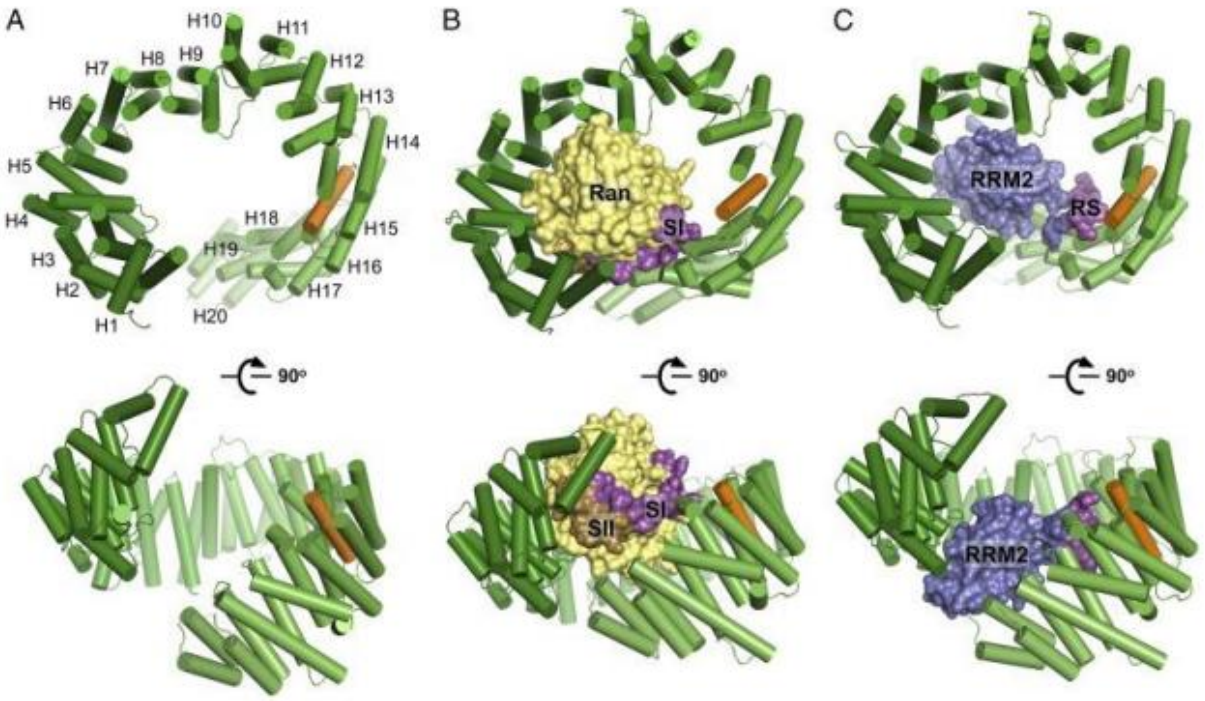

Figure 12. Three-dimensional structure of unbound TNPO3 (A), bound to RanGTP (B) or bound to SRSF1 (C). TNPO3 is represented in green with a display method that highlights HEAT repeats, while TNPO3 cargo proteins are represented through the shell model (Maertens et al. 2014).

Tissue engineering and skeletal muscle tissue engineering

Tissue engineering is a multidisciplinary field that integrates biological sciences and engineering to develop tissues capable of restoring, maintaining, or enhancing tissue function, and in some cases, replacing entire organs (Langer et al., 1993). This approach involves the creation of tissue-like structures through the combination of living cells, biocompatible scaffolds, biochemical signals (e.g., growth factors), and physical stimuli (Berthiaume et al., 2011). The concept of "tissue engineering" emerged in the late 1980s when Dr. Joseph Vacanti and Dr. Robert Langer introduced synthetic, biocompatible, and biodegradable polymers as scaffolds for cell delivery. This represented a shift away from naturally occurring scaffolds, which had unmodifiable physical and chemical properties (Vacanti, 2006). The field revolves around four key components: (I) selection and isolation of appropriate cells, (II) scaffolds made from synthetic or natural biomaterials, (III) signaling molecules that guide cellular activity, and (IV) bioreactors that provide a controlled, biologically active environment for tissue growth (El-Sherbiny & Yacoub, 2013). (Figure 13)

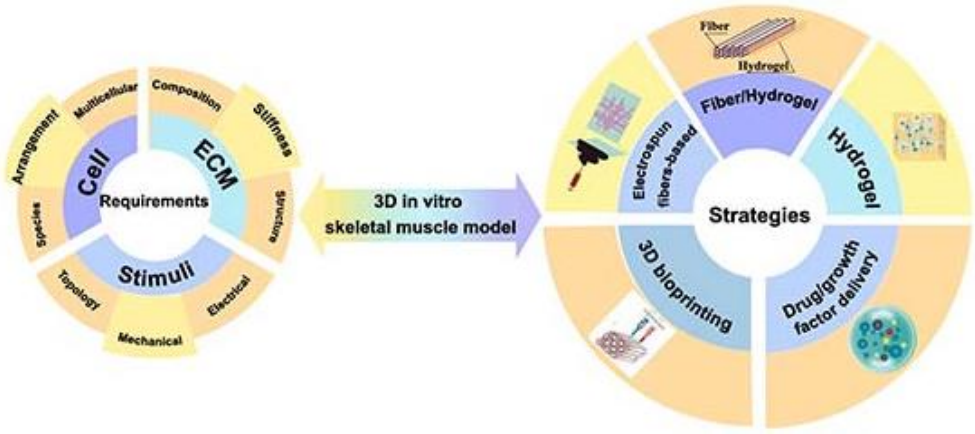

Figure 13. Graphical summary of the tissue engineering skeletal muscle progresses including various bioengineering strategies, such as 3D geometrical confinement, electrospinning, the controlled cell/molecule delivery and porous hydrogels (Zhuang et al., 2020).

The applications of tissue engineering are vast, targeting tissues undergoing damage or degeneration, example are for skin, muscle, liver, and pancreas (Berthiaume et al., 2011). Particularly, skeletal muscle tissue engineering (SMTE) seeks to repair or restore functionality in muscles affected by diseases, trauma, or surgeries. Skeletal muscle injuries, such as volumetric muscle loss (VML), myopathies, significant traumatic injury, and aggressive tumor removal, compromise the muscle's innate regenerative capacity, leading to permanent loss of mass and function (Kwee & Mooney, 2017). Conventional therapies like autologous muscle transplantation and ex vivo muscle cell injections are only partially effective. As a result, SMTE has emerged as a promising method, utilizing tissue engineering's regenerative potential to repair muscle tissue (Kang et al., 2020). SMTE involves the use of myogenic progenitor cells or cells from patients to generate functional skeletal muscle (Ostrovidov et al., 2015). Scaffolds play a critical role in this process by mimicking the extracellular matrix (ECM) and providing structural and mechanical support. Collagen, a major ECM protein, has been widely used in SMTE applications (Beier et al., 2009). In addition to collagen, synthetic and natural materials such as polycaprolactone (PCL), alginate, and fibrin have been employed to improve scaffold performance (Patel et al., 2019). Scaffolds with specific properties, such as stiffness, topography, electrical conductivity, and polymer composition, have been developed to enhance muscle differentiation and functionality. Additionally, co-culturing skeletal muscle cells with endothelial cells to vascularize the muscle, fibroblasts to engineer the myotendinous junction (MTJ), or neural cells to create neuromuscular junctions (NMJs) has allowed for more complex engineered tissues (Ostrovidov et al., 2019). Despite significant progress in SMTE, fully functional *in vitro* skeletal muscle tissue constructs have yet to be developed. One promising avenue to overcome this challenge is 3D bioprinting, which allows for the precise spatial

organization of cells in complex structures that closely resemble native muscle tissue. Electrospinning is another approach used to create microporous, aligned structures with a variety of materials, offering a straightforward method for generating skeletal muscle tissue constructs (Kang et al., 2020). Both 3D bioprinting and electrospinning hold potential for advancing SMTE by facilitating the de novo synthesis of skeletal muscle tissues. The success of skeletal muscle tissue engineering hinges on replicating the structural organization of muscle fibers, which is crucial for contractile properties and efficient force production (Kang et al., 2020). Creating an anisotropic environment in which myoblasts can align, fuse, and undergo myogenesis is essential for engineering functional muscle fibers. Furthermore, using co-cultures with other muscle-resident populations, such as endothelial and neural cells, can further improve the biomimetic tissue outcome by enhancing vascularization and forming neuromuscular junctions (Colapicchioni et al., 2022) (Figure 14-15).

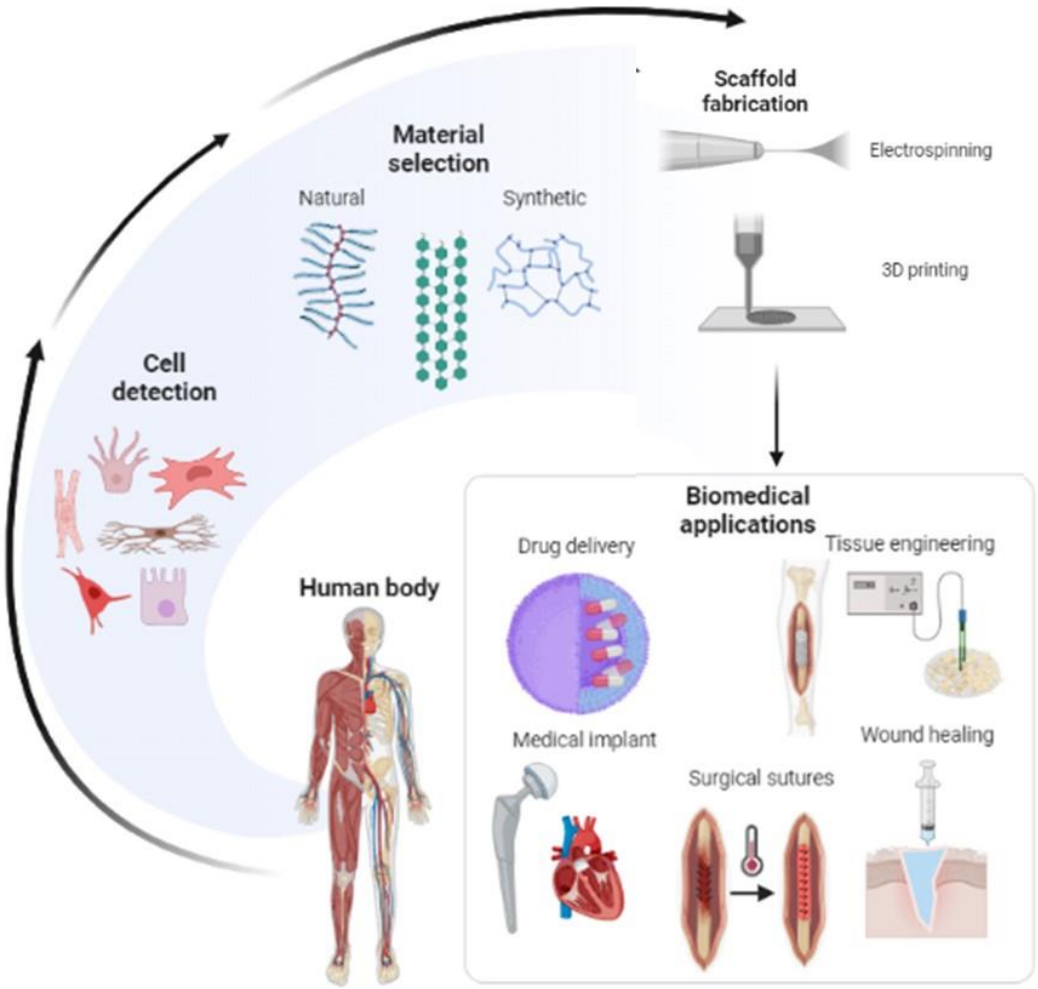

Figure 14. Scheme of various biomedical applications using electrospinning and 3D printing.

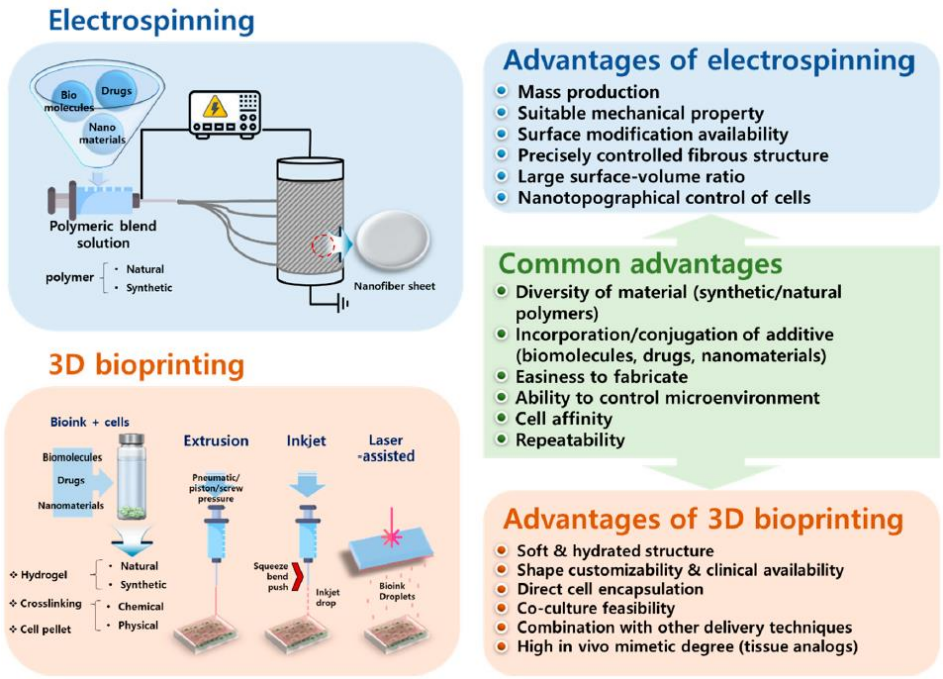

Figure 15. Pros and cons between electrospinning and 3D bioprinting to engineer skeletal muscle tissue constructs (Kang et al., 2020).

Electrospinning

Electrospinning is a simple, adaptable, and controlled technology for the production of micro/nanofibers from polymer solutions or melts using electrostatic forces (Pieri et al., 2020). Electrospinning is the most efficient method for aligning and elongating polymer chains to produce polymeric nanofibers with well-defined structures that can mimic the physical functions of the native ECM, providing numerous attachment points for cell adhesion and growth and thus influencing their morphology and activities (Yang et al., 2022). A typical electrospinning setup includes a syringe with a polymer solution attached to a metallic needle, a syringe pump to control the flow rate, a high voltage power source, and a metallic collector. When a voltage is applied between the syringe and the collector, the solution extruded via the metallic needle transforms into an electrically charged jet that is drawn toward the collector. As the solvent evaporates along the jet's course from the spinneret to the collector, the jet width reduces substantially, resulting in the development of a mat ofthin fibers deposited randomly on the metallic collector (Figure 15A). Numerous factorsaspects, including solution qualities (solvent, concentration, molecular weight, viscosity), process settings (flow rate, voltage, distance between the needle and collector), and ambient conditions (humidity, temperature), can influence the diameter and repeatability of the electrospun fibers and the reproducibility of the process (humidity, temperature) (Pieri et al., 2020).

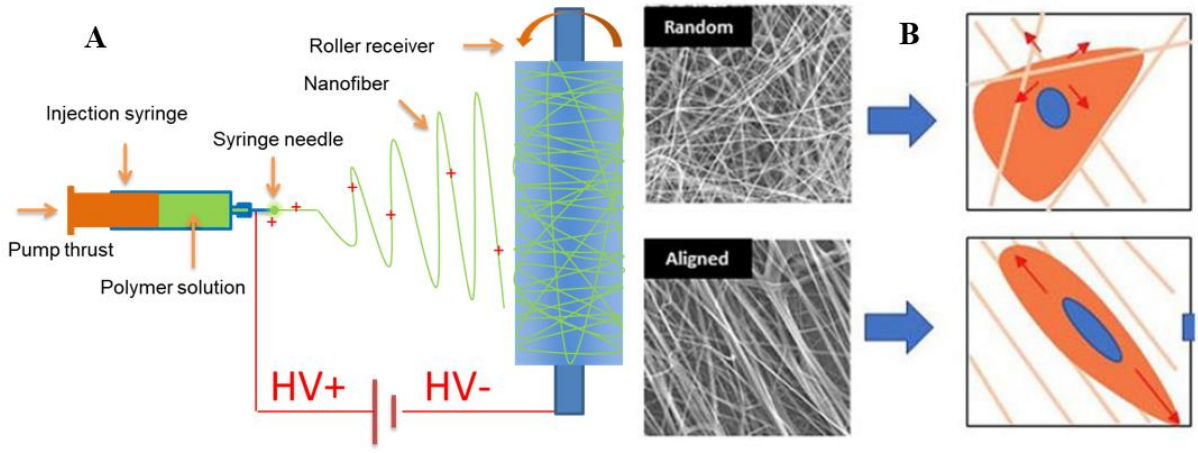

Figure 16. The Electrospinning setupmachine. (B) Schematic image of fibrinogen substrate the deposition of electrospun fibers with different topographies, which direct the cell morphology phenotype (Alarcin et al., 2021)

Because electrospun fibers assemblies the nanoscale qualities of a natural ECM, it became possible to reproduce and rebuild the native tissue conditions. Topographical effects may be used to evaluate the qualities of electrospun nanofibers, such as random and aligned structures (Figure 15B), varied thicknesses, and nanoscale micropores. Many studies have shown that electrospun fibers have a high potential for skeletal muscle regeneration. For example, electrospinning has been utilized to create scaffolds with uniaxially designed structures that lengthen myotubes (Alarcin et al., 2021). An orientated scaffold that acts as a template for alignment might be employed to induce the myoblasts organization since they fuse and differentiate into multinucleated myofibers. The electrospinning technology is appealing for this application because of the degree of control provided by adjusting various parameters (Aviss K, et al., 2010).

3D bioprinting

Three-dimensional (3D) bioprinting is a cutting-edge technology that allows for the fabrication of complex biological constructs with hierarchical structures mimicking native tissues (Murphy & Atala, 2014). This technique involves the layer-by-layer (LbL) deposition of bio-functional materials to create 3D constructs, typically on substrates or tissue culture dishes. The capacity to design and produce structures with pre-defined geometries and specific functionalities holds great potential for applications in tissue engineering and regenerative medicine. A key element in 3D bioprinting is the bioink, which plays a critical role in replicating the extracellular matrix (ECM) to

support essential processes such as cell proliferation, differentiation, and overall functionality. The formulation of bioinks is of paramount importance, as their rheological properties, such as viscosity and gelling time, affect both the resolution and structural integrity of the printed constructs (Gungor-Ozkerim et al., 2018). For example, high viscosity bioinks, although beneficial for printability, may hinder cell migration, differentiation, and matrix remodeling due to their dense polymer networks (Hospodiuk et al., 2016). Typically, bioinks are composed of biomaterial solutions in a hydrogel form, encapsulating the cells required for tissue development. These biomaterials include natural hydrogels such as collagen, alginate, and gelatin, which provide physical support and promote cell functionality. To enhance performance, natural polymers can be chemically modified, for instance, by adding methacryloyl groups to enable photocrosslinking. In contrast, synthetic polymers, such as PEG-based hydrogels, PVA, and PCL, offer high biocompatibility and customizable properties. Combining both natural and synthetic polymers into composite bioinks provides an optimal balance, leveraging the strengths of both to enhance cell support and material customization. (Figure 17).

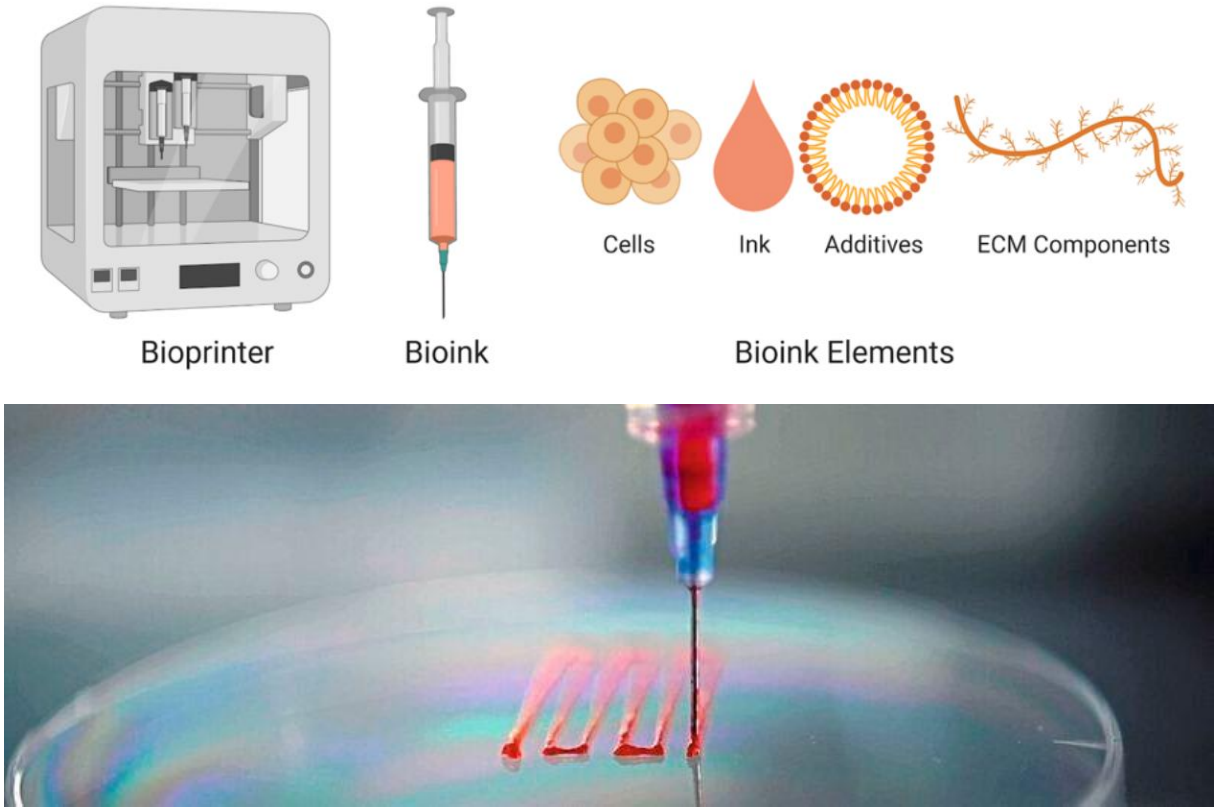

Figure 17. Bioprinting illustrations.

Different bioprinting techniques, such as extrusion-based, inkjet, laser-assisted, and stereolithography, offer various advantages for tissue fabrication (Figure 17). Extrusion-based bioprinting uses mechanical pressure to push bioink through a nozzle, allowing continuous deposition and high cell viability. Inkjet bioprinting deposits bioink in droplets using microvalves and supports various operational mechanisms, including thermal, acoustic, electrostatic, and piezoelectric methods. Laser-assisted bioprinting is known for its precision and achieves high cell viability, though it is more costly. Stereolithography, which uses photosensitive resins for point-by-point 3D construction, is still undergoing optimization. Each bioprinting method contributes to the creation of functional 3D tissue constructs, enhancing *in vivo* mimicry compared to traditional 2D cell culture methods (Kapałczyńska et al., 2018; Gaebel et al., 2011; Guillotin et al., 2010; Beier et al., 2009; Zheng et al., 2021; Mandrycky et al., 2016).

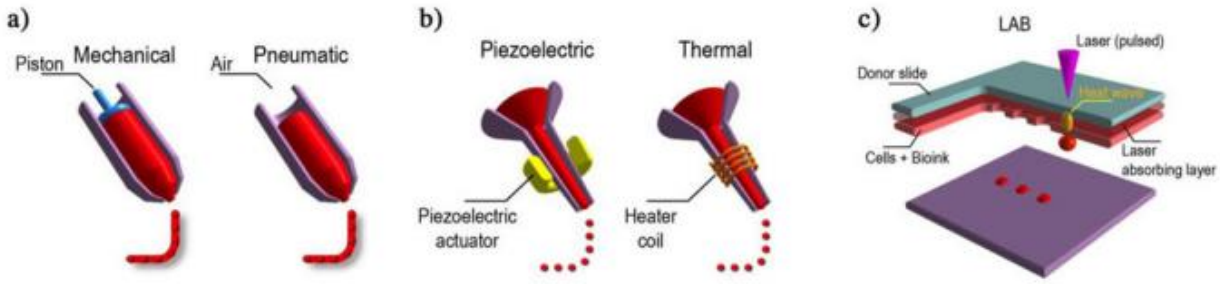

Figure 18. Three major bioprinting strategies are: (A) Micro-extrusion printers that extrude cell-containing biomaterials using pneumatic or mechanical systems. (B) Inkjet bioprinters that employ heating or ultrasonic pressure to create bioink-cell droplets. (C) Laser -assisted bioprinters (LAB) that, heating an absorbing substrate, use laser beams to dispense cell-containing biomaterials (Ostrovidov et al; 2019).

Hydrogel

Hydrogels are three-dimensional networks made up of hydrophilic polymers that are joined together by covalent bonds or by physical intramolecular and intermolecular interactions. They may absorb large volumes of water or biological fluids, up to thousands of percent, and swell quickly without disintegrating. Hydrogels are spongy and stretchy when swelled, imitating biological tissues to a large extent (Figure 18 a-d) (El-Sherbiny and Yacoub, 2013). Hydrogels are classified as natural, synthetic, or semisynthetic (also known as hybrid). Depending on their stability in a physiological environment, hydrogels can be either durable (as are most polyacrylate-based hydrogels) or biodegradable (as are polysaccharide-based hydrogels). Natural hydrogels are often characterized by adhesion sites for cell attachment and strong interactions with cells, whereas synthetically generated hydrogels lack

adhesive sites for cell attachment and have nonspecific interactions with cells. Hybrid hydrogels, which include both biological and synthetic parts, can be proteolytically degradable via their biological domains while yet having precise mechanical characteristics dictated by the synthetic composition (Lev and Seliktar, 2018)

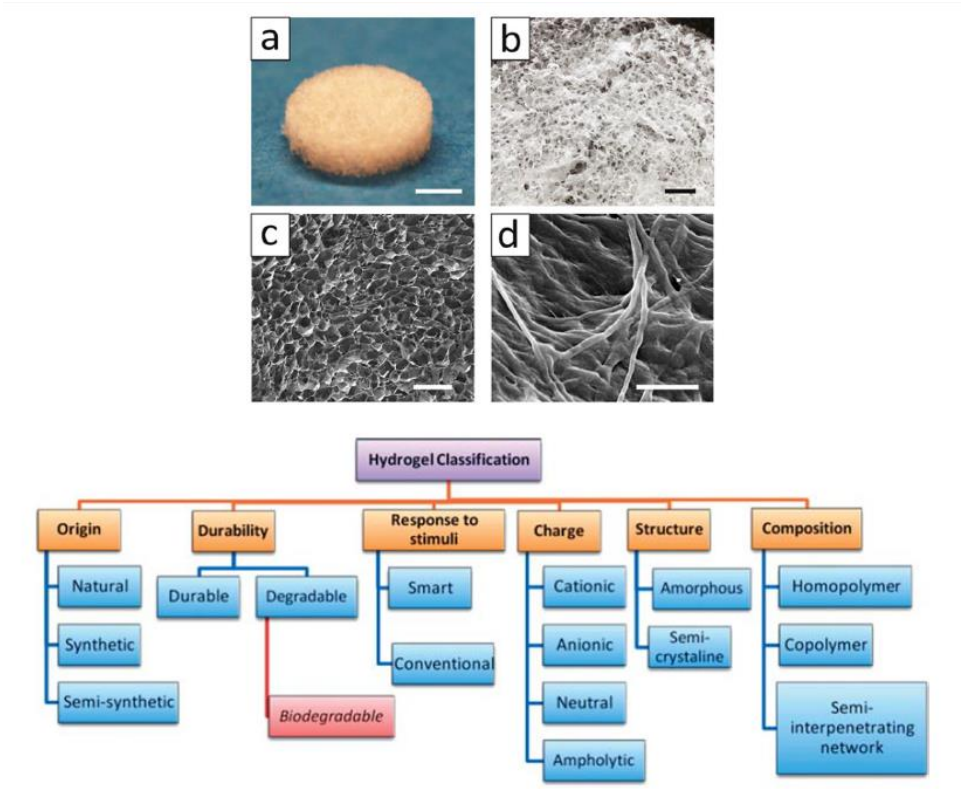

Figure 19. (a, b) Pictures of the collagen scaffold. (c) SEM micrograph showing the fibrous and porous surface of the scaffold, revealing its high porosity. (d) High magnification SEM micrograph showing the minute architecture of the scaffold (Liverani et al., 2019). In the bottom there is a scheme of hydrogel classification (El-Sherbiny and Yacoub, 2013).

The design requirements should also incorporate traditional mechanical and physicochemical metrics (such as biodegradation, porosity, and correct surface chemistry) as well as biological performance measures (such as biocompatibility and cell adhesion).

The main criteria of a scaffold for tissue engineering are (El-Sherbiny and Yacoub, 2013):

- Maintenance of cellular proliferation and optimal cellular dispersion during the scaffold's life span. In many circumstances, this would be till its full decay.
- Hydrogel scaffolds must be extremely porous with an open interconnected structure allowing a large surface area relative to the scaffold’s volume.

- Many other essential factors include pore size, pore volume, pore size distribution, and pore interconnectivity, which promote cell ingrowth, homogenous cell distribution, and matrix neovascularization.
- Both the physicochemical and topographical surface properties of scaffolds are important in determining and influencing cellular adherence and proliferation.

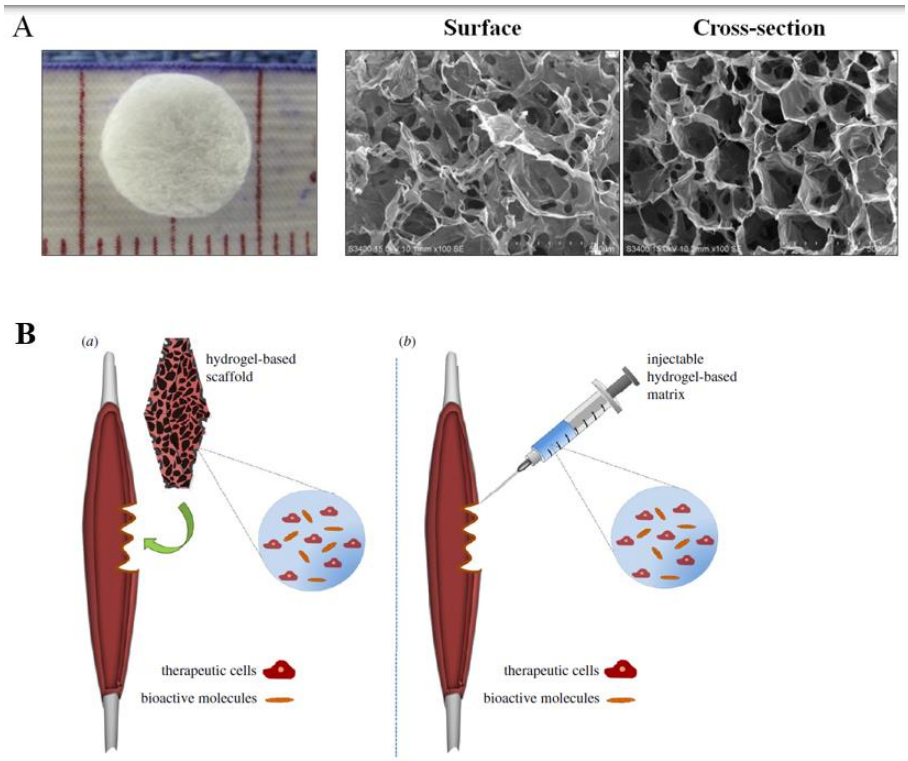

Figure 20. (A) Collagen I hydrogel scaffold. (B) Administration of hydrogel-based delivery systems for therapeutic cells and/or bioactive agents in the treatment of skeletal muscular myopathies .The first strategy involves the implantation of a pre-formed hydrogel-based scaffold. The second strategy, an injectable approach, involves either a liquid precursor of the matrix that is injected and then formed in situ, or pre-formed hydrogel particles designed to pass through the needle (Lev and Seliktar, 2018).

Hydrogels have been used as extracellular matrices, to encapsulate and deliver cells, to act as tissue barriers and bioadhesives, to serve as drug depots, and to deliver bioactive molecules. Thanks to their capacity to adapt their mechanical properties to those of natural tissues, hydrogel-based scaffolds are a particularly significant class of scaffolds. The use of hydrogels for skeletal muscle tissue engineering is emerging as a viable therapeutic option due to their natural ability to encapsulate cells in situ, enhance cell survival, aid integration, and provide protection during implantation (Figure 19 A) (Lev and Seliktar, 2018). The porous microstructure of hydrogel scaffolds facilitates the diffusion of oxygen, nutrients, and growth factors, making them ideal for the development and differentiation

of myogenic cells in mass culture and for myoblast engraftment in skeletal muscle regeneration. Hydrogels in muscle regeneration research can be categorized into two main methods (Figure 19B): the first involves injectable hydrogels that either stimulate endogenous restoration and regeneration or serve as delivery vehicles for therapeutic agents, including cells and bioactive molecules. The second strategy utilizes hydrogels as prefabricated scaffolds to direct *in vitro* muscle tissue synthesis or orchestrate in situ muscle tissue regeneration *in vivo* (Lev and Seliktar, 2018). Current approaches employ type I collagen hydrogel scaffolds to facilitate myoblast engraftment. Collagen, a primary extracellular matrix (ECM) protein, plays a pivotal role in muscle tissue architecture by providing structural integrity and mechanical stability. Type I collagen, the most prevalent form, is extensively utilized to promote myogenic differentiation and tissue repair due to its bioactive properties that support constructive remodeling. Its inherent tensile strength and rigidity enhance muscle function by reinforcing tissue and improving regenerative capacity after injury. Collagen I scaffolds possess bio-inductive and biomechanical properties, making them highly suitable for tissue engineering applications. These scaffolds provide a three-dimensional framework for cell adhesion, migration, and proliferation while actively promoting cellular processes that facilitate tissue remodeling and integration. Myoblasts seeded on collagen scaffolds exhibit improved survival, proliferation, and alignment, which are crucial for functional myotube formation. Additionally, collagen's mechanical resilience allows it to withstand dynamic forces generated by muscle contractions, while its biodegradability ensures gradual degradation and replacement by native tissue over time. Given its biocompatibility and minimal immunogenicity, collagen is widely applied in regenerative medicine, including muscle repair, wound healing, and reconstructive procedures. Collagen-based scaffolds have been shown to enhance muscle regeneration by fostering myoblast alignment and maturation, key factors in restoring functional muscle tissue (Chan et al., 2016). The combination of its bio-inductive potential and mechanical support underscores the critical role of collagen scaffolds in promoting successful myogenic engraftment and tissue regeneration. Hydrogels used in bioink formulation, along with cells, must satisfy specific criteria, including biocompatibility, biodegradability, and appropriate mechanical properties (Tian S. et al., 2023) Among their physicochemical properties, rheological behavior is the most critical factor influencing printability and shape fidelity of the final construct (Schwab A et al., 2002). In extrusion-based bioprinting (EBB), the ideal bioink must adjust its rheological properties as the extrusion process progresses through distinct phases: (i) prior to dispensing, the material should exhibit a gel-like state; (ii) during extrusion, it should demonstrate shear-thinning behavior; and (iii) after deposition, it must retain its elastic shape and structural integrity. Evaluating the viscoelastic properties of hydrogels is thus the primary step in bioink development, alongside assessing cell viability and proliferation post-

bioprinting. The most commonly used biomaterials in bioprinting include natural polymers like alginate, gelatin, collagen, hyaluronic acid, chitosan, and decellularized extracellular matrix (d-ECM), as well as synthetic polymers such as poly(ethylene glycol) (PEG), Pluronic, and polyvinyl alcohol (PVA) (Rezvani G. E. et al., 2021). Among these, collagen is of particular interest due to its abundance in the human body, high biocompatibility, and low immunogenicity, facilitating its success in biomedical applications (Sorushanova A. et al., 2019). Collagen, the major insoluble fibrous protein in the extracellular matrix (ECM) and connective tissue, is categorized into 29 different types based on properties, functionality, and distribution in native tissues (Lee J M. et al., 2021, O'Connell C D. et al., 2018). It consists of repetitive amino acid sequences that self-assemble into fibrils under physiological conditions (neutral pH and 37°C). While collagen supports cell adhesion and proliferation, its use in 3D bioprinting poses challenges due to low mechanical strength, limited mass transport, and short-term structural stability. To address these issues, fibrillar collagen has been introduced for 3D printing, replacing soluble collagen forms; however, fibrillar collagens could only be uniformly resuspended and printed in weakly acidic solutions, which are unsuitable for maintaining cell viability. A novel bioink composed of fibrillar type I collagen derived from equine tendon has been developed through a proprietary process, resolving the limitations of traditional collagen-based bioinks and enabling the creation of durable 3D structures in physiological conditions with customizable mechanical properties.

1. Applications of Electrospinning in Skeletal Muscle Tissue Engineering

1.1 Electrospun Poly(L-lactide-co-ε-caprolactone) Scaffolds for Enhanced C2C12 Myoblast Bioactivity and Their Role in Promoting Cell Commitment for Skeletal Muscle Regeneration Applications

1.2. Controlled *in vitro* electrostimulation assays of a myoblast cell line cultured on ion-permeable electrospun poly(L-lactide-co-ε-caprolactone) scaffolds.

1.1 Electrospun Poly(L-lactide-co-ε-caprolactone) Scaffolds for Enhanced C2C12 Myoblast Bioactivity and Their Role in Promoting Cell Commitment for Skeletal Muscle Regeneration Applications

Introduction

Frequent causes of skeletal muscle (SKM) loss include injuries, surgery, aging, metabolic diseases, and inherited genetic disorders. While satellite cells (SCs), located between the basal lamina and sarcolemma of mature myofibers (Mauro A. 1961), can partially restore SKM wasting, their self-regenerative potential diminishes with age and disease (Corbu A. et al., 2010). Consequently, due to limited regenerative capacity, surgical interventions, and few therapeutic options, SKM loss is often considered largely irreversible (Liu J et al.,2018, Bloise N. et al., 2018). New strategies are required to address the limitations of conventional therapies for muscle regeneration (Biressi S. et al., Judson R.N. et al., 2020, Scharner J. 2011). Efforts have been made to engineer SKM tissue *in vitro* using synthetic polymeric biomaterials. *In vitro* models are valuable tools in medicine and biology for studying cells and tissues and conducting functional tests. Although tissue culture plastics (TCPs) are commonly used for 2D cell culture, their stiffness and two-dimensional structure are unsuitable for advanced studies. Extensive research aims to create functional 3D supports, or scaffolds, that more accurately represent the tissue microenvironment and can be adjusted according to experimental needs (Harrison R.G. 1959, Aggarwl B.B. et al., 2009). Scaffolds, combined with regulatory signals, offer a biomimetic extracellular matrix (ECM) for cell growth and proliferation, making them crucial in tissue engineering (TE) (Chan B.P et al., 2008, Evans D.J.R. et al., 1999, Gualandi C., et al., 2012). The electrospinning (ESP) technique has been employed to fabricate electrospun scaffolds for various TE strategies (Pham Q.P. et al., 2006). Synthetic aliphatic polyesters, known for their mechanical properties, commercial availability, and FDA approval, have been successfully electrospun (Mukherjee S. et al., 2011). ESP allows for the creation of fibers with controlled dimensions and orientation, providing an anisotropic structural organization for SKM tissue (Mertens J.P. 2014, Turner N.J. et al., 2011). SKM development begins with myoblasts derived from myogenic precursors and culminates in the formation of multinucleated myotubes through myocyte fusion, ultimately resulting in mature muscle fibers with parallel myofibrils (Chal J., 2017) and aligned sarcomeres (Sanes J.R. 2003). Electrospun scaffolds can guide myofibril alignment and support SKM tissue formation, a feature not achievable with traditional TCPs (Yang D. et al., 2022). Numerous studies have evaluated the advantages and limitations of different electrospun scaffolds for SKM tissue fabrication (Colapicchioni V. et al., 2022). For instance, Choi et al. 2008 demonstrated that an electrospun aligned poly(3-caprolactone) (PCL)/collagen nanofiber

scaffold facilitated myoblast alignment, while an elastic substrate was needed for myotube differentiation. Krishna H Patel (2019) emphasized the need for micropatterned scaffolds that guide cell organization and stimulate proliferation, using a blend of PCL and decellularized ECM. L. Wang et al. (2015) highlighted the benefits of integrating electrospun scaffolds with additional biomaterials; an aligned nanofiber scaffold combined with hydrogels produced parallel and elongated myotubes. Since cells in their native environment are surrounded by various structures, it is expected that cell attachment, proliferation, and differentiation could be influenced by external micropatterned materials (Li H. et al., 2011). However, external stimuli must be consistent to impact cells, necessitating that scaffolds maintain mechanical integrity. The copolymerization of lactide (LA) with the flexible caprolactone (CL) unit effectively controls the mechanical properties and degradation rate of the materials (Qian H., et al., 2000, Penning J et al., 1993), expanding the range of biomedical applications and making them suitable for providing steady stimuli *in vitro* or *in vivo* (Jeong S.I. et al., 2004). In this study, we designed an electrospun scaffold made of poly(L-lactide-co-ε-caprolactone) (PLCL), coated with type I collagen, to recreate a favorable environment for cells. By recognizing collagen as a key ECM component of SKM, cells can adhere to the substrate (Wu T. et al., 2017). The scaffold features controlled microarchitecture to promote cell growth, suitable physicochemical properties for cell interactions, appropriate mechanical properties to support cell functionality, and a customized morphology that mimics the native environment. This setup enabled us to further investigate the phenotypic profile of myoblasts throughout SKM tissue formation. Following the suggestions of E. Martinez (2009) and Huaqiong Li (2000), we explored how the micro- and nanostructure of the scaffold influences cell deformation and nuclear changes, as the nucleus is connected to the cytoskeleton by intermediate filaments. We analyzed the effects of the polymer-based scaffold on differentiation at various stages of myogenesis, using precise quantitative analysis of differentiation-specific markers. This included examining myogenic regulatory factors (MRFs), which directly control the myogenic process and interact with myocyte-specific enhancer factors (MEFs) that regulate myoblast commitment (Naidu P.S. et al., 1995, Asfour H.A. et al., 2018). Additionally, we studied myoblast morphology during myogenic commitment using confocal and electron microscopy to determine how the scaffold shapes SKM myogenesis and tissue growth, revealing the link between cell fate and material cues. These findings offer crucial insights into SKM development, essential for understanding physiological tissue formation and identifying deviations indicative of dysfunctional or pathological SKM.

Materials and Methods

Electrospun nanofibrous scaffold

Poly(L-lactide-co-ε-caprolactone) (PLCL) copolymers with varying compositions were obtained from Corbion (Amsterdam, The Netherlands). Specifically, PLCL 70/30 (LA/CL molar ratio) (PURASORB® PLC 7015, inherent viscosity midpoint 1.5 dL/g), PLCL 85/15 (PURASORB® PLC 8516, inherent viscosity midpoint 1.6 dL/g), and PLCL 95/5 (PURASORB® PLC 9517, inherent viscosity midpoint 1.7 dL/g) were utilized. Dichloromethane (DCM) and dimethylformamide (DMF) were purchased from Sigma-Aldrich and used as received, without further purification. Type I collagen solution (0.25% in acetic acid) derived from calf skin was also sourced from Sigma-Aldrich (St. Louis, MO, USA).

PLCL Scaffold Fabrication

The custom-made electrospinning setup included a high-voltage power supply (Spellman SL 50 P 10/CE/230), a syringe pump (KD Scientific 200 series), and a glass syringe containing the polymer solution attached to a stainless steel blunt-tip needle. A rotating metallic drum collector (120 mm length, 50 mm diameter) was employed to fabricate electrospun scaffolds consisting of uniaxially aligned nanofibers. The electrospinning process was conducted at room temperature (RT) with 50% relative humidity. Polymer solutions were prepared by dissolving each of the three PLCL samples in a DCM:DMF solvent mixture (65:35 v/v) at a 20% w/v polymer concentration. The solution was dispensed at a flow rate of 1.2 mL/h, with a 20 cm gap between the needle and collector, and a 20 kV applied voltage. To produce aligned nanofibers, the collector rotated at a linear speed of 15.7 m/s, while random fibers were obtained with a rotation speed of 6000 rpm. After 90 minutes, electrospun mats measuring 30–40 μm thick and 15 × 8 cm in size were produced.

PLCL Scaffold Characterization

Scanning electron microscopy (SEM) analysis was conducted using a Phenom Pro-X SEM (Thermo Fisher Scientific Inc., Waltham, MA, USA) at an accelerating voltage of 10 kV on samples sputtered with a thin layer of gold. Nanofiber diameter distribution was evaluated from SEM images using Fiji, an open-source software based on ImageJ2. The results are expressed as mean diameter ± standard deviation (SD). Fiber orientation in the aligned nanofiber mats was quantified using the Directionality plugin in Fiji, based on the local gradient orientation method, following a previously validated procedure. Thermal properties were assessed with a differential scanning

calorimeter (DSC Q100; TA Instruments, New Castle, DE, USA). Approximately 5 mg of sample was placed in Tzero aluminum pans and subjected to heating at a rate of 20 °C/min, from −80 °C to 200 °C, followed by quenching to −80 °C and reheating to 200 °C under a nitrogen atmosphere. Mechanical properties were evaluated using an Instron 4465 tensile testing machine on rectangular strips (5 mm wide, 20 mm gauge length) cut from the electrospun mats, with the fiber orientation aligned with the gauge length. The crosshead speed was 10 mm/min, corresponding to a strain rate of 50%/min. Results are presented as average values ± SD and are displayed in stress–strain curves.

C2C12 culture on PLCL

Prior to cell seeding, all scaffolds were cut into suitably sized pieces and assembled with CellCrown™ support (Scaffdex, Tampere, Finland), then sterilized using ethanol following a previously described protocol (Alessandri M. et al., 2021).

PLCL Functionalization

A Type I collagen solution derived from calf skin was diluted 10-fold with distilled water to achieve a final working concentration of 0.01%. This solution was used to coat sterilized scaffolds by applying it overnight at 4 °C. After coating, the solution was removed, and the scaffolds were rinsed with PBS prior to cell seeding. Fourier transform infrared spectroscopy (FT-IR) was performed on both uncoated and coated scaffolds using a Spectrum Two instrument equipped with an ATR accessory (Perkin-Elmer, diamond crystal, Milan, Italy). Spectra were collected between 400 cm−1 and 4000 cm−1, with a resolution of 4 cm−1, accumulating 16 scans, and a step size of 1 cm−1. The water contact angle (WCA) was measured using the sessile drop method with a 10-second analysis time in air, utilizing a KSV CAM101 instrument (KSV Instruments Ltd., Helsinki, Finland) on both uncoated and coated scaffolds. Ten measurements were taken for each sample.

Cell Culture

C2C12 murine myoblasts (ATCC Cat# CRL-1772, RRID:CVCL 0188) were plated into a complete growth medium composed of Dulbecco's modified Eagle high-glucose medium (DMEM) with 10% fetal bovine serum (FBS) (Biowest, Nuaille, France), L-glutamine (Euroclone, Milan, Italy) and 1% penicillin/streptomycin at 37 °C and 5% CO_2. At 80% confluence, C2C12 were induced to differentiate, replacing complete growth medium with a differentiation medium made of DMEM with 1% horse serum (HS) (Sigma-Aldrich, St. Louis, MO, USA). Myogenic differentiation was

investigated as follows: T0, proliferating undifferentiated myoblast used as control; T1, early stage after 24 h of differentiation; T3–T5, intermediate stage after 3–5 days of differentiation; T7–T10, late stage. C2C12 were cultured with the same cell-seeding density (15×10^3 cells/cm^2) under two conditions: standard TCP as a control and a non-woven PLCL scaffold.

C2C12 Viability Assay

C2C12 cells were seeded on both tissue culture plastic (TCP) and PLCL scaffolds, and cell viability and proliferation were evaluated using the CellTiter 96® AQueous One Solution Cell Proliferation Assay (Promega, Madison, WI, USA), following the manufacturer's protocol. Absorbance was measured at 490 nm using a Spark Tecan microplate reader. Assessments were conducted at four time points (days 1, 2, 5, and 7), with each test performed in triplicate.

C2C12 Morphological Study

The morphological evolution of myogenesis in cells cultured on PLCL scaffolds was examined using scanning electron microscopy (SEM) at 2, 6, and 24 hours of culture. Cell-laden PLCL scaffolds were fixed in 2.5% glutaraldehyde (TAAB Laboratories) in 0.1 M sodium cacodylate buffer (Electron Microscopy Sciences) at pH 7.2 for 3 hours at 4 °C. Following fixation, the samples were washed twice in 0.15 M sodium cacodylate buffer at room temperature (RT) and then further fixed in 1% osmium tetroxide (OsO4) in 0.1 M cacodylate buffer for 30 minutes at 4 °C. The samples were then washed once in 0.1 M cacodylate buffer for 10 minutes at RT, dehydrated through ascending ethanol solutions (70%, 95%, and 100%), and subsequently treated with a 1:1 solution of 100% ethanol and hexamethyldisilazide for 1 hour at RT, followed by overnight incubation in hexamethyldisilazide at RT. The processed cell-seeded PLCL scaffolds were then prepared for SEM analysis according to the Scaffold Characterization Methods.

Quantitative Reverse Transcription Polymerase Chain Reaction (RT-qPCR)

RNA was extracted from C2C12 cells cultured on TCP and PLCL scaffolds at time points T0, T1, T5, and T7 using TRIZOL® reagent (Thermo Fisher Scientific, Waltham, MA, USA), following the protocol described in (Costa R. et al., 2020). One microgram of RNA from each sample was reverse-transcribed, and quantitative real-time PCR (qPCR) was conducted using MaximaTM

SYBR Green qPCR Master Mix 2X (Thermo Fisher Scientific) on an IQ5 Thermal Cycler RT-PCR detection system (Bio-Rad, Hercules, CA, USA). The qPCR analysis was performed in triplicate, with the cycle threshold (CT) values normalized to glyceraldehyde 3-phosphate dehydrogenase (GAPDH). The primers used for qPCR are listed in Table 1.

Table 1. Forward (Fw) and reverse (Rev) primers for real-time qPCR analysis.

Gene (GenBank Accession Number) (Mus Musculus)	**Primers**
Myf5 Myogenic Factor 5 (NM_008656.5)	Fw: 5'-AGGTGGAGAACTATTACAGC Rev: 5'-TGATACATCAGGACAGTAGATG
Myog Myogenin (NM_031189.2)	Fw: 5'-AGTACATTGAGCGCCTAC Rev: 5'-CAAATGATCTCCTGGGTTG
Des Desmin (NM_010043.2)	Fw: 5'-ACACCTAAAGGATGAGATGG Rev: 5'-GAGAAGGTCTGGATAGGAAG
Murf-1(TRIM63) Muscle-specific RING finger protein 1 (NM_001039048.2)	Fw: 5'-GACTTAGAACACATAGCAGAG Rev: 5'-CTCTTCTGTAAACTCCTCCTC
Myf6 Myogenic Factor 6 (NM_001003982.1)	Fw: 5'-ATAGAGAAGGAGCCGTGTTGG Rev: 5'-TTCTCTGAGATCTGGCTGGGA
Mef2c isoforma α1 Myocyte Enhancer Factor 2 C (NM_001170537.1)	Fw: 5'-CTCAGACATTGTGGAGACATT Rev: 5'-TCAGGGCTGTGACCTACTG
Mef2c isoforma α2 Myocyte Enhancer Factor 2 C	Fw: 5'-CTCAGACATTGTGGAGGCAT Rev: 5'-TTCTTCAGTGCGTGGGGT

(NM_001347568.1)	
GAPDH Glyceraldehyde-3-Phosphate Dehydrogenase (NM_001256799.2)	Fw: 5’-CTCTGATTTGGTCGTATTGG Rev: 5’-GTAAACCATGTAGTTGAGGTC

Western Blotting

C2C12 cells cultured on TCP and PLCL scaffolds were lysed with RIPA buffer at T0, and at subsequent time points T1 through T10, as described by Costa et al. [35]. The lysates were collected and stored at −80 °C. Protein concentrations were quantified using a Lowry assay kit. Proteins were separated using Invitrogen NuPage mini gels (Thermo Fisher Scientific, Waltham, MA, USA), transferred to a nitrocellulose membrane, and blocked with 5% skimmed milk in TBS-Tween (0.1% Tween) for 1 hour at room temperature (RT). The membranes were incubated overnight at 4 °C with the primary antibody against skeletal muscle myosin (F59) (dilution 1:200; Santa Cruz Biotechnology, Dallas, TX, USA), followed by a 1-hour incubation at RT with a peroxidase-conjugated secondary antibody. After washing, the membranes were exposed to ECL Western blotting substrates (1:1) for 1 minute, and chemiluminescent signals were detected using Clarity Western ECL Substrate (Bio-Rad, Hercules, CA, USA). The relative intensity of protein expression was analyzed using ImageJ2 and normalized to actin.

Immunostaining

For immunofluorescence (IF) analysis, cell-laden PLCL scaffolds were fixed in 4% paraformaldehyde (PFA) for 20 minutes and subsequently washed three times with PBS. The scaffolds were then incubated overnight at 4 °C with a primary antibody against skeletal muscle myosin (F59) (dilution 1:200; Santa Cruz Biotechnology, Dallas, TX, USA). After washing, the samples were incubated with a secondary antibody (Goat Anti-Mouse IgG (H+L), DyLight 488; dilution 1:1000; Thermo Fisher Scientific, Waltham, MA, USA) for 1 hour at 37 °C. Nuclei were counterstained with Hoechst (Sigma-Aldrich, St. Louis, MO, USA). The slides were mounted with an aqueous medium. Confocal imaging was performed using a Nikon A1 confocal laser scanning microscope with a 40×, 1.4 NA objective, and 405 and 488 nm laser lines. Z-stacks were acquired with an optical resolution of 210 nm/pixel, stored at 12-bit with 4096 gray levels, a pinhole diameter set to 1 Airy unit, and a z-step size of 500 nm. Acquisition parameters, including laser power, amplifier gain, and offset levels, were fixed. Image analysis was conducted using NIS-Elements software (Nikon, RRID:SCR_014329) and ImageJ2.

Quantification and Statistical Analysis

Cell counts were assessed for normality using the Shapiro–Wilk test. Data are presented as mean ± standard deviation (SD). To compare two groups, unpaired two-tailed t-tests were employed. For comparisons involving three or more groups, one-way ANOVAs were conducted using GraphPad Prism. Statistical significance was determined with a threshold p-value of < 0.05.

Results

Design and Evaluation of Poly(L-lactide-co-ε-caprolactone) Nanofibrous Scaffolds

Polymeric scaffolds were obtained by electrospinning PLCL copolymers with various compositions (70/30, 85/15, and 95/05 LA/CL) into nanofibrous porous meshes. The solutions and electrospinning parameters for each polymer were optimized to produce bead-free fibers. Initially, mats of randomly oriented fibers were collected on a drum rotating at low speed (see Material and Methods). SEM images in Figure 1A show uniform, bead-free fibers for all copolymer compositions. Fiber diameter distribution analysis revealed an average diameter of approximately 0.7 ± 0.2 μm for all samples (data not shown). The impact of copolymer composition on the thermal and mechanical properties of PLCL samples was assessed through calorimetric and tensile tests. Figure 1B displays the first DSC heating scans of the as-spun PLCL mats. The copolymers exhibited glass transitions (Tg) at 22 °C, 42 °C, and 57 °C for PLCL 70/30, PLCL 85/15, and PLCL 95/05, respectively, with cold crystallization exothermic peaks followed by endothermic melting peaks of equal magnitude for all samples. This indicates that melting after cold crystallization pertains only to the PLCL crystal phase formed during the heating scan, confirming that the electrospinning process produced entirely amorphous PLCL mats, similar to results for poly(L-lactic acid) (Biresso S. et al., 2020). As anticipated, Tg values, as well as the melting temperature I and melting enthalpy (ΔHm) of the crystal phase formed during cold crystallization, decreased with increasing CL content in the copolymer. Stress–strain measurements of the PLCL scaffolds (Figure 1C) showed that increasing the CL co-unit content from 5 mol% to 15 mol% led to a slight reduction in the elastic modulus from 89 Mpa to 73 Mpa, while further increasing CL content to 30 mol% resulted in a drop to 14.5 Mpa. Notably, among the samples studied, PLCL 70/30 most closely approximates the mechanical behavior of SKM tissue (Young's modulus of relaxed muscle fibers is 61 ± 5 kPa (Marthur A.B et al., 2001)) (Figure 1D). The variations in elastic modulus can be attributed to the solid-state properties of the copolymers [14]. PLCL 95/05 and PLCL 85/15,

with Tg values above room temperature (57 °C and 42 °C, respectively), behave as glassy materials under mechanical testing conditions, exhibiting similar elastic moduli. In contrast, PLCL 70/30 has a Tg lower than the other two copolymers (22 °C), which accounts for its rubber-like behavior and reduced stiffness. Therefore, PLCL 70/30 was selected for scaffold fabrication for SKM applications due to its favorable mechanical properties. PLCL 70/30 scaffolds with aligned fibers were produced using a high-speed rotating drum (see Section 2) to replicate the fibrous morphology of SKM. SEM analysis revealed regular, bead-free fibers, and analysis using Fiji's Directionality plugin showed that the fibers were well-aligned with the rotation direction of the collector (Figure 1E, left image). Approximately 68% of the nanofibers were aligned within 0–18° of the rotation direction, while only 2.6% were aligned within 72–90°. Before biological testing, the scaffolds were sterilized with ethanol, treated at 37 °C in buffer solution for 24 h (Figure 1E, middle image) to check for dimensional and morphological stability during cell culture tests, and coated with type I collagen (Figure 1E, right image). SEM confirmed that neither thermal treatment nor collagen coating altered the fiber morphology. Figure 1F shows the results for uncoated and collagen-coated PLCL, with characteristic bands of PLCL and collagen functional groups identifiable. The absorption bands at 1750 cm−1 and 1730 cm−1 correspond to C-O in PLCL, while bands at 1650 cm−1 (amide I), 1560 cm−1 (amide II), and 3300 cm−1 (-OH) are attributed to collagen. WCA analysis (Figure 1G) confirmed collagen presence, with PLCL, a hydrophobic material, showing a WCA value of 98.72 ± SD 3.1 (Figure 1G top image), compared to a significantly lower value of 37.9 ± SD 3.5 for the collagen-coated electrospun mat (Figure 1G bottom image), indicating increased hydrophilicity.

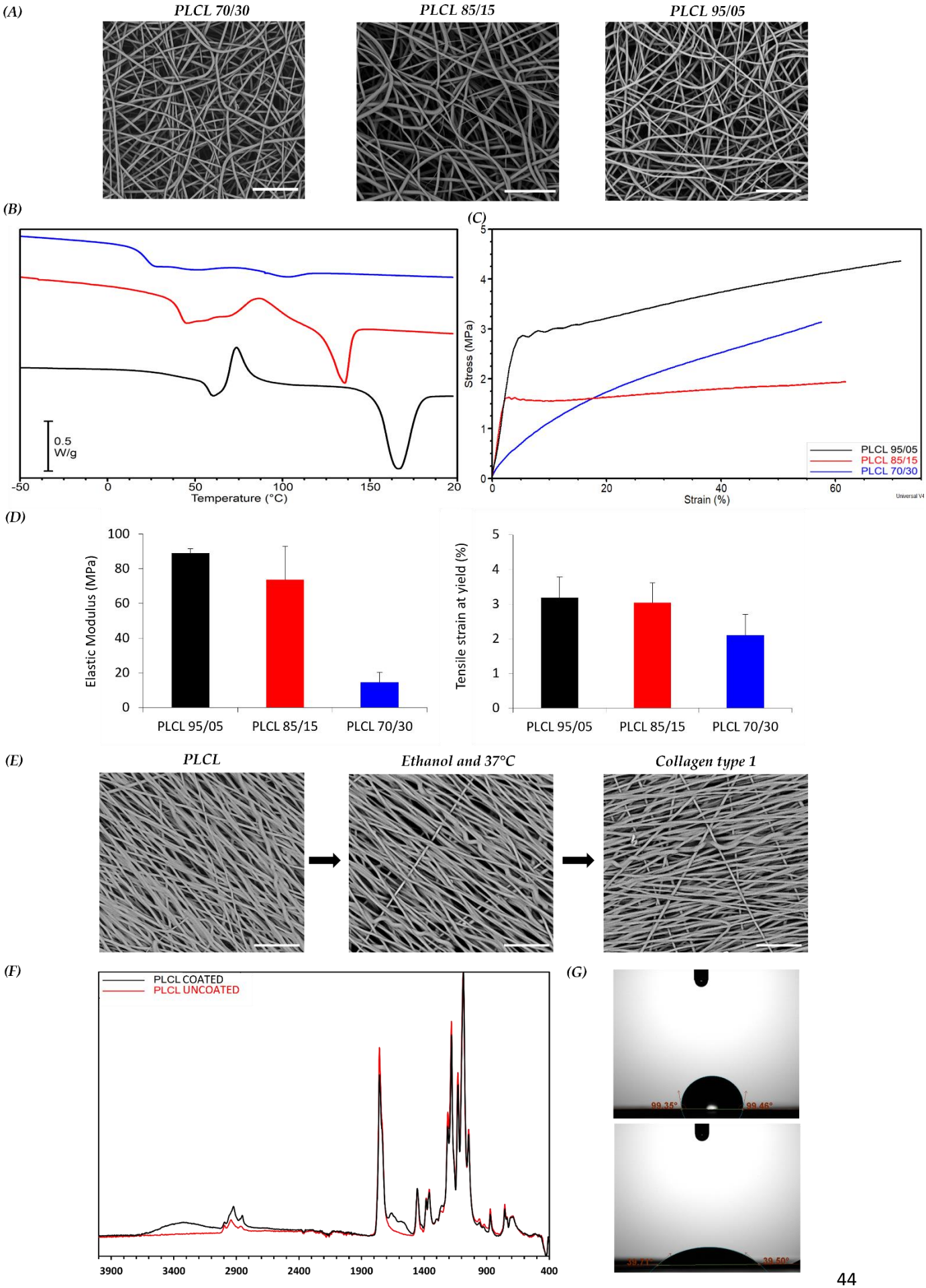
(A)
PLCL 70/30
PLCL 85/15
PLCL 95/05
(B)
0.5
W/g
-50
0
50
100
150
20
Temperature (°C)
(C)
Stress (MPa)
Strain (%)
PLCL 95/05
PLCL 85/15
PLCL 70/30
(D)
Elastic Modulus (MPa)
PLCL 95/05
PLCL 85/15
PLCL 70/30
Tensile strain at yield (%)
PLCL 95/05
PLCL 85/15
PLCL 70/30
(E)
PLCL
Ethanol and 37°C
Collagen type 1
(F)
PLCL COATED
PLCL UNCOATED
3900
3400
2900
2400
1900
1400
900
400
(G)
99.35°
99.46°

Figure 1. Scaffold characterization. (**A**) SEM images of PLCL scaffolds with compositions 70/30 (blue), 85/15 (red), and 95/05 (black). (**B**) DSC heating curves showing the glass transition temperature (Tg) of the scaffolds. (**C**) Representative stress-strain curves for different scaffolds. (**D**) Measurements of Young's modulus and yielding points for the scaffolds. I SEM images of PLCL 70/30 scaffold following ethanol sterilization, 37 °C treatment, and type I collagen coating. (**F**) ATR-IR spectra comparing coated and uncoated PLCL mats. (**G**) Water contact angle (WCA) measurements for uncoated (top) and coated (bottom) PLCL mats. Scale bars: 20 µm.

Assessment of Cytocompatibility and Cell Morphology on scaffold

To assess the cytocompatibility of the PLCL 70/30 scaffold, a cell viability test was conducted. C2C12 murine myoblasts were seeded onto the collagen-coated PLCL scaffold and fixed in a cell-crown insert (Figure 2A). Cell vitality and proliferation were evaluated at days 1, 5, and 7 and compared with control samples. The results indicated that cell viability remained unaffected by the PLCL scaffold throughout the culture period. However, a slight, though not statistically significant, decrease in C2C12 proliferation was observed after 7 days, with reduced cell growth on the PLCL scaffold compared to the control. To further investigate, we analyzed cell morphology (Figure 2B). SEM imaging revealed that C2C12 cells displayed distinct phases of attachment, elongation, and proliferation on the PLCL scaffold. Within 2 hours, C2C12 cells with a round morphology began adhering to the scaffold. By 6 hours, the cells had fully adhered and elongated in alignment with the nanofiber orientation. After 24 hours, a layer of C2C12 cells covered the nanofibrous surface (Figure 2C). These findings are consistent with previous research (Choi J.S. et al., 2008, Narayanan et al., 2020), demonstrating that aligned fibers support cell attachment and growth. Overall, the cell viability, proliferation, and morphological analyses confirm the biocompatibility of the PLCL scaffold and highlight the significance of unidirectional fiber alignment in C2C12 cell morphogenesis.

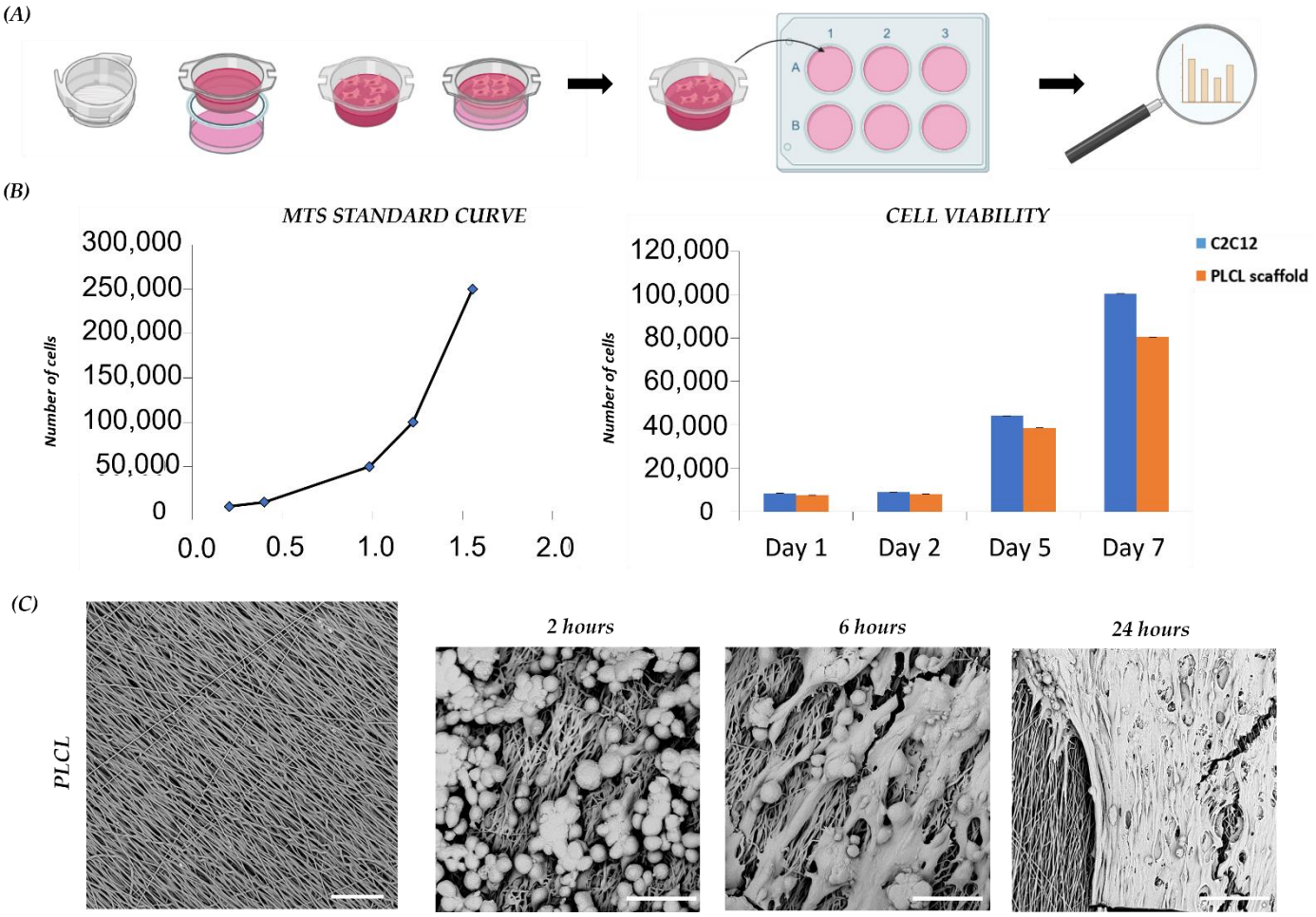

Figure 2. C2C12 proliferation and morphology on scaffolds: (A) Schematic representation of PLCL scaffold preparation for C2C12 cell culture. (B) Cell viability and proliferation of C2C12 on scaffolds and controls, measured on days 1, 2, 5, and 7. (C) Representative SEM images showing C2C12 morphology on PLCL scaffolds before and after cell seeding, at 2, 6, and 24 hours. Scale bars: 25 µm.

Impact of PLCL Scaffold on Myogenic Regulatory Factor Expression and Myoblast Differentiation

To evaluate the influence of the nanostructured PLCL scaffold on myoblast lineage, we examined the expression of myogenic regulatory factors (MRFs) involved in myoblast fusion and myotube formation. We assessed MRF transcript levels during both undifferentiated and differentiated phases of C2C12 cells on the PLCL scaffold and compared them with controls. Pax7, a critical regulator of embryonic skeletal myogenesis, showed downregulation in C2C12 cells on both the PLCL scaffold and control throughout the differentiation period (T1–T7). Notably, increased Pax7 expression was observed on day 7 on the PLCL scaffold, attributed to the residual presence of undifferentiated cells ($p < 0.05$) (Figure 3A). Myf5, which is active during the activation, proliferation, and early differentiation stages of myogenesis, was expressed at higher levels on the

PLCL scaffold compared to the control from T1 (~2–2.5-fold increase) ($p < 0.05$), indicating that the scaffold enhanced cell activation and differentiation (Figure 3A). MyoD levels remained constant over time under both conditions (Figure 3A). Myf5 and MyoD together activate myogenin (MyoG), which is crucial for muscle differentiation and cell cycle arrest. A significantly higher level of MyoG was detected in cells on the PLCL scaffold, with a nearly threefold increase at T1 and a fivefold increase at T7 compared to controls, indicating accelerated differentiation ($p < 0.05$) (Figure 3B). Early Myf6 expression was higher in the control relative to the PLCL scaffold at T1, but late Myf6 expression at T3 was significantly greater on the PLCL scaffold, reflecting anticipated differentiation ($p < 0.05$). Additionally, early differentiation was further evidenced by significantly higher levels of muscle ring-finger protein (MURF-1) on the PLCL scaffold compared to the control, with MURF-1 serving as an autophagic marker associated with late-stage myogenesis and cell death ($p < 0.05$) (Figure 3B). Desmin, a structural gene and early muscle-specific protein, showed relatively stable expression levels over time under both conditions, with a moderate induction in controls upon stimulation ($p < 0.05$) (Figure 3C). We also assessed the myocyte-specific enhancer factor alpha (MEF2C) α1 and α2, which regulate myoblast differentiation. The Mef2Cα1/Mef2Cα2 ratio in the PLCL scaffold suggested a predominance of Mef2Cα2, favoring myogenic commitment ($p < 0.05$) (Figure 3D). Overall, these findings demonstrate that the PLCL scaffold significantly enhances myogenesis, driving substantial changes in key genes involved in the differentiation process.

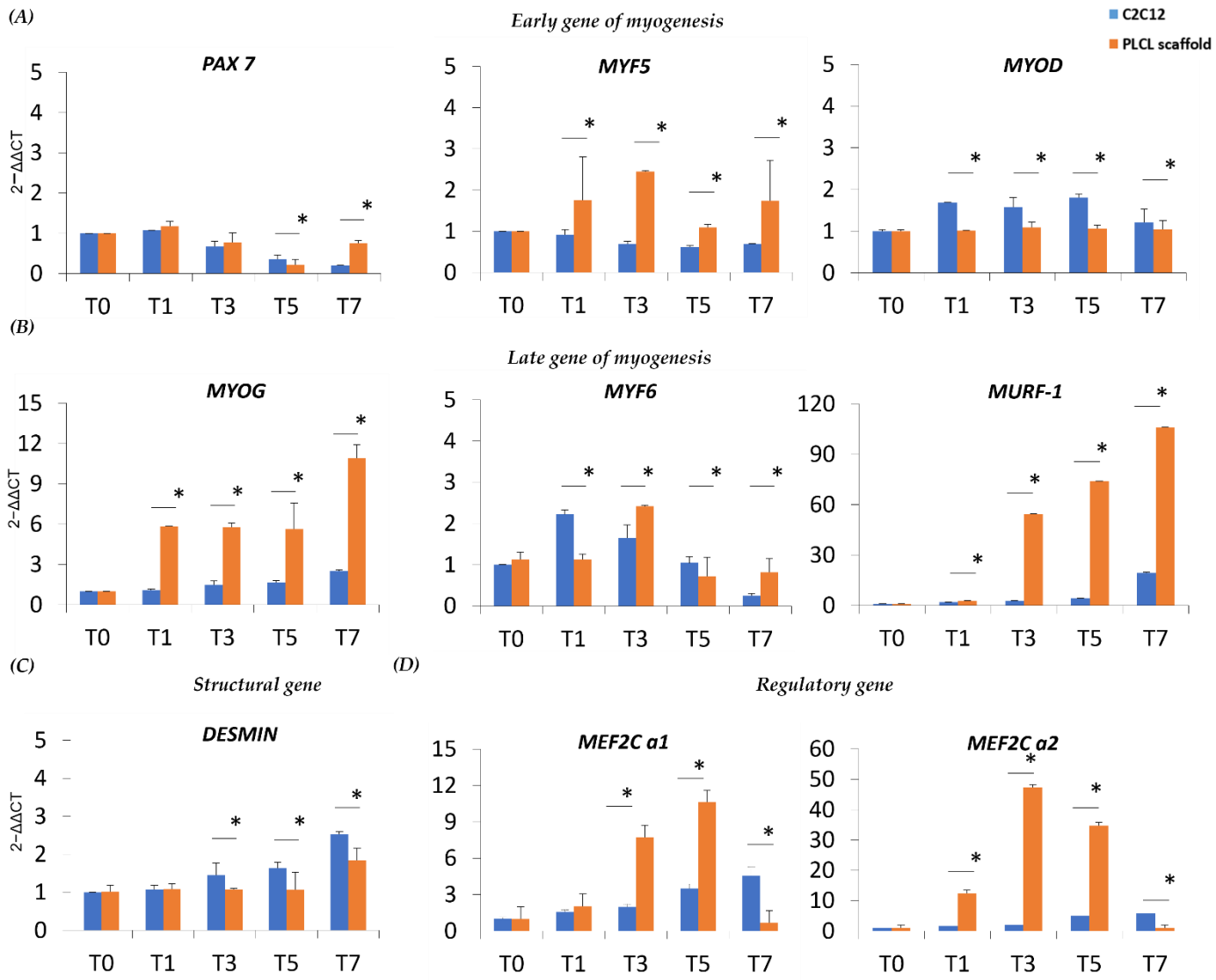

Figure 3. Real-time q-PCR of MRFs, muscle-specific proteins and MEF transcript levels in C2C12 on the scaffold and C2C12 control during myogenic differentiation. (A**)** Transcript levels of early myogenic regulatory factors (MRFs) measured immediately after 24 hours of differentiation (T1), during differentiation (T3–T5), and at later stages (T7). (B) Transcript levels of late MRFs at T1, T3–T5, and T7. (C) Expression levels of a structural gene at T1, T3–T5, and T7. (D) Expression of myogenic enhancer factor (MEF) at T1, T3–T5, and T7. * Data are representative of three independent experiments, presented as means ± SD, with significance set at $p < 0.05$.

Assessment of Myogenesis via Confocal Imaging and Western Blot Analysis

To gain insight into the myogenesis occurring within the cell-laden PLCL scaffold, we performed confocal imaging of fluorescently stained myosin heavy chain 1 (MyHC-1). MyHC-1, a muscle-specific protein, began to be expressed from T5 to T10 [35]. At T0, undifferentiated C2C12 cells showed no positivity for MyHC-1, although a few differentiated cells were positive for MyHC-1 on the scaffold (Figure 4A). These observations align with our previous *in vitro* findings, underscoring

the role of the PLCL scaffold in guiding C2C12 morphogenesis and accelerating cell differentiation. By T1, an increase in MyHC-1 positive cells was noted on the PLCL scaffold (Figure 4B). At T3, we observed fused myocytes and a few myotubes (Figure 4C), while by T5, mature myotubes were widespread across the scaffold (Figure 4D). Although T5 is typically considered an intermediate stage of myogenesis *in vitro*, with the PLCL scaffold, it marked the final stage of differentiation. Stable myotubes were present at T7, with a reduction in MyHC-1 positivity, supporting the notion of an accelerated differentiation process (Figure 4E). Western blot (WB) analysis further confirmed that C2C12 cells on the scaffold exhibited a consistent expression of MyHC-1, whereas the control only showed MyHC-1 expression from T5 to T10 (Figure 4F). Overall, the PLCL scaffold facilitated the maturation of myoblasts within 5 days, demonstrating a significant acceleration compared to the control.

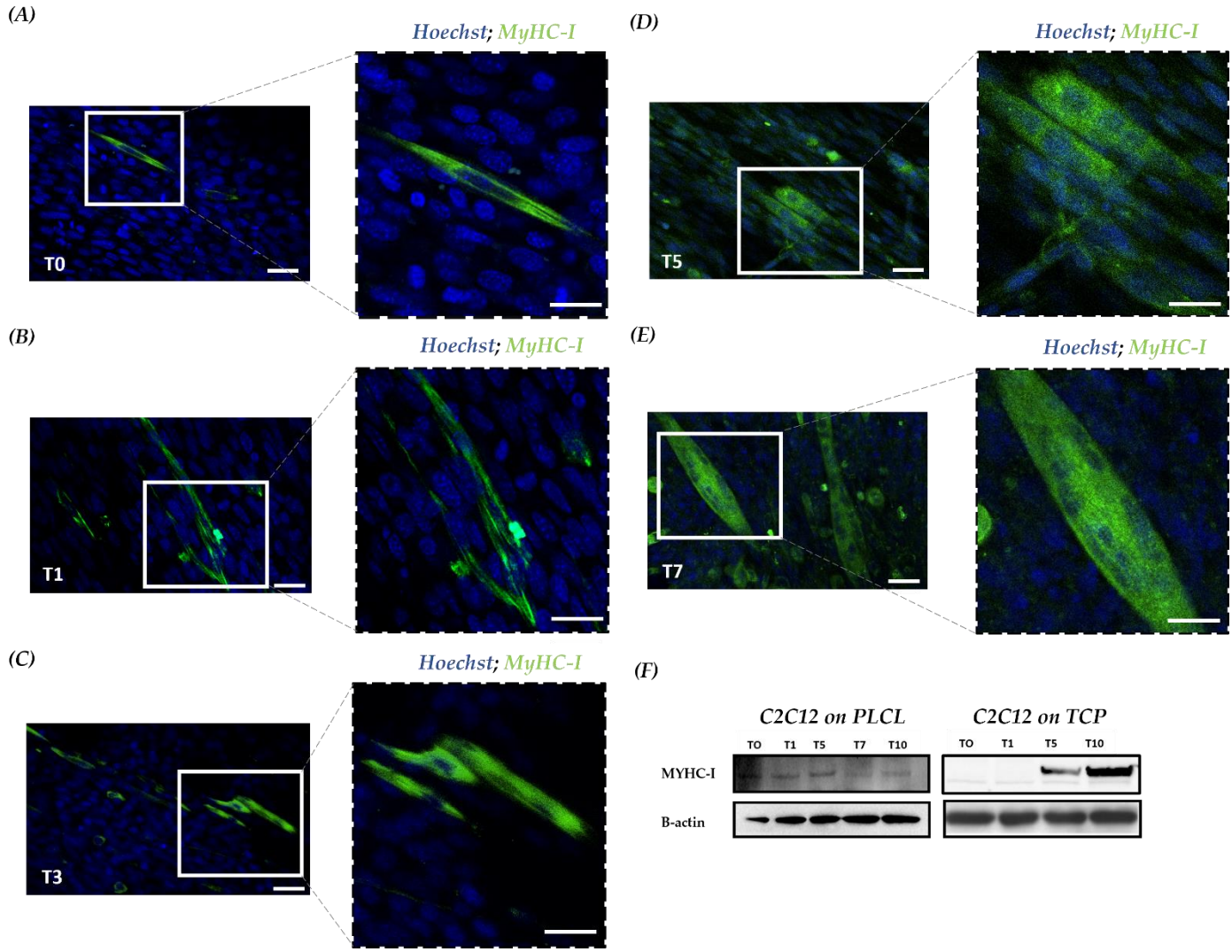

Figure 4. Confocal microscopy with immunofluorescence staining was used to investigate MyHC-1 expression in cell-seeded scaffolds. MyHC-1 is indicated in green, while nuclei are counterstained with DAPI in blue. (A) At T0, undifferentiated cells show only blue nuclei, with no cytoplasmic MyHC-1 staining. (B) At T1, there is a progressive increase in the number of differentiated cells

positive for MyHC-1. (C) At T3, both undifferentiated cells and fused myocytes begin to form initial myotubes. (D) At T5, there is an observable increase in myotube formation. E) At T7, mature multinucleated myotubes are evident. (F) Western blot analysis of MyHC-1 in total protein fractions, with bands quantitated by normalizing MyHC-1 levels to actin. Data are representative of three experiments and presented as means.

Morphological Changes of C2C12 Myoblasts on PLCL Scaffolds During Myogenic Commitment: A SEM Analysis

Given the potential influence of the PLCL scaffold on C2C12 morphogenesis, we investigated the morphological changes of C2C12 during myogenic commitment using SEM. At T0, the images revealed myoblasts aligned according to the scaffold's orientation. Notably, membrane structures facilitating interactions and adhesions between myoblasts were observed (Figure 5A). By T1, there was an increase in these membrane structures, suggesting that the scaffold's topography and the elasticity of PLCL enhanced cell–cell interactions through adhesions and connections (Figure 5B). At T5, we saw that fused myocytes had formed mature myotubes, with a decrease in cell–cell adhesion (Figure 5C). By T7, myotubes had become wider, and the number of membrane structures had significantly reduced (Figure 5D). These findings indicate that growing C2C12 on a tissue-like matrix fosters more physiologically relevant cellular interactions and activates intracellular signaling pathways.

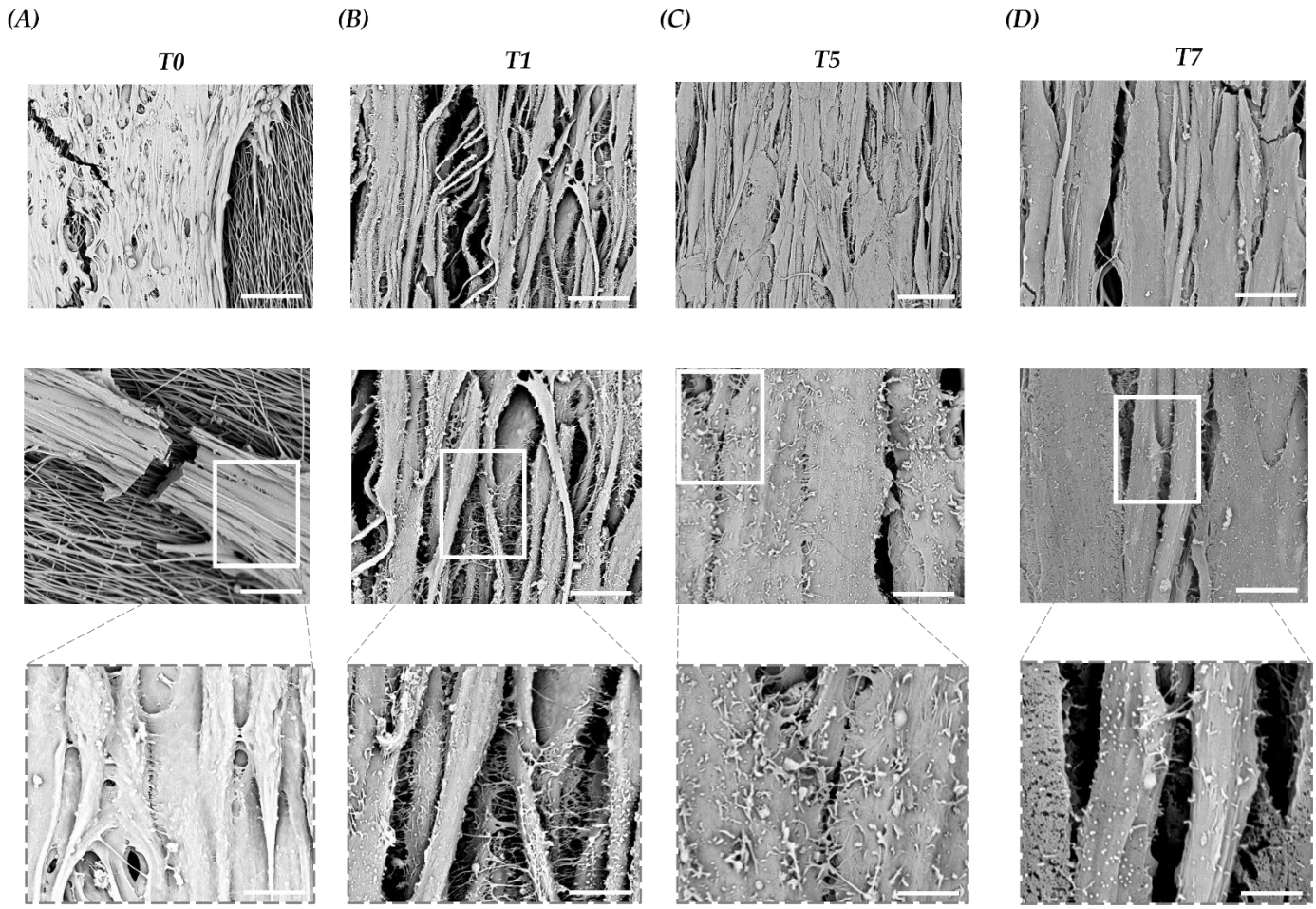

Figure 5. Representative SEM Images of C2C12 Cells on a Scaffold at T0 and During Differentiation (T1–T7) (A) At T0, aligned C2C12 myoblasts are focused on cell–cell interactions and membrane structures. Scale bars: 50 µm, 15 µm, and 5 µm. (B) At T1, C2C12 myocytes exhibit increased cell–cell adhesion and enhanced membrane structures. Scale bars: 15 µm, 5 µm, and 2.5 µm. (C) At T5, myocyte fusion is evident with developing myotubes and reduced membrane structures. Scale bars: 15 µm, 5 µm, and 1.5 µm. (D) At T7, myotubes are enlarged with further reduction in membrane structures. Scale bars: 10 µm, 5 µm, and 1.5 µm.

Discussion

Skeletal muscle (SKM) is a widespread organ in the body, and its dysfunction or impaired regeneration can lead to various SKM disorders and disabilities (Liu J. et al., 2018). SKM tissue comprises specialized cells grouped into muscle fibers formed by the fusion of myocytes derived from precursor myoblasts. Intricate signaling pathways regulate the development of SKM; however, the interactions between myoblasts, myocytes, and myotubes during myogenesis remain inadequately explored (Chak J. et al., 2017). Tissue engineering (TE) approaches for creating muscle-like tissues provide a promising alternative to conventional *in vitro* and *in vivo* studies, addressing their limitations. Scaffolds are crucial in skeletal muscle tissue engineering (SMTE) as they must persist long enough to support functional SKM development (Semplicini C. et al., 2018, Ulery B.D et al., 2011). To accurately reproduce SKM, we designed a scaffold using biodegradable and biocompatible polymeric fibers with high alignment achieved through electrospinning (ESP) (Aviss K. et al., 2020, Cronin E.M. et al., 2004, Huang A.J et al., 2006). We selected PLCL, an aliphatic polyester among various biopolymers, based on its mechanical properties, choosing PLCL 70/30 for its optimal elastic modulus of approximately 14.5 Mpa, which closely mimics the native tissue environment necessary for myogenic differentiation (Engler A.J. et al., 2006). To further enhance SKM functionality, we coated the PLCL scaffold with collagen to improve cell adhesion and replicate a tissue-like environment (Wu T. et al., 2017). After establishing the scaffold's nanostructure and chemical composition, we investigated the signaling pathways regulating SKM development, focusing on how they influence myoblast morphology and activity (Bacakova L. et al., 2004). Studying myogenesis using a myoblast cell line is crucial for monitoring the stages from single myoblasts to elongated myocytes and fused myotubes, ensuring the development of SKM similar to that *in vivo*. In this study, we employed the C2C12 murine myoblast cell line to assess the cytocompatibility of our scaffold, a critical step in biomaterial development. Cell viability tests showed that C2C12 myoblasts cultured on the PLCL scaffold exhibited a similar proliferation rate to those cultured on tissue culture plastic (TCP). Scanning electron microscopy (SEM) analysis revealed that the scaffold's topography guided C2C12 morphogenesis. Notably, within 2 hours, undifferentiated cells were attached to the scaffold; by 6 hours, they had elongated, and within 24 hours, they covered the nanofibrous substrate with a confluent cell layer. These observations corroborate previous studies (Choi J.S et al., 2008, Narayanan N. et al., 2020) demonstrating that the scaffold's contact guidance facilitates cell adhesion, orientation, and elongation, promoting the organization of C2C12 cells. This method enabled us to analyze key stages prior to tissue formation and observe how immature myoblasts interact with the scaffold without external induction (Li H. et al., 2011). Understanding how myoblast differentiation is driven is essential for identifying factors

significantly contributing to SKM development under various conditions. Our analysis of gene expression during differentiation showed that the early regulatory gene Myf5 was more abundant in C2C12 on the scaffold compared to the control. Myf5 collaborates with MyoD to initiate myoblast determination and regulate downstream genes such as MyoG, which were upregulated in C2C12 on the scaffold. The increased expression of Myf5 and MyoG suggests that the PLCL scaffold facilitates early myogenic commitment. Subsequently, MyoD and MyoG suppress Myf5 expression and promote Myf6, which is involved in mature SKM development; therefore, earlier Myf6 expression on the scaffold was expected. Additionally, we evaluated the myocyte-specific enhancer factor alpha factors (MEF2C), focusing on the ratio between Mef2Cα1, which represses muscle-specific genes, and Mef2Cα2, which supports myoblast differentiation (Collinsworth A.M. et al., 20022, Badodi S. et al., 2015) The predominance of Mef2Cα2 in C2C12 on the scaffold indicated enhanced myoblast maturation. The structural gene desmin, a key intermediate filament protein in SKM, showed similar expression patterns under both conditions, confirming that the scaffold modulates differentiation without altering essential protein structures. We also assessed the expression of MURF-1, an autophagic marker indicating advanced stages of myogenesis and cell death (Witt S.H et al., 2005), which was found to be overexpressed in the PLCL scaffold compared to the control. This supports our hypothesis that the scaffold positively influences myoblast behavior by promoting early differentiation. Our findings demonstrate that the 2D cell culture approach is inadequate for studying tissue formation due to its poor representation of *in vivo* conditions. In line with genetic profiles, the earlier expression of MyHC-1, as observed through immunofluorescence (IF) and Western blot (WB), indicated a more pronounced and accelerated cell commitment with effective myoblast-to-myotube formation within a shorter time frame. The PLCL scaffold facilitated C2C12 myogenesis, evident from high and early expression levels of myogenic regulatory factors and downstream signaling, as shown by desmin and MyHC-1 patterns. SEM analysis of undifferentiated and differentiated C2C12 highlighted interactions between myoblasts, revealing microvilli-like structures that form bridges between cells (McClure M.J et al., 2019, Gorbe A. et al., 2005, Gorbe A. et al 2005, Srinivasan S.P. et al., 2012). These structures were notably present after 1 day of differentiation, with significant reductions observed by T5 and absent by T7. This underscores the role of material cues in both biophysical and biochemical aspects, enhancing SKM tissue development in a shorter time. We demonstrated that cells grown in an appropriate microenvironment form cell–cell bonds and release molecules that activate signaling pathways essential for SKM maturation. As myogenic maturation and differentiation are completed, microvilli-like structures gradually disappear, revealing a less-understood mechanism (Cosgrove B.D. et al., 2016, Suzuki K. et al., 2001). Recent research indicates that cell adhesions regulate

myogenesis through factor transfer, signaling activation, and cytokine secretion (Charrasse S. ET AL., 2003). Our study showed that cells rely on membrane structures for transitioning from myoblasts to mature myotubes, with ongoing research to explore cell–cell adhesions and the effects of released molecules. Overall, this study highlights the benefits of growing C2C12 on a collagen-coated electrospun scaffold from both morphological and molecular perspectives, suggesting that the PLCL scaffold provides an optimal microenvironment for fabricating physiological *SKM In vitro*. The detailed gene and protein analysis, combined with SEM results, demonstrates how scaffold-enhanced myoblast fusion synchronizes with the development of cell–cell adhesions, activating essential signaling pathways during myogenesis (Pagnotta G. et al., 2020). Although tissue engineering faces challenges in fully replicating native tissue complexity, recent advancements in creating hierarchical tissue scaffolds (Gotti C. et al., 2020) may revolutionize regenerative medicine (Guex A. et al., 2012). Our results show that scaffolds designed to mimic the desired tissue microenvironment represent an effective tool for studying myogenic differentiation, significantly improving the differentiation and maturation process to create physiological SKM tissue *in vitro*. Future studies will investigate the role of mechanical transduction in SKM formation and conduct i*n vivo* experiments to develop functional SKM tissue. Despite the challenges of *in vivo* applications, tissue engineering offers a novel strategy for *in vitro* tissue formation and functional testing, providing a cost-effective and detailed approach to studying tissue development and myogenesis

1.2. Controlled *in vitro* electrostimulation assays of a myoblast cell line cultured on ion-permeable electrospun poly(L-lactide-co-ε-caprolactone) scaffolds.

Introduction

Severe loss of skeletal muscle (SKM) can arise from various causes such as trauma, surgery, sarcopenia, diabetes, and inherited genetic disorders (Liu et al., 2018). Genetic myopathies, which are hereditary disorders marked by progressive muscle wasting and weakness, currently lack effective therapies (Emery, 2002). Emerging strategies involve a combination of therapies aimed at preserving muscle mass, enhancing muscle maturation, and promoting regeneration. However, a comprehensive understanding of the disease's pathophysiology is essential for discovering effective treatments (Meriggioli and Roubenoff, 2015). Knowledge of muscle cell functions, including contraction responses and contractility development, can serve as indicators for muscle disorders and help identify therapeutic targets while deepening our understanding of pathogenic mechanisms. Investigating the relationship between muscle function and pathology contributes to the advancement of diagnostic tools for preventing or mitigating muscle impairment (Allen et al., 2008). Pioneering studies have demonstrated the potential of "*in vitro* exercise models" using myotubes stimulated by electric impulses (EPS) to explore contractile activity effects (W. Chen et al., 2019). Electric stimulation is well-established for promoting cell proliferation, differentiation, and maturation, thereby supporting SKM functionality (Prabhakaran et al., 2011). An additional motivation for advancing *in vitro* assays is the ethical imperative to reduce reliance on animal testing. They also offer advantages such as scalability and efficient screening of potential therapeutic candidates. By utilizing *in vitro* systems, early-stage drug discovery can be accelerated, and compound selection optimized for clinical applications (Holmes et al., 2010; Krewski et al., 2010). Successful fabrication of *in vitro* SKM requires a mechanically compliant microenvironment, nanostructured cellular orientation, and a controlled electrical system for cellular activity (Abasi et al., 2020; So et al., 2020). In particular, 3D scaffolds enable biomimicry of the natural tissue environment, providing a framework for cellular attachment and proliferation while enhancing cellular differentiation and maturation (Pacilio et al., 2023). A significant technological challenge is the development of advanced 3D scaffolds for *in vitro* cell culture that also incorporate electronic functionality for cell stimulation. Electric fields at cellular positions must be carefully controlled in terms of intensity, timescale, and spatial extent, as these factors influence cellular interactions and responses. The high ionic conductivity of the cell culture medium affects the screening of static electric fields on rapid timescales (<100 μs) due to ionic displacement currents. Therefore, stimulating electrodes must be designed to maintain a persistent ionic current

near the cells. Various approaches have been explored in the literature to generate electrical signals affecting cell phenotype and contraction. Four general approaches are illustrated in Figure 1:

1. Conductive Scaffold with DC Bias (Fig. 1a): This approach involves applying a bias across a conductive scaffold, creating a parallel electric field along the scaffold surface (Hardy et al., 2015; Pires et al., 2015; Sordini et al., 2021). The scaffold's conductivity must be controlled to prevent excessive currents that could overheat cells. DC currents generate a surface potential gradient impacting cell adhesion but do not sufficiently depolarize cell membranes or stimulate cells.

2. Conductive Scaffold with AC Potential (Fig. 1b): In this method, an AC potential is applied to a conductive scaffold relative to the cell culture medium. A bath electrode grounds the medium potential, generating a displacement current orthogonal to the scaffold surface. This current produces electric fields strong enough to activate voltage-gated channels and stimulate cells (F. J. Chen et al., 2021; Das et al., 2020; Ganji et al., 2016).

3. Dielectric Non-Porous Scaffold (Fig. 1c): This approach involves driving ionic currents parallel to the scaffold surface using electrodes positioned on opposite sides of the cell culture surface (Afshar et al., 2020; Dixon & Gomillion, 2023). This configuration is technically simple but may result in poorly controlled electric fields, making stimulation experiments challenging due to surface roughness or cell migration.

4. Dielectric Porous Scaffold (Fig. 1d): Here, scaffold porosity allows ionic currents to flow orthogonally to the scaffold surface (Kaji et al., 2010). The resulting electric fields surround all cells within the scaffold, regardless of their position. To achieve high local current densities, an electrode is placed below the scaffold and driven by a bias relative to the cell culture bath electrode.

In this study, we adopt the porous dielectric scaffold approach. We use electrospinning to fabricate 3D nanofibrous scaffolds of poly(L-lactide-co-ε caprolactone) with high ionic conductivity, enabling the generation of strong electric fields through their surface. Our approach combines controlled electrical stimulation, precisely oriented electric fields with respect to cell alignment, and advanced mechanical compliance to drive cellular contractile activity. We visualize and characterize scaffold actuation, induced by tissue contraction, in real-time using atomic force microscopy (AFM). This work demonstrates how nanostructured multifunctional scaffolds significantly advance *in vitro* assay design, allowing cells to be cultured in conditions that mimic *in vivo* environments and subjected to controlled chemico-physical stimuli, all while observing cellular responses in real-time.

Materials and Methods

Scaffold fabrication (see Materials and Methods pag. 32-33.)

The electrospinning process was performed using a homemade apparatus consisting of a high-voltage power supply (Spellman SL 50 P 10/CE/230), a syringe pump (KD Scientific 200 series), and a glass syringe filled with the polymer solution connected to a stainless steel blunt-ended needle. Uniaxially aligned nanofibers were produced using a rotating collector (metallic drum: length = 120 mm, diameter = 50 mm) at a linear speed of 6000 rpm. Polymer solutions were prepared by dissolving poly(L-lactide-co-ε caprolactone) with a molar composition 70/30 L-lactide/ε caprolactone (PLACL7030) (Corbion, Amsterdam, The Netherlands) in a mixture of dichloromethane (DCM) and dimethylformamide (DMF) (Sigma-Aldrich, St. Louis, MO, USA), DCM:DMF = 65:35 v/v at a polymer concentration of 20% w/v. The polymeric solution was delivered at a constant flow rate of 1.2 mL/h, with a needle-to-collector distance of 20 cm and a voltage of 20 kV. Prior to cell seeding, the electrospun scaffolds were coated with type I collagen solution from calf skin (Sigma-Aldrich, St. Louis, MO, USA). Scanning electron microscopy (SEM) was conducted using a Phenom Pro-X SEM (Thermo Fisher Scientific Inc., Waltham, MA, USA) at an accelerating voltage of 10 kV on gold-sputtered samples. The SEM images were analyzed using ImageJ2, to determine the distribution of nanofiber diameters and pores size, which were reported as the average diameter ± standard deviation (SD).

Cell cultures and viability analysis (see Materials and Methods pag. 33)

C2C12 murine myoblasts (ATCC Cat# CRL-1772, RRID: CVCL 0188) were seeded in a complete growth medium containing Dulbecco's modified Eagle high-glucose medium (DMEM) supplemented with 10% fetal bovine serum (FBS) (Biowest, Nuaille, France), L-glutamine (Euroclone, Milan, Italy), and 1% penicillin/streptomycin. C1C12 were incubated at 37 °C and 5% CO2 until 80% confluence. Subsequently, C2C12 were differentiated by substituting the complete growth medium with a differentiation medium consisting of DMEM supplemented with 1% horse serum (HS) (Sigma-Aldrich, St. Louis, MO, USA). The process of myogenic differentiation was examined at different time points: T0 (0 day of differentiation stimuli) represented the control group of proliferating undifferentiated myoblasts, T5 (5 days of differentiation stimuli) represented the intermediate stage of cell differentiation. The C2C12 cells were cultured at the same density under two conditions: tissue culture plates (TCP) as the control group and scaffolds. Cell viability and proliferation were evaluated using the Cell Titer 96 AQueous One Solution Cell Proliferation Assay

(Promega, Madison, WI, USA). Viability and proliferation experiments were performed at four time points (days 1, 2, 5, and 7), in triplicate.

SEM analysis (See Materials and Methods, pag. 35)

Scanning electron microscopic (SEM) observations were performed using a Phenom Pro-X SEM (Thermo Fisher Scientific Inc.,Waltham, MA, USA) at an accelerating voltage of 10 kV on gold-sputtered samples. SEM observations of C2C12 cultured on scaffolds were performed at 2, 6, and 24 hours of culture for cell morphogenesis analysis. Myogenic differentiation was analyzed at T0 and T5 of differentiation. The scaffolds were fixed as described by S. Pacilio (Pacilio et al 2023). Finally, the scaffolds were processed for SEM analysis following the same procedure described in the Scaffold Fabrication and Characterization section.

Scaffold ionic conductance

The scaffold was mounted in the customized measurement cell, confining the area in contact with the PBS 0.1M electrolyte using a silicone O-ring of 5.0 mm in diameter. A source measure unit (SMU, Keysight B2912) was employed to set the ionic current flowing in the PBS solution, through Ag/AgCl electrodes and agarose salt bridges. The voltage drop across the scaffold was measured in a 4-poin probe configuration to extract the scaffold resistivity.

Cell stimulation chamber

The cell stimulation chamber featured a PLACL 7030 scaffold suspended within a polydimethylsiloxane (PDMS) well with a 10mm hole diameter. The scaffold was positioned between an Indium Tin Oxide (ITO) electrode on a glass surface and a Platinum (Pt) wire, serving as the bath electrode. The compartments below and above the scaffold were filled with phosphate saline buffer. A Keysight B2912 SMU was used to provide current controlled stimuli ranging from 2mA to 10mA. Charge balanced, bipolar stimulation pulses were applied, with a pulse duration of 2 milliseconds. The stimulation protocol consisted of a variable number of successive stimuli, ranging from 2 to 30.

In vitro AFM analysis

To evaluate cell contractility the cell stimulation chamber was placed on the sample holder of a NX10 (Park-Systems) AFM. The liquid probe hand was used to put the AFM tip (HQ:NSC36/Cr-Au BS) in contact with the scaffold (setpoint 12 nN). While feedback was active, the scaffold was stimulated, and the z-scanner height was monitored on an oscilloscope screen. Imaging of the scaffold was done in pin-point mode.

Results

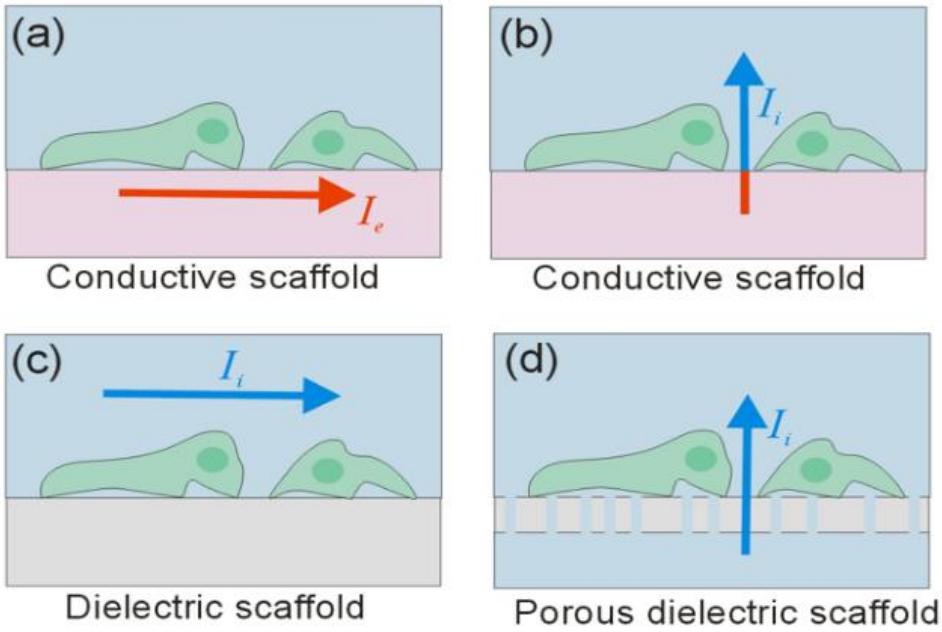

Figure 1: Four different scaffold and electrical stimulation geometries for driving stimulating electric fields on cells. (a) Conductive scaffolds with parallel electrical polarization; (b) Conductive scaffolds with orthogonal electrical polarization; (c) Dielectric scaffolds with parallel electrical polarization; (d) Dielectric porous scaffolds for orthogonal electrical polarization. Red and blue arrows indicate electrical and ionic currents, respectively.

Characterization of Scaffolds: Fiber Alignment, Ionic Conductance, and Mechanical Properties

The poly (L-lactide-co-ε caprolactone) copolymer scaffolds (PLACL7030) were fabricated using electrospinning. SEM micrographs confirmed the presence of aligned and bead-free fibers in the scaffolds (Fig. 2a). Analysis of the fiber diameter distribution revealed an average diameter of 0.7 ± 0.2 μm. Additionally, the pore dimensions ranged from 0.4 to 4 μm, with peak values occurring between 1 and 2.8 μm (Fig. 2b). Previous stress-strain measurements conducted on PLACL7030

nanofibrous scaffolds indicated a relatively elastomeric behavior, with an elastic modulus of approximately 14.5 MPa, which is optimal for mimicking the native microenvironment of muscle fibers (Pacilio et al., 2023). For precisely measuring the ionic current flowing through the scaffold (ionic conductance), the scaffolds were mounted in a customized electrochemical cell in a 4-point probe configuration using PBS 0.1M as the electrolyte solution. The ionic conductance experiment demonstrated the high porosity of the PLACL7030 scaffold and its applicability for cell culture electrical stimulations. The current-vs-voltage straight lines shown in Fig. 2d reveal comparable ionic resistances with (266.67 ± 0.06) Ω or without (243.9 ± 0.3) Ω the 40 μm-thick scaffolds. From these values and using the 0.1M PBS conductivity (σPBS = 13 mS/cm), the scaffold ionic conductivity was calculated to be σScaffold = (0.84 ± 0.02) mS/cm (see Supp. Inf. 1). To complete the scaffold characterization, AFM morphological images were taken in a liquid environment (PBS, see Supp. Inf. 2). The overall fiber morphology and alignment were preserved, although increased fiber diameters indicated water uptake and swelling of the co-polymeric scaffold. The AFM experiments also determined the effective Young's modulus, which is crucial for assessing the scaffold's stiffness in a biologically relevant liquid. Fig. 2e shows force spectroscopy data obtained in the center of the circular free scaffold membrane (r = 5 mm) clamped at its borders. Upon tip indentation, the membrane deformed, resulting in a stiffness of 0.69 nN/nm. Applying plate deformation theory, the effective elastic modulus was calculated to be 52 MPa (see Supp. Inf. 3). This modulus is consistent with earlier tensile stress tests of the scaffold (Pacilio et al., 2023).

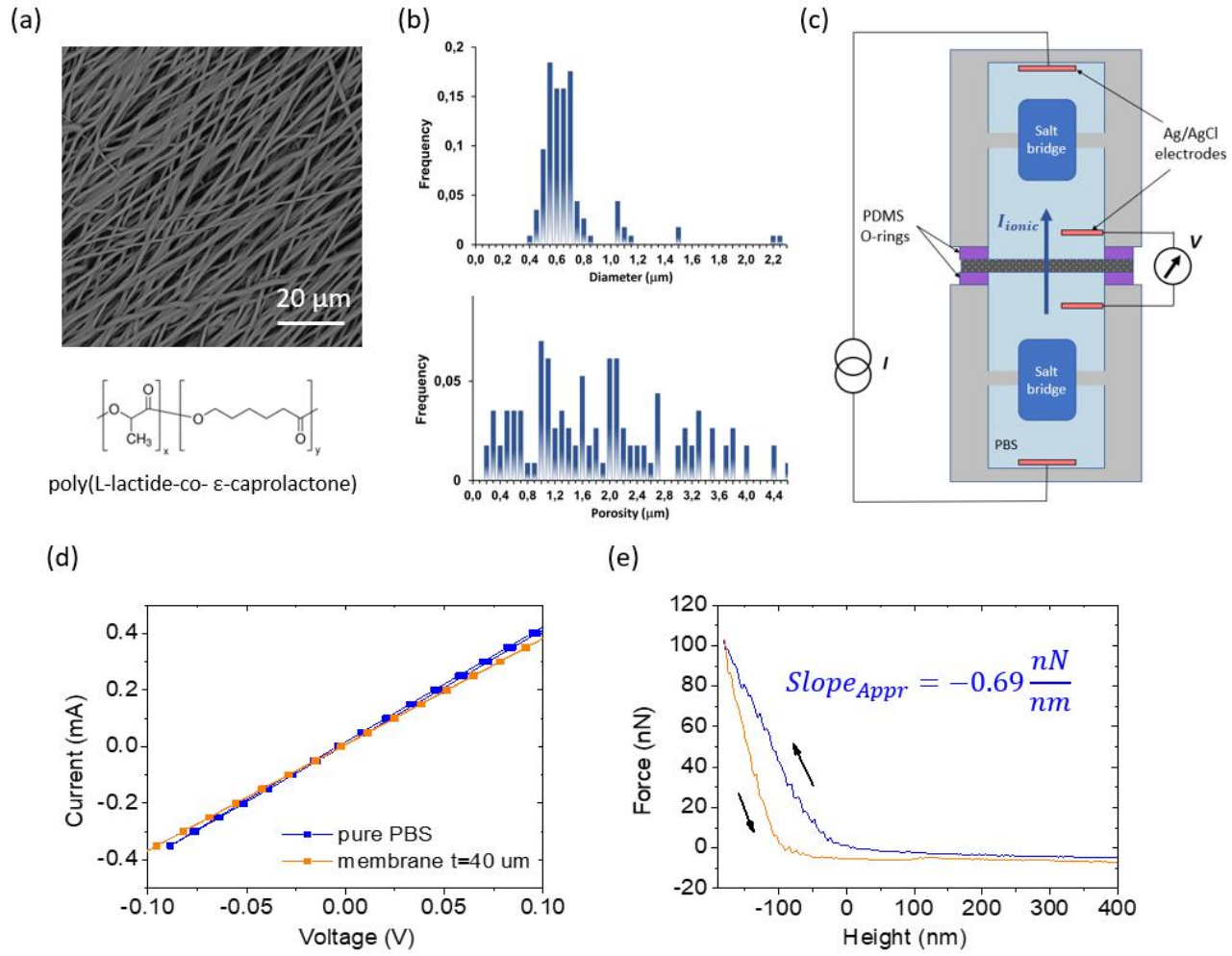

Figure 2: Porous PLCL scaffold characterization. (a) SEM micrograph of the scaffold aligned fibers and chemical formula of the PLCL compound. (b) Fiber diameter (top) and scaffold porosity (bottom) distribution analysis. (c) Schematic cross-section of the 4-point probe experimental setup used to determine the ionic conductance of the scaffold. Through the salt-bridges an ionic current is driven through the membrane. The two Ag/AgCl electrodes are used to measure the voltage drop occurring over the membrane. (d) I-V characteristics for pure PBS (blue) and with the 40 µm-thick membrane (orange) added between the PDMS o-rings. (e) Force as a function of AFM tip height measured in PBS for approach (blue) and retract (orange) curves.

Cell Proliferation, Morphology, and Differentiation of C2C12 Myoblasts on Poly (L-lactide-co-ε caprolactone) Scaffolds

In cell-culture experiments, C2C12 murine myoblasts were seeded and cultured on the scaffolds. SEM analysis of myoblast proliferation revealed the following: at 3 hours, C2C12 myoblasts, initially round in shape due to trypsinization, began to attach to the scaffold. By 6 hours, the cells, adopting a spindle shape, were fully adhered and starting to elongate in alignment with the nanofiber orientation. After 24 hours, the nanofiber surface was entirely covered with elongated

C2C12 cells. Cell viability assays conducted at days 1, 2, 5, and 7 demonstrated the biocompatibility of the scaffold compared to the control on tissue culture plastic. SEM observations of undifferentiated (T0) and differentiated (T5) myoblasts showed that at T0, the cells were single and aligned according to the scaffold orientation, while at T5, they had fused into mature myotubes. These findings confirm the scaffold's cytocompatibility and its influence on C2C12 proliferation, morphology, and differentiation. The results align with previous studies, indicating that the scaffold's nanofiber topography provides effective contact guidance for myoblast elongation and alignment, thus facilitating cell maturation and differentiation.

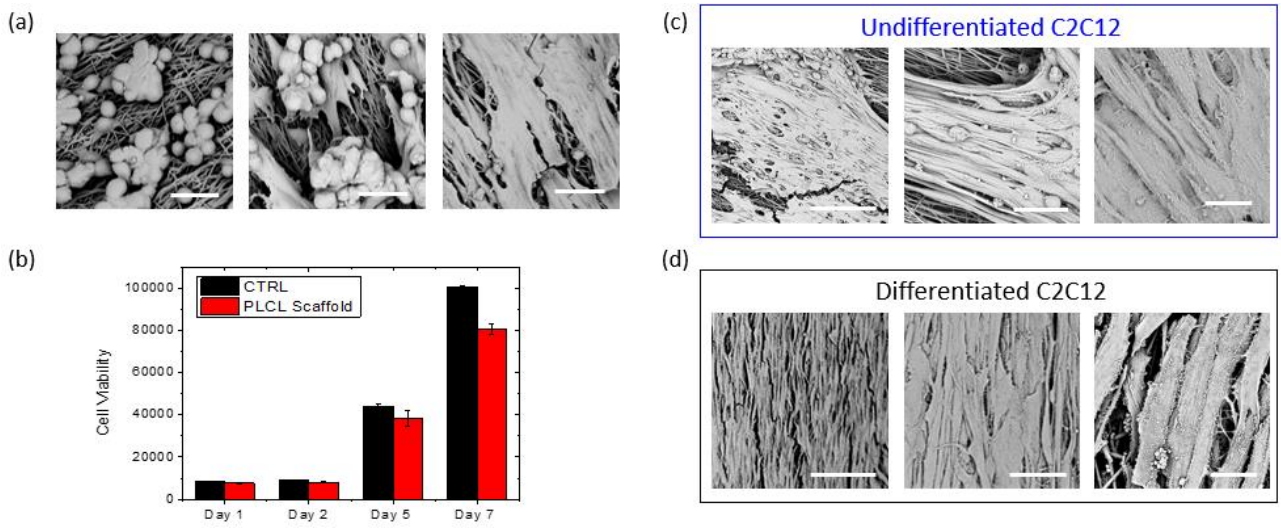

Figure 3: (a) SEM micrographs reporting myoblast proliferation at 2, 6, and 24h (from left to right). White line scale bar = 30 µm. (b) Cell viability over days to evaluate scaffold biocompatibility. SEM micrographs of undifferentiated (T0) (c) and differentiated (T5) C2C12 (d). White line scale bar = 100, 30, and 10 µm (from left to right).

Characterization of Scaffold-Induced Skeletal Muscle Contraction and Contractility in Response to Electrical Stimulation

To monitor muscular cell contractility upon differentiation and electrical stimulation, we employed the AFM tip to sense scaffold vibrations induced by cellular contractions in liquid. The experimental setup involved clamping the circular PLACL7030 scaffold at its borders with a PDMS ring, separating the liquid reservoir into two halves. The lower half space was electrically contacted with an ITO electrode, while the upper half space was in contact with a platinum wire. These electrical contacts were used to drive stimulating current pulses through the scaffold membrane. Displacements of the scaffold membrane were monitored with the AFM tip positioned at the

scaffold center with a constant contact force. The biphasic current pulses and related voltages employed for cell electrical stimulation are depicted in Fig. 4b. Key parameters such as current amplitude, number of stimuli, and stimuli polarity were investigated for their impact on differentiated cell contractility. Scaffold height was monitored by the AFM tip upon 10 bipolar stimulations using different current amplitudes, revealing that: (i) cell contractions induced bell-shaped scaffold height variations with 80ms and 140ms as rising and fall time constants, respectively; (ii) 4mA is the threshold current amplitude below which differentiated cells are not affected by the current stimuli; and (iii) contractility, measured as scaffold height variation, increased with higher currents. In contrast, undifferentiated cells on the PLACL7030 scaffold exhibited constant, null height for all current amplitudes. Increasing the number of stimuli enhanced the cell contraction response, with a linear correlation up to 15 stimuli, beyond which a plateau in height change response was observed. Stimuli polarity did not affect cell contractility. The sensitivity of scaffold actuation to current amplitude was determined as (4.7 ± 0.5) nm/mA, and to the number of stimuli as (3.19 ± 0.08) nm/number of stimuli. The threshold for cell actuation was found to be (3.1 ± 0.4) mA for current intensity and (–1.2 ± 0.4) for the number of stimuli. The minimum electrical field required to induce cell contractility was calculated to be (4.7 ± 0.7) V/cm. Real-time monitoring demonstrated dynamic changes in actuation times aligning with the physiological action potential of skeletal muscle, encompassing phases of depolarization, repolarization, and hyperpolarization. Increased stimuli (20-30) led to twitches summation and tetanic contractile force. These observations indicate the reliability of our *in vitro* assay in mimicking excitation–contraction coupling mechanisms.

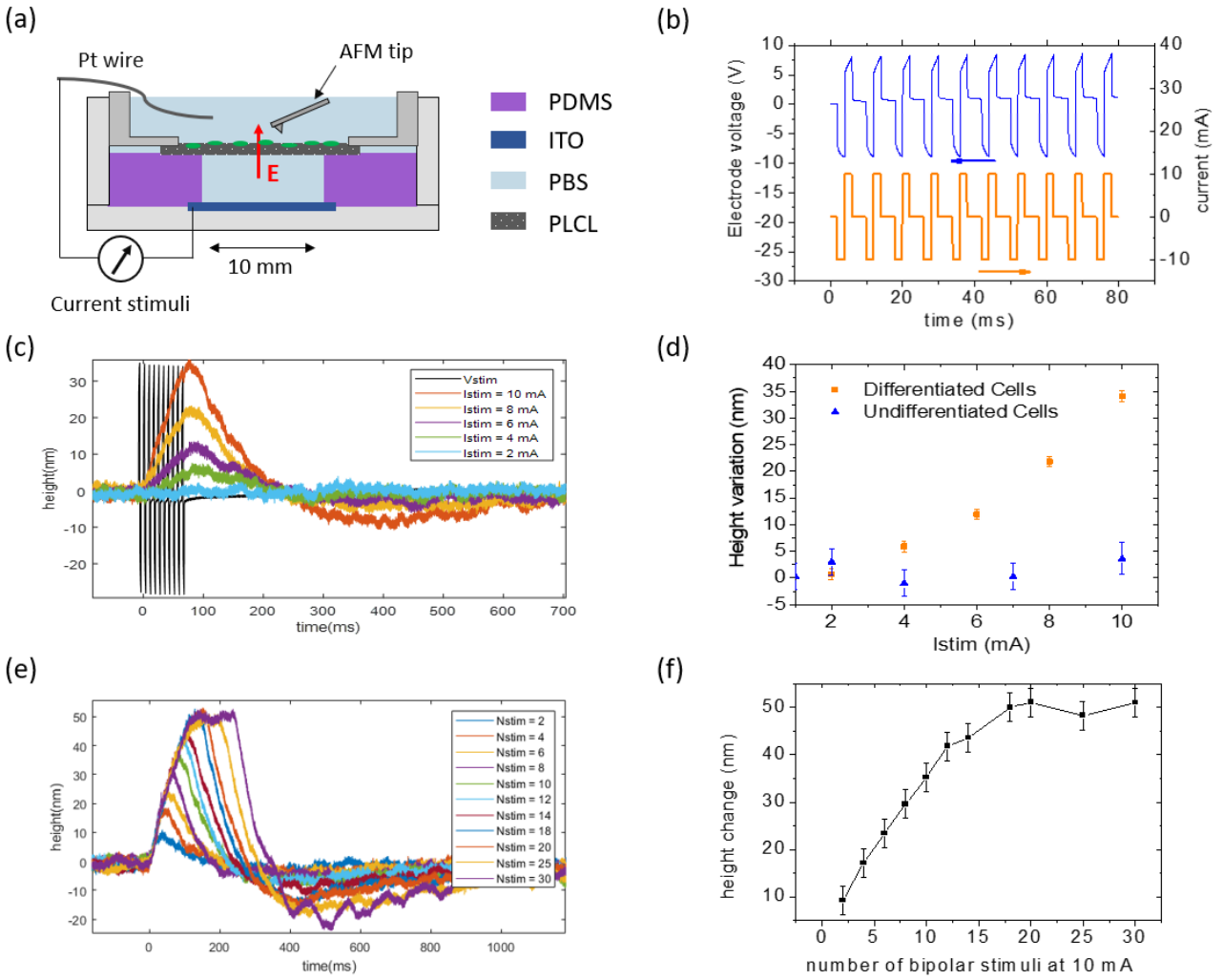

Figure 4: *In vitro* cell contractility evaluation. (a) Cross-section of the experimental setup used for measuring the scaffold deformations induced by myoblasts (in green) grown or differentiated into it, upon the orthogonally oriented electric field stimulations. (b) Example of a current stimulation protocol (set at 10 mA with combined negative and positive polarity). (c) Scaffold height monitored in real-time by the AFM tip upon electrical stimulation using different current amplitudes. (d) Scaffold height variation peaks for differentiated (orange) and undifferentiated (blue) cells in function of the stimulation current amplitude (using a train of 10 current stimuli). (e) Scaffold height monitored in real-time by the AFM tip upon electrical stimulation at fixed 10mA amplitude for diverse number of stimuli. (f) Scaffold height variation peaks for differentiated cells in function of the number of stimuli at a fixed current amplitude of 10mA.

Discussion

The electrospun PLACL7030 scaffold demonstrated well-aligned, bead-free fibers with an average diameter of 0.7 ± 0.2 µm and pore sizes between 0.4 and 4 µm, making them suitable for cell culture applications. The scaffold's elastomeric behavior, with an elastic modulus of approximately 14.5 MPa, was optimal for muscle fiber development. Ionic conductance measurements confirmed

the scaffold’s high porosity and its suitability for electrical stimulation in cell culture. The ionic resistances, both with and without the scaffold, and the calculated ionic conductivity of (0.84 ± 0.02) mS/cm indicate efficient ionic transport through the scaffold.

AFM imaging in a liquid environment revealed that the scaffold maintained its fiber morphology and alignment. The force spectroscopy results further support the scaffold's mechanical relevance for *in vitro* applications, aligning with previous tensile stress tests. The successful fabrication and characterization of the PLACL70/30 scaffold demonstrates its potential for applications requiring structural support and electrical stimulation. Our previous study evaluated the scaffold’s ability to support and guide myoblast behavior, including rapid attachment, elongation, and differentiation into myotubes. The scaffold's biocompatibility, confirmed by cell viability results, further supports its suitability for tissue engineering. The alignment and maturation of myoblasts on the nanofibrous scaffold emphasizes its role in mimicking the natural muscle environment, which is critical for developing functional muscle tissue *in vitro*. In the current study, we further investigated the scaffold’s responsiveness to electrical stimuli and its effects on cell contractility. To monitor muscular cell contractility upon differentiation and electrical stimulation, we employed an AFM tip to sense scaffold vibrations induced by cellular contractions in liquid. The experimental setup involved clamping the circular PLACL70/30 scaffold at its borders with a PDMS ring, separating the liquid reservoir into two halves. The lower half space was electrically contacted with an ITO electrode, while the upper half space was in contact with a platinum wire. These electrical contacts were used to drive stimulating current pulses through the scaffold membrane. Displacements of the scaffold membrane were monitored with the AFM tip positioned at the scaffold center with a constant contact force. The biphasic current pulses and related voltages employed for cell electrical stimulation were analyzed for their effects on key parameters, including current amplitude, number of stimuli, and polarity. AFM monitoring of scaffold height upon 10 bipolar stimulations with varying current amplitudes revealed several important findings: (i) cell contractions induced bell-shaped scaffold height variations with rising and fall time constants of 80 ms and 140 ms, respectively; (ii) a threshold current amplitude of 4 mA below which differentiated cells were not affected by the stimuli; and (iii) an increase in contractility, measured as scaffold height variation, with higher currents. In contrast, undifferentiated cells on the PLACL70/30 scaffold exhibited a constant, null height for all current amplitudes tested. Moreover, increasing the number of stimuli enhanced the cell contraction response, with a linear correlation up to 15 stimuli, beyond which a plateau in the height change response was observed. Stimuli polarity did not affect cell contractility.

The scaffold’s sensitivity to current amplitude was determined as (4.7 ± 0.5) nm/mA, while sensitivity to the number of stimuli was (3.19 ± 0.08) nm per stimulus. The threshold for cell actuation was determined to be (3.1 ± 0.4) mA for current intensity and (–1.2 ± 0.4) for the number of stimuli. The minimum electrical field necessary to induce cell contractility was calculated as (4.7 ± 0.7) V/cm. Real-time monitoring demonstrated dynamic changes in actuation times aligning with the physiological action potential of skeletal muscle, encompassing depolarization, repolarization, and hyperpolarization phases. Increased stimuli (20–30) led to the summation of twitches and tetanic contractile force. These findings underscore the reliability of our *in vitro* assay in accurately replicating the excitation–contraction coupling mechanism of skeletal muscle, providing a robust platform for studying muscle function and response to electrical stimulation. Overall, the PLACL70/30 scaffold's ability to support cell attachment, elongation, differentiation, and contractility under electrical stimulation highlights its suitability for advanced muscle tissue engineering applications. The scaffold's mechanical properties and its responsiveness to electrical stimuli make it a promising platform for developing *in vitro* models of muscle physiology and for investigating therapeutic interventions aimed at restoring or enhancing muscle function. This approach holds significant potential for advancing the study of healthy and diseased skeletal muscle tissues, identifying therapeutic targets, and streamlining drug evaluation and repurposing.

2. Applications of 3D printing in Skeletal Muscle Tissue Engineering

2.1. Muscle 3D Models to Investigate LGMDD2 Transportin 3 Related: Insights into Myogenic Processes

2.2. Development of a Micro-Pillar System for Culturing Functional Human Skeletal Muscle Microtissues: Insights into LGMDD2 Pathophysiology

2.1. Muscle 3D Models to Investigate LGMDD2 Transportin 3 Related: Insights into Myogenic Processes

Introduction

Limb-Girdle Muscular Dystrophy Type D2 (LGMDD2) is a rare autosomal dominant neuromuscular disorder characterized by variable onset and severity, predominantly affecting the pelvic girdle muscles, causing generalized muscle atrophy (Gamez et al., 2001) Central to its pathology is the transportin-3 (TNPO3) gene involved in the nuclear import of serine/arginine-rich proteins essential for mRNA metabolism and splicing (Torella A. et al., 2013; Costa et al.;2020). Considering TNPO3's role in nuclear import, it is hypothesized that disruptions in splicing factor transport and RNA metabolism contribute to muscle pathology (Gibertini et al., 2018). Recent advancements, including CRISPR-Cas9 gene editing, have shown promise in correcting TNPO3 mutations, offering potential therapeutic approaches (Vilchez JJ et al;2023). Despite significant advances in genetic research, the precise mechanisms underlying LGMDD2 remain incompletely understood (Melià et al., 2013). Our study aimed to further explore the role of TNPO3 in LGMDD2 pathogenesis using healthy and patient-derived immortalized myoblast models in 2D and 3D cell cultures. A 3D environment allows for a more physiologically relevant model of skeletal muscle (SKM) tissue compared to traditional 2D cultures. This is particularly important for studying diseases and therapeutic responses, as 3D models provide an accurate representation of how cells behave and interact *in vivo*, leading to more reliable data and potentially more effective treatments (Gungor-Ozkerim et al., 2018). Bioinks such as collagen, alginate, and gelatin are used to create a 3D environment that mimics the extracellular-matrix (ECM), provide the necessary support for cell proliferation, differentiation and the development of muscle-like structures (Pacilio et al;2023, Kang et al., 2020). We chose collagen for our 3D bioprinted SKM model because it is a major component of the SKM extracellular matrix (ECM), providing structural support and promoting cell-cell and cell-ECM crosstalk.(Hauschka S D and Konigsberg I R, 1966, Velleman SG, 1999). Additionally, we included glycoproteins laminin and fibronectin, which are critical for muscle cell attachment, differentiation, and signaling, thereby enhancing the physiological relevance of our model by closely mimicking the native ECM composition (Halper J and l Kjae M., 2014). We examined the role of a 3D collagen bio-printed hydrogel scaffold in SKM myogenesis in healthy and diseased conditions. The 3D collagen bio-printed hydrogel, faithfully recapitulating the native SKM tissue, proved valuable for investigating myogenic processes and understanding the role of the TNPO3 in disease development. Focus was placed on expression patterns of myogenesis-related genes, particularly Myogenic Regulatory Factors (MRFs) like Myf5, Myog, and Myf6, and other

muscle-specific genes. Furthermore, due to their involvement in disease pathogenesis, we investigated the roles of MEF2C and its isoforms α1 and α2, regulated by splicing factors like SRSF1 and RBM4, which are key cargoes of TNPO3. MEF2 genes are critical for muscle development and interact with MRFs. The regulation of MRFs factors involves MEF2 family proteins, which can regulate positively MyoD, MyoG and MRF4, positive feedback and a negative regulation by the same Myf6 (Asfour, H.A et al., 2018). Alterations in MEF2 activity are being implicated in various diseases (Sandmann T. et al., 2006). Further analysis included MyHC isoforms, because myopathic alterations lead to muscle fiber impairment (Angelini C. et al., 2020) As muscle atrophy is a common feature in LGMDD2 patients, we examined the P62 marker and studied the potential activation of autophagic activity by analyzing MURF-1 (Cenacchi G. et al., 2013, Witt S.H et al., 2005). Ultrastructural analysis of LGMDD2 patients revealed peculiar features, thereby, to ensure the reliability of our model, transmission electron microscopy (TEM) was performed. Consequently, LGMDD2 was investigated at the functional level by analyzing SKM contractility, a critical parameter for understanding the pathogenesis of the disease. Therefore, a more sophisticated model, micropillar technology, was utilized to accurately measure muscle contraction dynamics. Gilbert P. et al., 2020 showed how the micropillar method supports the formation of SKM tissue that mimics biological responses and allows for non-invasive contractile force measurements via post deflection analysis. Using this system, we monitored longitudinal muscle contractions in LGMDD2 micropillar 3D model. Our *in vitro* models have significantly contributed to understanding LGMDD2 pathology, highlighting functional impairments during SKM development caused by TNPO3 mutations. Early-stage cell differentiation alterations impact myogenic commitment and, consequently, SKM functionality. The data collected from our study are invaluable for drug discovery and new therapeutic approach for LGMDD2 patients.

Materials and Methods

Cell cultures

2D and 3D immortalized control and LGMDD2 human myoblasts were plated in a growth medium consisted of Skeletal Muscle Cell (C-23160 PROMOCELL), 20% Fetal Bovine Serum (FBS, Biowest, Nuaille, France) and 1% gentamycin (Thermo Scientific) in humidified atmospheric air (5% CO2) at 37 °C. To induce differentiation cells were switched to a medium containing DMEM (Biowest, Nuaille, France) with 10 µg/ml (1%) of insulin (Sigma-Aldrich, St. Louis, MO, USA) and 50 µg/ml of gentamycin antibiotics (Thermofisher Scientific, Waltham, Massachusetts, USA). Myogenic differentiation was induced as follows: T0, proliferating undifferentiated myoblast used

as control; T1, early stage after 24 h of differentiation; T3–T5, intermediate stage after 3–5 days of differentiation; T7–T10, late stage after 7-10 days of differentiation.

Collagen hydrogel preparation

The collagen ink (CI), made of fibrillar type I collagen in its native form derived from equine tendon, was produced using a proprietary process developed by Typeone Biomaterials Srl. It is provided as a ready-to-use sterile suspension at a concentration of 25 mg/mL in a neutral buffered solution (pH 7.4) without the presence or addition of crosslinking agents. Photo-crosslinking of the CI is achieved through UV light irradiation at 365 nm with an intensity of 12 mW/cm² for 2 minutes, maintained at a distance of 3 cm between the sample and the UV lamp.

Rheological characterization

The rheological properties of collagen ink (CI) were evaluated using an MCR 102 parallel-plate rheometer (Anton Paar, Graz, Austria) with a 25 mm diameter plate (PP-25) and a gap of 0.3 mm. All measurements were conducted in triplicate at 20°C to replicate the static conditions of both the pre-printing and post-printing processes. The following oscillatory tests were performed: amplitude sweep, gelation, and an isothermal test. The rotational analysis included flow curves and a three-interval thixotropic test (3ITT), executed in controlled shear rate mode. Input data were configured using the Rheoplus software. Approximately 500 µL of hydrogel was placed onto the rheometer plate with a syringe. The upper plate was then lowered until it contacted the sample surface, and excess material was removed with a spatula. Distilled water was added to the trap to prevent evaporation.

Amplitude sweep analyses were conducted on CI before and after crosslinking across a strain range (ɣ) from 0.01% to 1000%, maintaining a constant frequency of 1 rad/s. This test evaluates the storage modulus (G′) and the loss modulus (G″) as functions of the applied strain (%), determines the linear viscoelastic range (LVE), and identifies the cross-over point (G′=G″), which indicates the stress required to induce flow of macromolecular chains within the hydrogel. All subsequent tests were performed within the LVE.

Gelation test was employed to assess the variation in the sample's rheological properties as a function of temperature. Both angular frequency and strain amplitude were maintained constant at 1

rad/s and 0.1%, respectively, to simulate static conditions. The temperature was initially set at 40 °C and decreased to 4 °C, with a linear ramp of 5°C/min applied. This procedure identified the temperature range where the samples exhibited gel-like behavior, which is crucial for determining printing parameters such as the temperature of the 3D bioprinter's printhead and the substrate.

Isothermal est assessed the time-dependent changes in G′ and G″ by keeping the strain amplitude (0.1%), angular frequency (1 rad/s), and temperature (37°C) constant. This measurement was performed post-crosslinking to evaluate its effectiveness. A 10-minute duration was chosen, with 37°C replicating the incubation conditions to which the printed constructs would be exposed following the printing process. Flow curve tests were carried out over a shear rate range ($\dot{\gamma}$) from 0.1 to 1000 s^{-1}, utilizing a "ramplog + decade" profile with a slope of 6. The flow curves plot viscosity (η) or shear stress (τ) as a function of the applied shear rate. The resulting plots were fitted according to the Ostwald-de Waele mathematical model (Eq. 1) to determine the shear thinning index (p) and the consistency index (C).

$\tau = C\ \dot{\gamma}^{p}$ (Eq. 1)

The 3ITT test was used to simulate the extrusion-based 3D bioprinting process and evaluate the hydrogel's mechanical behavior following exposure to high shear rates. The test was conducted in controlled shear rate (CSR) mode, with the resulting graph depicting viscosity as a function of time. To simulate the resting state of the hydrogel within the syringe prior to printing, a low shear rate (0.1 s^{-1}) was applied at 20 °C. Subsequently, a high shear rate was applied to mimic the material's passage through the syringe nozzle, with the value calculated *according to Equation 2.*

$\dot{\gamma} = \frac{4Q}{\pi r^3}$ (*Eq. 2)*

where Q is the volumetric flow rate and r is the value of the nozzle radius. Q for a nozzle that has the shape of a cylinder was determined using the Equation 3:

$Q = v\ A_l$ *(Eq. 3)*

Where A_l is the lateral area of the section and v represents the flow velocity.

3D Bioprinting

The Bio V1 bioprinter (REGEMAT 3D S.L., Granada, Spain), equipped with an extrusion-based piston-driven system, was utilized under a laminar flow hood to maintain sterile working conditions. The bioprinter system included a dispensing syringe, an XYZ stage with a controller,

and a temperature controller. The 3D constructs were designed using a CAD model integrated with the bioprinter's custom software, and the CAD models were exported as Standard Triangle Language (STL) files to generate G-code files. Bioinks were loaded into syringe barrels equipped with precisely calibrated pistons and 0.58 mm inner diameter (ID) conical tips, which were then placed in the corresponding printheads. Constructs were printed according to the pre-designed geometry within a 24-multiwell plate. Extensive optimization determined the optimal printing parameters, including a nozzle diameter of 0.58 mm and a flow speed of 4 mm/s. The printing temperature was maintained at 20°C to prevent nozzle clogging due to the thermo-responsive properties of GelMA and collagen. All constructs adhered to a pre-designed cylindrical geometry and were arranged in a parallel pattern within a 12-multiwell plate. Following printing, a post-crosslinking procedure was conducted (12 mW/cm², 365 nm, 2 min, at 3 cm) on the three-layer bioprinted constructs to stabilize the structures during incubation at 37°C. For the bioink formulation, 1 mL of type I collagen was mixed with 5 x 10^6 myoblast cells. The optimized collagen bioink formulation was prepared by gently mixing the suspended cells (5 x 10^6) from both human immortalized myoblasts derived from healthy donors (CTRL) and myoblasts from patients affected by TNPO3-related muscular dystrophy (LGMD D2), along with the addition of laminin (SIGMA Aldrich, USA) and fibronectin (SIGMA Aldrich, USA).

RNA isolation and RT-qPCR

Total RNA from 2D and 3D myoblasts was extracted using TRIzol Reagent (Thermo Fischer Scientifc, Waltham, Massachusetts, USA). RNA amount and quality were determined employing Drop ND-2000 (Thermo Fischer Scientific). The complementary DNAs (cDNAs) were synthesized by reverse-transcription using iScript RT Super Mix cDNA. RT-qPCR was performed exploiting CFX Connect™ Real-Time PCR Detection System thermal cycler (Bio-Rad Laboratories, Hercules, CA, USA) and dsDNA MaximaTM SYBR Green qPCR Master Mix 2X (Thermo Fisher Scientific) according to manufacturer’s instructions. 40S Ribosomal Protein S18 (RPS18) was used as the internal control. The expression level of genes was calculated using the 2-ΔCt method. Primers in Supplementary Data

Western Blotting

Pellets from 3D collagen scaffolds were previously treated with collagenase concentrated 1 mg/mL. Both 2D and 3D were lysed in RIPA buffer. Protein samples were separated by 4-12 % Bis-Tris Gels (Invitrogen, Thermo Fisher Scientific, Whaltam, Massachusetts, USA) and electroblotted onto nitrocellulose membranes.The blots were probed with anti-Myosin Heavy Chain (Santa Cruz Biotechnology,1:200), anti-TNPO3-C (Abcam, numero AB1:1000), anti-TNPO3-N (Abcam, Cambridge, UK,1:1000) anti-SRSF1(Thermo Fisher Scientific, ,1:250) anti-Myog,(Santa Cruz Biotechnology, 1:200) anti-MyoD (Santa Cruz Biotechnology, 1:200) anti-RBM4 (Santa Cruz Biotechnology, 1:200) anti-desmin (Santa Cruz Biotechnology,1:200) and anti-p62 (Santa Cruz Biotechnology,1:400) antibodies.

Immunofluorescence

Cells underwent fixation with 4% PFA for 20 minutes at RT followed by 2 × 5-min PBS washes and permeabilization with 0.5% TritonX100/PBS for 10 minutes at RT. Slides were then blocked with 1% PBS/BSA and then incubated in primary antibodies at 4 °C overnight. The following primary antibodies were used: anti-MyHC (Santa Cruz Biotechnology,1:200) anti-SRSF1 (Thermo Fisher Scientific,1:200) anti-TNPO3 (Abcam,1:250), anti-p62 (Santa Cruz Biotechnology,1:250), anti-alpha actinin (Santa Cruz Biotechnology,1:500). Samples were then incubated in suitable secondary antibodies anti-mouse IgG antibody (1:1000, ThermoFisher Scientific, cat. no.), goat anti-rabbit IgG antibody (1:1000, ThermoFisher Scientific, cat. no.) 1h at RT. Immunofluorescent images were captured using Nikon A1 confocal laser scanning microscope equipped with a 40×, 1.4 NA objective and with 405 and 488 nm laser lines. Quantification was performed with ImageJ.

Transmission electron microscopy

Myoblasts pellet obtained by cells trypsinization and centrifugation for 5 min at 12000 rpm, was fixed in 2.5% glutaraldehyde in cacodylate buffer to settle the protein component, postfixed in 1% OsO4 to fix the lipidic component. Then dehydration was performed in graded ethanol, passages in acetonitrile were carried out to ensure final embedding in araldite. Semithin sections were stained in toluidine blue. Thin sections, stained with uranyl acetate and lead citrate, were examined with a

Philips 400T transmission electron microscope.

Statistical analysis

GraphPad Prism 8 was used for statistical analysis. T-TEST comparisons were used with just two pair of conditions and the level of significance was as follows: $p < 0.05$

Results

3D bio-printed collagen scaffold fabrication and characterization

Collagen is extensively studied as a biomaterial in extrusion-based bioprinting (EBB) due to its favorable biological and mechanical properties. A comprehensive rheological screening was conducted to evaluate the material's mechanical properties throughout the printing process. Collagen's shear-thinning behavior, which influences its printability, was assessed through rotational measurements, with results displayed in Figure 1 (A - B). The data shows viscosity (η) and shear stress (τ) as functions of shear rate. A typical shear-thinning behavior, characteristic of printable materials, was observed, as viscosity decreased from 560 Pa·s at 0.1 s^{-1} to 0.14 Pa·s at 1000 s^{-1}. The Ostwald-De Waele regression (Eq. 1) was applied to the viscosity curve (red line in Fig. 1(A)) at medium shear rates, yielding a shear-thinning parameter (p) of 0.11 and a consistency index (C) of 80.62 Pa·s, confirming the shear-thinning properties of uncrosslinked collagen ink (u-CI). A p-value below 1 indicates shear-thinning behavior, with lower p-values reflecting more pronounced shear-thinning. The consistency index (C) provides insight into the material's flow and deformation characteristics, with higher values indicating better preservation of the printed structure. Figure 1(B) presents a shear stress vs. shear rate graph, providing insights into the shear stress experienced during the bioprinting process, which will affect embedded cells. According to Equation 2 (see Material and Methods), a flow rate of 3 mm/s through a nozzle with a diameter of 0.41 mm and height of 1 mm results in a shear rate of 300 s^{-1}, corresponding to a shear stress of 150 Pa, a value considered safe for cells in the hydrogel (Lemarié L. et al., 2021, Blaeser A. et al., 2016). The entire printing process was simulated using a 3ITT test, predicting the hydrogel's behavior before, during, and after extrusion. A low shear rate (0.01 s^{-1}) simulated the static conditions inside the syringe and post-extrusion, while a high shear rate (300 s^{-1}) simulated the extrusion process, calculated using Equation 2. As shown in Figure 1(C), collagen exhibited viscosities of 442 Pa·s and 375 Pa·s before and after extrusion, respectively, while approaching zero viscosity during extrusion. This behavior confirms that collagen

hydrogel can be easily extruded at 20°C, regaining 85% of its initial mechanical properties post-extrusion, making it suitable for bioprinting. Gelation tests were performed to evaluate the temperature-dependent rheological properties of u-CI. A temperature ramp from 4°C to 40°C revealed a slight decrease in the rheological moduli (Figure 1(D)). At 20°C, the material exhibited gel-like behavior, with a G′ of 605 Pa and a G″ of 93 Pa, establishing 20°C as the optimal printing temperature. However, this formulation is expected to maintain its gel-like behavior across a broader temperature range. The viscoelastic properties of the collagen suspension were further assessed using an amplitude sweep test. Figure 1(E) shows that u-CI exhibits gel-like behavior, with G′ (425 Pa) exceeding G″ (70 Pa). The linear viscoelastic (LVE) range was maintained up to 6% strain, with the crossover point occurring at 50%, beyond which the material behaved like a liquid. To enhance collagen's stability, crosslinking was performed using UV light, capitalizing on collagen's inherent photo-responsiveness (Shirahama H. et al., 2016). Rheological analysis of crosslinked collagen (c-CI) revealed a modest increase in G′ (585 Pa) and G″ (85 Pa) after crosslinking (Figure 1(D)), along with a more pronounced G″ peak. The crossover point remained at 50%, and the LVE range extended from 0.1% to 7%. These results confirm that UV light induces further crosslinking of the collagen chains.

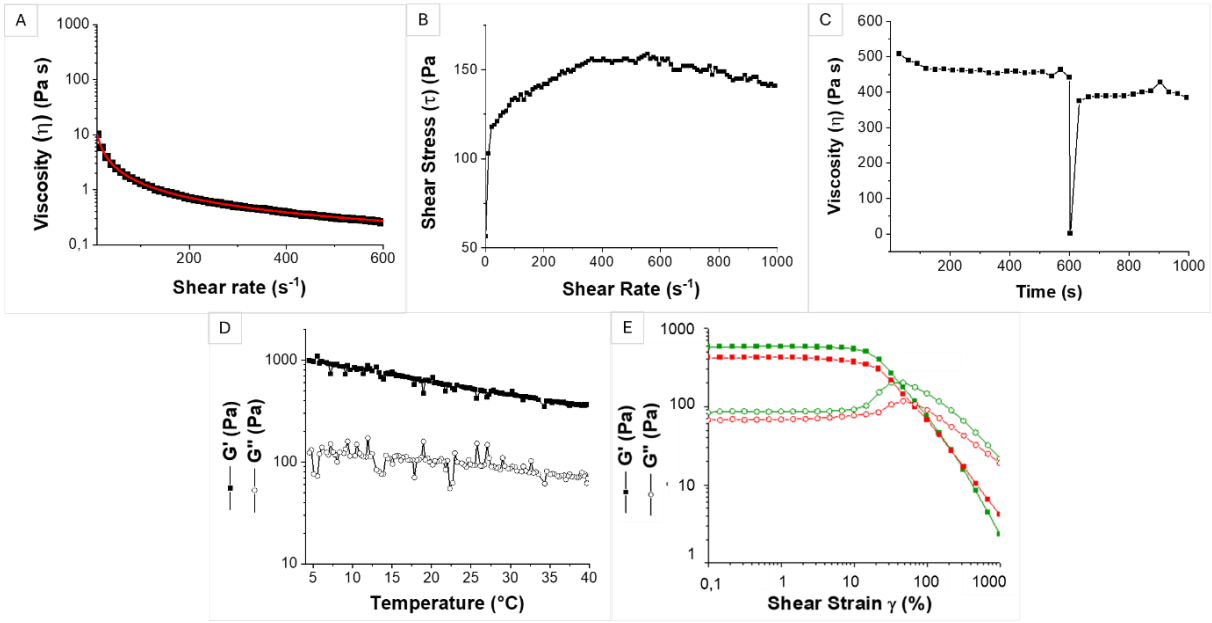

Figure 1. Rheological characterization of collagen hydrogel formulation. (A) Viscosity curve of u-CI fitted with Ostwald-De Waele model (red line); (B) Flow curve of u-CI; (C) Three-interval thixotropic test (3ITT) of u-CI; (D) Gelation measure of c-CI; (E) Amplitude sweep test of u-CI (red curves) and c-CI (green curves).

Printing tests were performed to evaluate the material's uniformity ratio and printability (Pr). The initial qualitative assessment of hydrogel printability involved observing the preservation of filament structure post-extrusion (Figure 2A). Following this, quantitative measurements were obtained by printing a 2 cm diameter grid for both hydrogels, as shown in Figure 2B). The uniformity ratio for crosslinked collagen (c-CI) was determined by comparing the expected filament length to the actual printed length, accounting for surface roughness. The uniformity ratio for c-CI (pink grid) was 0.96 ± 0.02, indicating good consistency in the printed filament. Printability values, calculated using Equation 4, were 0.91 ± 0.02 for c-CI. In general, a Pr value of 1 corresponds to a perfect square, signifying high shape fidelity and proper maintenance of the extruded filament's form (Zhao C. et al., 2021).

$$Pr = L^2/16\,A \qquad \text{(Eq. 4)}$$

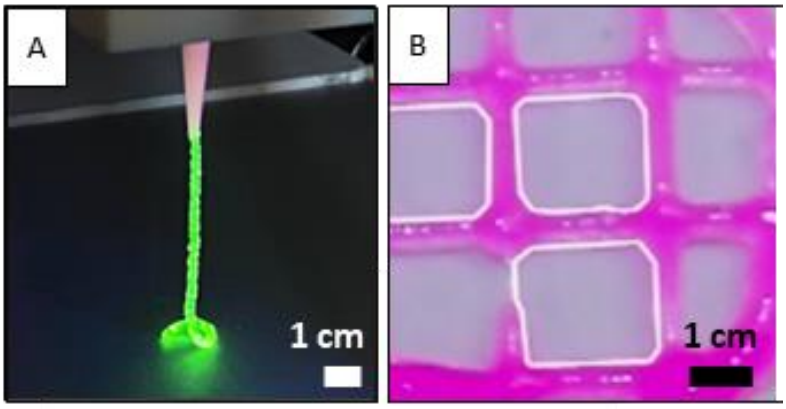

Figure 2. (A) Extruded filament of CI stained with fluorescein; (B) Printed c-CI (pink)

Once the optimal ink conditions were established, printing parameters were optimized for stable constructs. Cylindrical diagonal constructs with a diameter of 15 mm, a layer height of 0.58 mm (total of 3 layers), and a printing temperature of 20 °C were used. The flow speed was set at 4 mm/s, and the travel speed at 5 mm/s using a 0.58 mm diameter needle to prevent nozzle clogging (Table 1). Multiple constructs were successfully printed with embedded myoblast cells in the collagen matrix using 3D-bioprinting. These optimized printing conditions provide a solid foundation for conducting biological tests on the printed constructs, demonstrating the potential for further advancements in tissue engineering and regenerative medicine.

Table 1. 3D Bioprinting conditions, scaffold geometry and crosslinking condition

Multiwell 12	3D BIOPRINTING CONDITION					PHOTO-CROSSLINKING		
	Nozzle	Flow Speed	Infill Pattern	Geometry	T	UV dist.	UV time	UV int.

Collagen Bioink	0,58 mm	4 mm/s	Diagonal Angle: 90° Range:3	LH: 0,58 mm H: 1,74 mm D: 15 mm 3 layers	20 °C	3 cm	2 min	12 Mw/cm^2

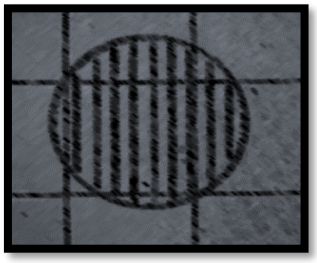

Figure 3. CAD Design of 3D Bioprinted constructs

Investigation of gene expression on 2D and 3D cultures

The immortalized myoblasts cell line, both the control one and the LGMDD2 TNPO3-related are induced to differentiate through a specific differentiation medium replacement. The expression level of genes encoding for myogenic regulatory markers (MRFs) Myf5, Myf6, Myog, muscles atrophy and autophagy markers Murf-1 and P62, muscle specific proteins such as Desmin, MEF2C α1/α2 and LGMDD2 related-proteins TNPO3, RBM4, SRSF1, PTB was performed. They were evaluated through RT-qPCR to better understand their activity during myogenic commitment both on 2D cultures and collagen 3D scaffolds, in turn comparing controls and LGMD D2 myoblasts. An evaluation of the expression levels of genes directly and indirectly involved in myogenesis, myogenic regulatory markers (MRFs) Myf5, MyoD, Myf6, Myog, muscle-specific protein Desmin and myocyte enhancer factors MEF2C α1/α2 was performed. Myf5, an early marker of the myogenic process, showed a 2- to 3-fold higher expression in 2D LGMDD2 myoblasts during early differentiation compared to CTRL, with a gradual decrease as differentiation proceeded but with higher expression than CTRL. In contrast, 3D scaffold displayed a progressive increase in Myf5 expression, particularly under LGMDD2 conditions in the late differentiation stages, reaching a 4-fold increase at T10 compared to CTRL (Fig. 1A). Myf6, which encodes an additional MRF factor directing myogenic specification along with Myog and Myod, exhibited constant expression levels over time in 2D myoblasts for both CTRL and LGMDD2. However, LGMDD2 consistently showed statistically higher levels throughout differentiation. In 3D scaffold, CTRL maintained constant levels from T0 to T5, with an almost 3-fold increase at T10. LGMDD2 also peaked at T10, displaying statistically higher levels compared to CTRL, similar to the trend observed for Myf5, suggesting their coordinated activity in myogenic specification (Fig. 1A). MyoD was constant over

time, with positivity at late stage in 2D (Fig. 1C). The final differentiation of unfused myoblasts and cell cycle arrest is regulated by MyoG. In 2D culture, transcript expression was null at T0 in both CTRL and LGMDD2; however, protein expression showed upregulation in pathological cells. At both transcriptional and protein levels, 2D LGMDD2 myoblasts increased up to 8-fold from T1 to T10 compared to CTRL. 3D scaffolds mirrored the 2D pattern, showing a statistically significant upregulation in LGMDD2 from T0 to T5 differentiation stages (Fig. 1A-C). In LGMDD2, Desmin displayed a constant upregulated trend from early stages, with a 3-fold and 4-fold increase at T1 and T10, respectively, compared to CTRL (Fig. 1D). MEF2C α1, a suppressor of muscle-specific genes, and α2, an activator of myoblast differentiation, were evaluated. A MEF2Ca1-MEF2Ca2 ratio was calculated, values lower than 1 point out an inhibition of the differentiation and viceversa. In both 2D and 3D CTRL conditions early differentiation stages showed a >1 ratio, that decreased at T5-T10. Conversely, LGMDD2 express <1 ratio in 2D and 3D model, increasing in the late stages (Fig.1E)

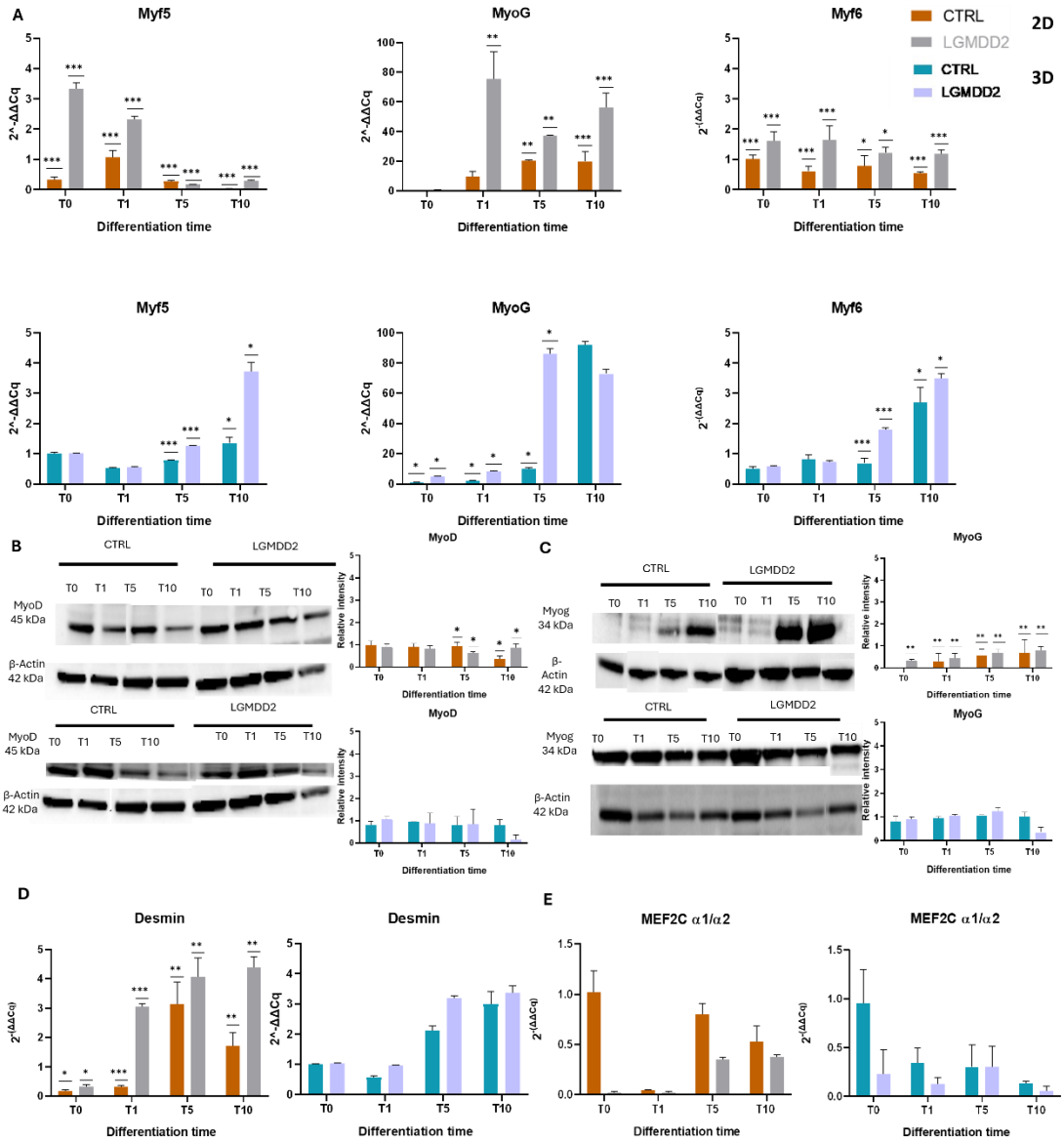

Figure 1. Graphic representation of myogenesis regulators relative gene expression (*Myf5, MyoG, Myf6, , DESMIN, MEFα-1, MEFα2)* levels evaluated by Real Time q-PCR at T0-T1 (early stages), T5 (intermediate stage) and T10 (late stage) of myogenic differentiation in both 2D and 3D cell models. Gene expression was normalized on the housekeeping gene *RPS18*. T-test (unpaired, two tailed): * $p \leq 0{,}05$; *** $p \leq 0.001$. **.** Western blotting analysis for myogenesis regulators in total protein fraction. of myogenesis-regulators protein *MyoD (B), Myog (C)* for 2D and 3D cell model expression levels normalized on β-actin. T-test (unpaired, two tailed): ** $p \leq 0{,}01$;

TNPO3 expression in LGMDD2

Real-time PCR in 2D cultures showed an increased expression of TNPO3 at the early stages of differentiation, peaking at T1-T5 in CTRL, while remaining high until T10 in LGMDD2 cells. In

3D cultures, the upregulation was mitigated, with constant expression in CTRL and a slight increase over time in LGMDD2. A more detailed analysis was done by examining TNPO3-CT and TNPO3-NT at the transcriptional level. The N-terminal domain generally binds RanGTP, and the C-terminal domain carries the cargoes. Analysis showed no significant difference between the conditions. Among the LGMDD2-related proteins, the expression of Serine and Arginine Rich Splicing Factor 1 (SRSF1) was also evaluated. SRSF1 is a TNPO3 cargo and displayed a slight increasing trend in CTRL during differentiation. LGMDD2 showed an inverse expression, with a decrease throughout differentiation. The 3D model revealed similar expressions in both conditions, with a slight increase in LGMDD2, reflecting the TNPO3 trend and suggesting their joint activity (Fig. 2B). RNA binding motif protein 4 (RBM4), cargo of TNPO3, is involved in alternative splicing events and selection of muscle cell-specific exons. RBM4 showed a similar trend of 2D and 3D TNPO3 levels, confirming their connection. RBM4 contributes to Polypyrimidine tract binding protein (PTB) reduction. The data obtained show upregulation of PTB in times T0 and T1 in LGMDD2 and a significant downregulation at T5. On the other hand, the relative expression in 3D reveals a steady level in CTRL and increased expression in LGMDD2.

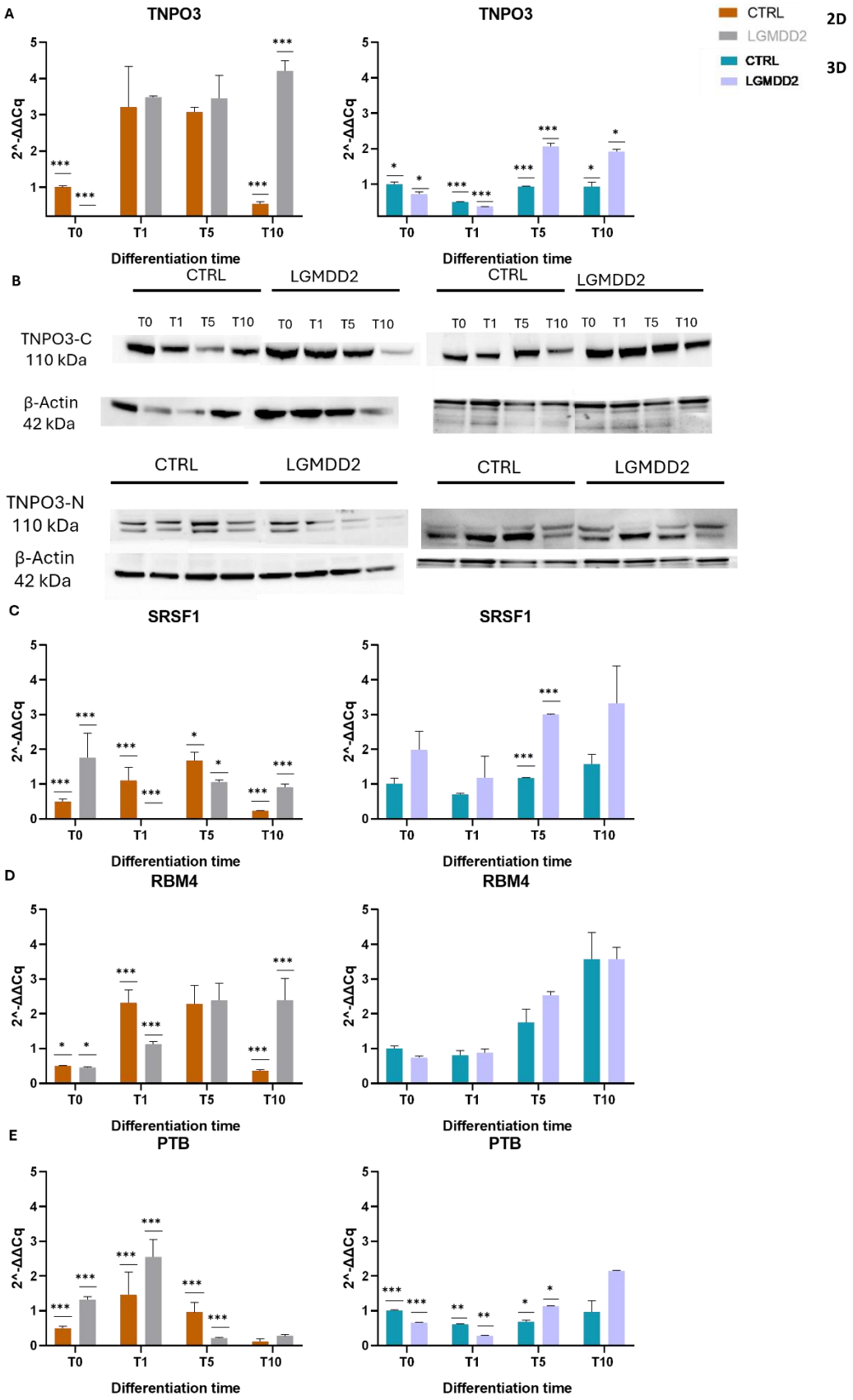

Figure 2. Graphic representation of LGMDD2 related genes, relative gene expression (TNPO3, SRSF1, RBM4 and PTB) levels evaluated by Real Time q-PCR at T0-T1 (early stages), T5 (intermediate stage) and T10 (late stage) of myogenic differentiation in both 2D and 3D cell models.

Gene expression was normalized on the housekeeping gene RPS18. T-test (unpaired, two tailed): * p ≤ *0,05; *** p ≤ 0.001.* **.** *LGMDD2-related protein TNPO3 C-t, TNPO3 N-t, expression levels both in 2D and 3D cell models, normalized on β-actin; Western blotting analysis on total protein fraction.*

Role of TNPO3 and its cargoes

Immunofluorescence assays were carried out on CTRL and LGMDD2-derived myoblasts according to the distinct differentiation stages with the aim of establishing the influence of myogenic differentiation in TNPO3 and SRSF1. Specifically, TNPO3 expression levels and localization have been confronted with its cargo protein and splicing factor SRSF1. In undifferentiated healthy myoblasts (T0) TNPO3 is exclusively expressed at cytoplasmic level, while SRSF1 has both a nuclear and cytoplasmic presence. For what concerns LGMDD2-derived myoblasts, TNPO3 signal is uniformly distributed in the cytoplasmic compartment; on the contrary, SRSF1 expression is only nuclear. At T1, in control myoblasts TNPO3 signal seems to be similarly distributed within the nuclear and cytoplasmic compartments; SRSF1, instead, looks more clustered at nuclear level, but present, to a lesser extent, in the cytoplasm. However, in pathologic cells, their localization is opposite: TNPO3 expression is decreased, and it is mainly found at cytoplasmic level; SRSF1 is only localized and strongly increased into the nucleus, highlighting a significant delocalization between them. In fusing control myotubes (T5) both SRSF1 and TNPO3 signal and localization significantly increase only in the nuclear compartment, confirming colocalization. At the same time, patient-derived differentiating myoblasts exhibit a totally different condition: TNPO3 localization is only cytoplasmic; conversely, SRSF1 expression increases, and it's found only into the nucleus.

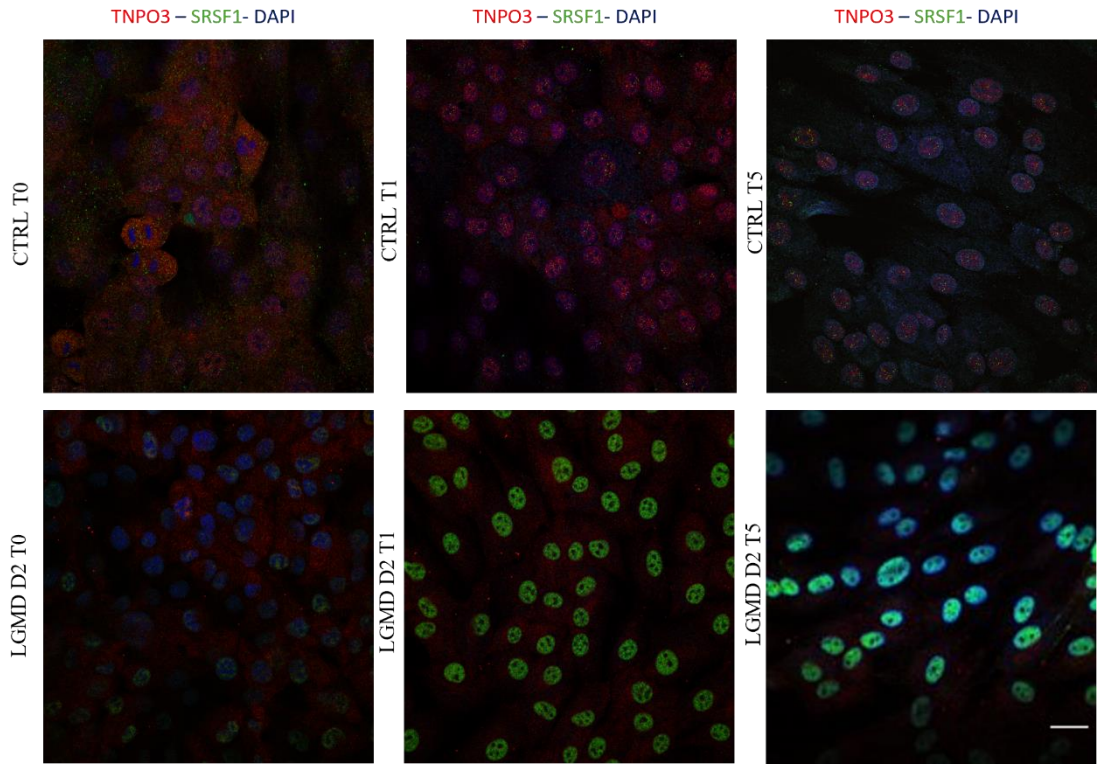

Figure 3. Investigation of TNPO3 C-t and SRSF1 localization during myogenesis by confocal microscopy. IF double staining for TNPO3 (in red) and SRSF1 (in green). Nuclei are counterstained with Hoechst. Scale bar: 50µm.

Study muscular atrophy and autophagy

The study of gene expression was also conducted on Murf-1, a marker of muscle atrophy. In 2D, Murf-1 increased only in CTRL during differentiation, indicating a natural and progressive slowdown of the cell cycle. In patients, however, levels are high from time T0, almost 10-fold, and are kept constant until T10. In 3D scaffolds, both controls and patients showed low expression except at T10, where gene levels increased dramatically in LGMDD2 (Fig 3A). the P-62 protein, involved in autophagic processes, revealed downregulation of gene expression after T0-T1 in 2D LGMDD2, whereas low gene levels (10-fold) were detected from T0-T1 in CTRL. In contrast, 3D scaffolds always showed a gradual increase in both CTRL and LGMDD2, consistent with the natural increase in cell death rate. P-62 localization analyzed by immunofluorescence showed the presence of P-62 in T0 LGMDD2 cells, with cytoplasmic spots of the protein. Differentiated LGMDD2 cells presented an increased signal of P-62 (Fig 3B-C).

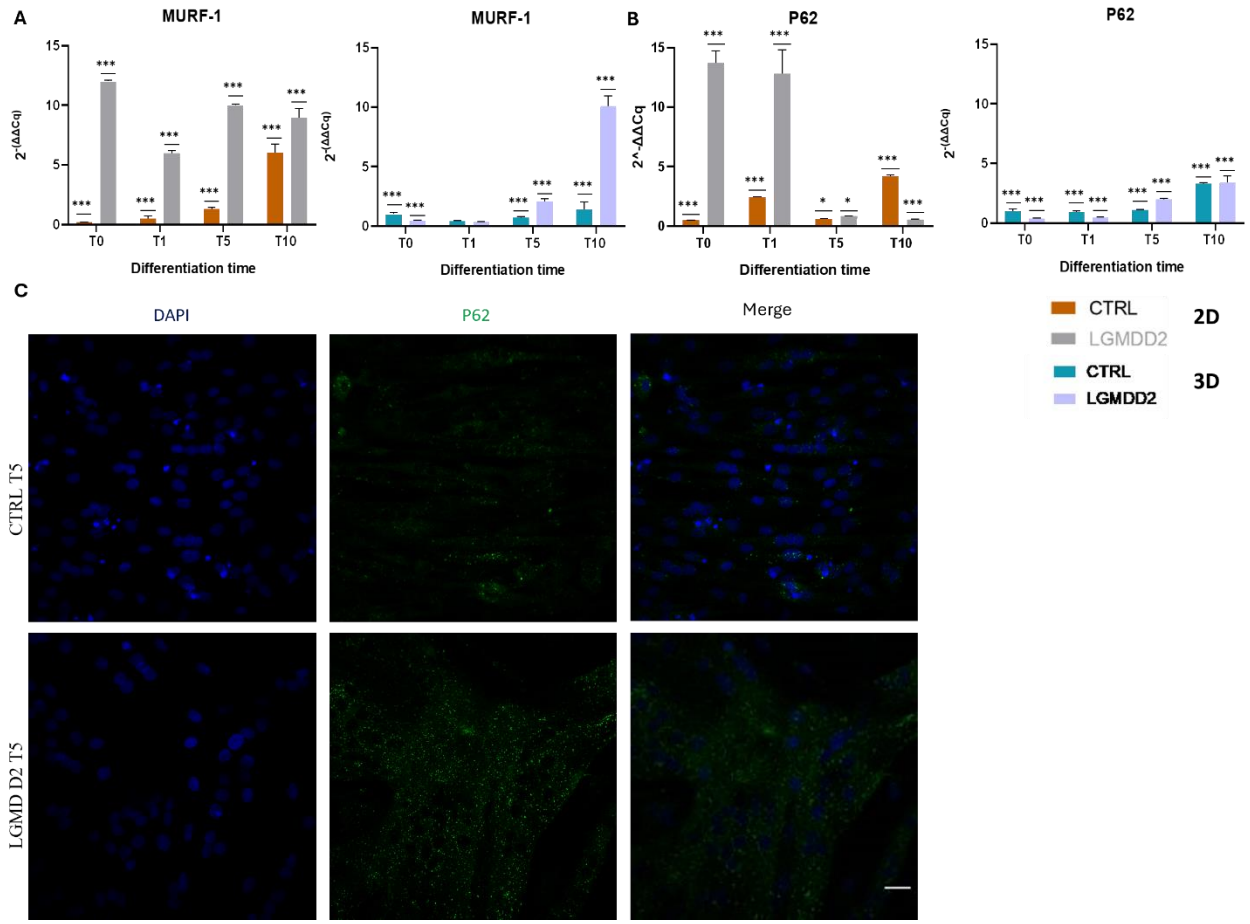

Figure 4. Graphic representation of atrophy (MURF-1) and autophagy (P62) markers relative gene expression levels evaluated by Real Time q-PCR at T0-T1 (early stages), T5 (intermediate stage) and T10 (late stage) of myogenic differentiation, in both 2D (A-B) and 3D (C-D) cell models. Gene expression was normalized on the RPS18 housekeeping gene. T-test (unpaired, two tailed): * $p \leq 0,05$; *** $p \leq 0.001$. Investigation of P62 localization during myogenesis by confocal microscopy. IF staining for P62 (in green). Nuclei are counterstained with Hoechst. Scale bar: 50µm.

Ultrastructural characterization of LGMDD2

CTRL and patient-derived myoblasts at T0 appear mononucleated, showing no structural evidence of muscle differentiation. The cytoplasm contains morphologically normal mitochondria, an amount of granular endoplasmic reticulum and electron-dense granules. Glycogen masses in packed aggregates and multi-lamellated structures can also be appreciated, particularly in healthy myoblasts. In addition, the nucleus surrounded by the nuclear membrane and condensed chromatin inside it are easily noted in both conditions and stages of differentiation; At the same time, developing myofibrils are absent in these early differentiation stages; they are considered to be synthesized after the completion of cell division, implying that cell division and myotubes differentiation are mutually exclusive events in skeletal muscle differentiation. At T5, both control

and LGMDD2-derived cells show clearly multinucleated myotubes. Moreover, at higher magnification, outlines of Z-bands surrounded by filaments are seen in the cytoplasm in both cell types, confirming that multinucleation determined by fusion of myoblasts in myotubes allows muscle differentiation. In particular, control cells at T5 show a higher amount of newly synthetized filaments, even with parallel orientation, while LGMDD2-derived myotubes show less and not yet well-oriented filaments. All the other cellular components of both healthy and pathologic cells show no relevant difference in comparison to the early differentiation stage.

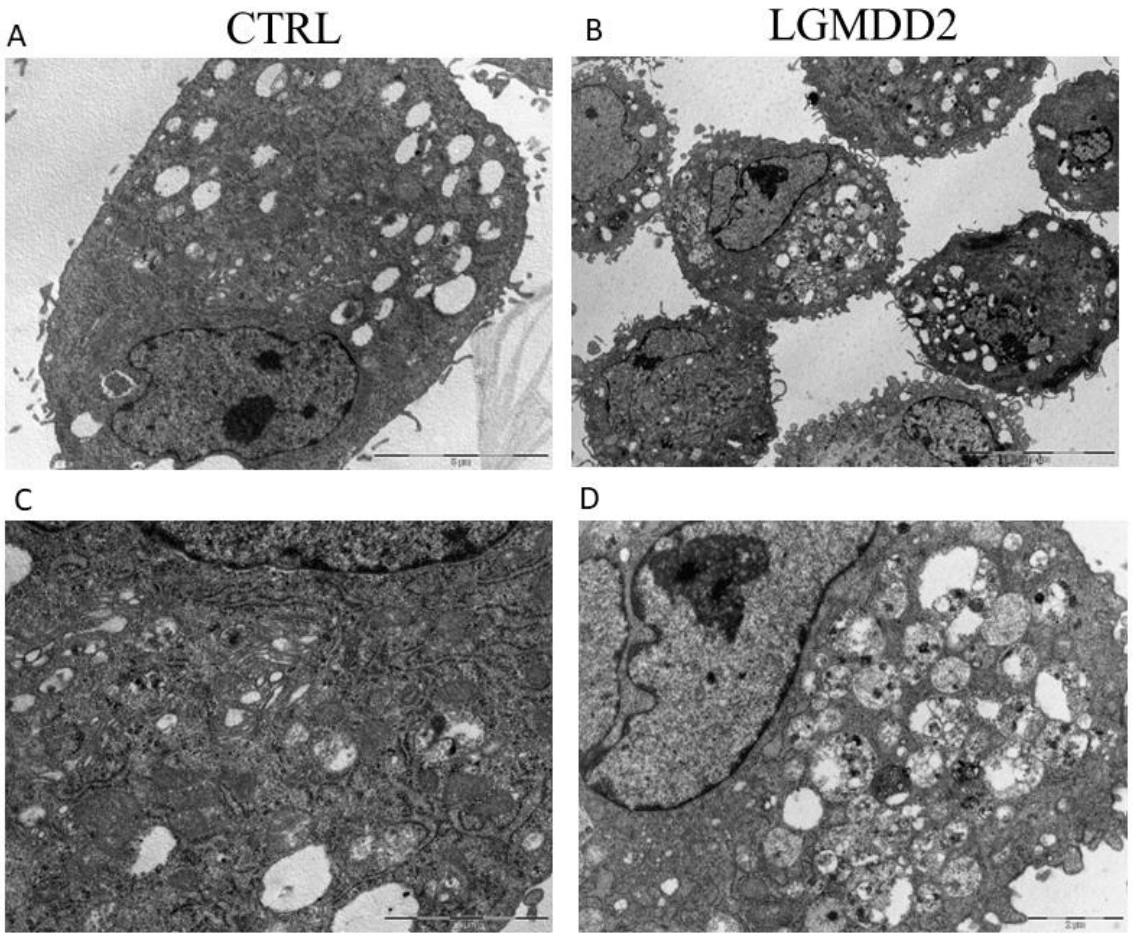

Figure 5. TEM analysis of healthy and LGMDD2-derived myoblasts in the early differentiation stage (T0). A and B images show 10 µm of magnification, whereas C and D a higher magnification of area (2 µm).

Discussion

Limb Girdle Muscular Dystrophy type D2 (LGMDD2) is a rare autosomal dominant- inherited neuromuscular disorder, dominated by progressive severe weakness occurring at the beginning in

the pelvic lower girdle and then extending to the axial and shoulder girdle, with increasing muscle atrophy (Costa et al., 2022). The mutation responsible for this condition occurs in the gene encoding for Transportin-3 (TNPO3), whose deletion of a single nucleotide causes an open reading *frameshift* and results in a 15 aminoacids protein elongation at the level of the C- terminal domain (Torella et al., 2013). Because TNPO3 protein belongs to β-karyopherins family, it facilitates the nuclear import of Ser/Arg-rich (SR) proteins. It has almost a ubiquitous expression and it plays an essential role in transcription regulation by indirectly participating in: splicing; 3' processing; mRNA transport; translation; non-sense mediated mRNA decay (Maertens et al., 2014). Hence, this protein was widely investigated; moreover, because of its related role to LGMDD2, it is fundamental to better explore its function in the muscular context, as well as taking into account the role of its cargoes. Especially, to better understand TNPO3 and its cargoes roles in myogenic differentiation, in my project, healthy (control (CTRL)) and LGMDD2 patients-derived immortalized human myoblasts were cultured by traditional cell cultures and by bio-printed scaffold, recapitulating the pathology in two and three dimensions (3D), respectively. In particular, 3D collagen scaffolds were employed since they replicate not only extracellular microenvironment of skeletal muscle but also guarantee their functionalities, overcoming the limits of traditional cultures. The setup consisted of 3D scaffolds of a bioink formulation of collagen type I mixed with myoblasts extruded by an extrusion bioprinter. The study was first of all focused on the molecular analysis of the myoblast's genetic profile; the genes chosen included 4 categories: myogenesis regulators (MRFs) (Myf5, Myf6, MyoG*)*, muscle-specific proteins (MEF2C in its isoforms α1 and α2 and desmin*)*, atrophy and autophagy markers (MURF-1, P62) and LGMDD2-related proteins (PTB, RBM4, TNPO3 and SRSF1*)*. The choice to analyze MRFs expression levels was necessary for demonstrating how myogenesis is driven, as it is an essential parameter that provides insights into both normal physiological processes and pathological conditions. Among MRFs, Myf5 is one of the first genes activated in myogenesis, so it was necessary to investigate it for its involvement in the early stages of differentiation. On the other hand, Myf6 and Myog are temporally expressed later than Myf5, directing myoblasts specification. The gene expression analysis of Myf5 and Myf6 indicated substantial differences between CTRL and LGMDD2 cells, particularly in the early and late stages of differentiation. In 2D culture, LGMDD2 myoblasts exhibited a 2- to 3-fold higher expression of Myf5 during early differentiation, with a consistent trend of higher expression than CTRL even as differentiation progressed. However, in the 3D scaffold, Myf5 expression showed a progressive increase, peaking at a 4-fold upregulation in LGMDD2 cells at late stages (T10), suggesting that the 3D environment supports a prolonged myogenic commitment. Similar behavior was observed for Myf6, Myf6 is expressed during myogenic specification, after MyoG activity stops Myf5

expression, where LGMDD2 cells maintained statistically higher expression throughout differentiation in 2D whereas in 3D cultures higher levels were only at the late stages. The data indicated that LGMDD2 presents irregularities during myogenic commitment: In 2D culture, LGMDD2 cells exhibited early stimulation to differentiate with high Myf5 expression, but with an active signal throughout the process; In 3D, Myf5 was under-expressed in the early stages of differentiation and upregulated in the later stages in LGMDD2. Conversely, control cells displayed an opposite pattern, where Myf5 typically manifests during early development. Therefore, the late upregulation of Myf5 in 3D LGMDD2 could be explained as a prolonged attempt to differentiate, reflecting sustained proliferation compared to control. Similarly, Myf6 expression provides additional evidence of dysregulated differentiation in LGMDD2 cells cultured. In 2D the elevated early-stage expression of MRFs suggests a precocious initiation of the maturation process; however, the prolonged and abnormally sustained Myf6 activity indicates a failure to achieve proper terminal differentiation. By contrast, 3D was characterized by a progressive increase in Myf6 amount for both conditions (CTRL and LGMDD2), suggesting how the bioprinting technique mimics the tissue-like environment influencing myogenic factors expression. Additionally, the transcriptional expression of MyoD, typically active during early differentiation, demonstrated a dysregulated pattern in the 2D model and an overexpression at T10 in the scaffold, further confirming its abnormal regulation. MyoG, a key regulator of terminal differentiation, was markedly upregulated at both transcriptional and protein levels in LGMDD2 myoblasts, with up to an 8-fold increase from T1 to T10 compared to CTRL. The sustained upregulation observed in both 2D and 3D cultures highlights the heightened differentiation activity in pathological cells. In 2D, following the Myf5 and Myf6 stimuli, MyoG peaked at T1, indicating early myogenic differentiation. However, in 3D cultures, MyoG increased progressively, showing its expression even at T0, following the gradual rise of Myf5 and Myf6. MyoG expression at T0 in the 3D model might be related to the influence of the 3D matrix, which itself induces cell maturation. In 2D the muscle-specific and structural gene Desmin, also followed a similar trend with a 3- to 4-fold upregulation in LGMDD2 at an early stage, indicating a strong structural and functional commitment to differentiation. In 3D, the trend was progressive and consistent with the previous stimuli, confirming their ability to modulate differentiation without altering protein structure. Myocyte Enhancer Factor 2C (MEF2C) has been investigated because of its regulatory function during the myogenic process. Its two isoforms α1 and α2, exhibit an opposite role: the former recruits HDAC5 histone deacetylase by hindering muscle-specific gene expression; the latter promotes muscle differentiation (Zhang et al., 2015). The MEF2Cα1/α2 ratio exhibited a >1 ratio in early stages in CTRL, which gradually decreased, suggesting inhibition of differentiation. Conversely, in LGMDD2 cells, the ratio was <1, indicating

delayed but ultimately enhanced myogenic differentiation at late stages. Data suggest that the underlying cause of LGMDD2 onset may involve disruptions in myogenesis regulatory pathways rather than muscle-specific protein expression. The hypothesis is supported by recent studies demonstrating the involvement of the TNPO3 protein and its cargoes in myogenic differentiation processes (Costa R. et al., 2021). Regarding TNPO3 and its cargoes, the expression analysis showed an increase in both CTRL and LGMDD2, with LGMDD2 exhibiting a prolonged upregulation of TNPO3 at the later stages. The transcriptional evaluation of TNPO3-CT and TNPO3-NT domains revealed no significant difference between conditions, but a more detailed examination of cargo proteins such as SRSF1 and RBM4 revealed differential expression patterns. Following TNPO3, in 2D cultures, SRSF1 showed an increasing trend at T0 and T10 in LGMDD2, while the 3D model displayed a slight increase in both CTRL and LGMDD2 conditions, with elevated levels in LGMDD2 at the late stages. Furthermore, among TNPO3 cargoes also RBM4 activity deserves to be highlighted, altogether with PTB expression. RBM4 and PTB are both implicated in alternative splicing events and muscle-specific exons selection, demonstrating an opposite trend during myogenic differentiation, as it was shown for C2C12 murine cell line (J. C. Lin & Tarn, 2011). RBM4 followed the TNPO3 expression pattern, further confirming, along with SRSF1, their role in splicing regulation and the potential connection between TNPO3 and muscle cell-specific exon selection. In addition, results obtained by immunofluorescence assays, performed to evaluate TNPO3 and *SRSF1* expression and localization are consistent with previous studies (Costa R. et al., 2021). They confirm in CTRL a similar distribution between nucleus and cytoplasm for TNPO3 in the early differentiation stages, and a progressive increase into the nuclear compartment as differentiation proceeds. SRSF1 localization is mainly nuclear from the beginning, and its signal, highly clustered, steadily increases, showing an evident colocalization with *TNPO3* in the late differentiation stages. In the case of LGMDD2-derived myoblasts fluorescent intensity is surprisingly expressed in different compartments by TNPO3 and SRSF1: the former appears localized only into the cytoplasm from T0, and slightly increasing in the nucleus at T1, but still persisting into the cytoplasmic compartment in the advanced stages of differentiation; the latter has a prominent expression only into the nucleus throughout the differentiation stages, revealing an apparent delocalization between them. On the whole, confocal imaging emphasized a different localization between nuclear and cytoplasmic compartments for TNPO3 during myogenic differentiation, strongly increasing in the nucleus of differentiating myotubes, and a consistent expression only in the nuclear compartment for SRSF1.Therefore, they are colocalized only in the nucleus as the myogenesis proceeds. These data, in accordance with Costa's study suggest that, in CTRL, SRSF1 and TNPO3 interaction and TNPO3 localization variations follow the myogenic

differentiation, again implying how this process could have a role in the proteomic network regulation into which myotube formation is involved and, in turn, affect LGMDD2 pathogenesis. Actually, this evidence is strengthened by opposite results obtained for LGMDD2-derived myoblasts: an evident delocalization between TNPO3 and SRSF1 is observed in the whole myogenic process as previously stated, suggesting that different localization and, consequently, the lack of interaction between them, which must be further elucidated, has surely a function in the pathogenetic course. The differential distribution of TNPO3 and its cargo proteins in CTRL and pathological cells points to altered splicing regulation in LGMDD2 conditions, potentially contributing to the muscle degeneration phenotype. Gene expression study was also performed on MURF-*1*, an atrophy marker related to the slowdown of the cell cycle and present in the advanced differentiation state. MURF-1 controls the half-life of important muscle proteins, including heavy and light chain myosin (Bodine & Baehr, 2014). Studies have demonstrated that all the MURFs proteins are tightly regulated during development, but MURF-1 is the only family member associated with muscle atrophy and, when abolished, results in muscle loss attenuation. Since LGMDD2 is associated with pronounced muscle atrophy, our findings support this, as MURF-1 was upregulated only in CTRL during differentiation in 2D, reflecting the natural slowdown of the cell cycle as differentiation progresses. In LGMDD2, MURF-1 remained consistently high, indicating impaired regulation of muscle turnover. In 3D cultures, MURF-1 was upregulated in both CTRL and LGMDD2, in line with myogenic commitment, but peaked at T10 in LGMDD2, suggesting an increased cell death rate. This outcome could be attributed to the enhanced *in vitro* conditions in 3D scaffold, which preserve cell vitality due to their spatial depth and improved cell-cell and cell-matrix interactions. In contrast, traditional 2D culture, with restrictive proliferation conditions, results in a higher death rate, as seen in daily culturing. P62 protein, a multifunctional scaffolding protein associated with selective autophagy (Jeong et al., 2019), was also evaluated. In 2D, P62 levels were 10 times higher in LGMDD2 at T0 and T1, while in 3D, both CTRL and LGMDD2 exhibited a gradual increase in P62 expression, correlating with the rising cell death rate in differentiated myotubes. Immunofluorescence analysis confirmed these findings, with LGMDD2 cells showing cytoplasmic accumulation of P62. This increased presence was also observed in patient biopsies from previous studies (Cenacchi G. et al., 2013), validating the theory that autophagic pathways are heightened in pathological conditions. Transmission electron microscopy (TEM) further corroborated our findings by revealing clear differences in myotube formation between control and LGMDD2 cells. at T5, Z-bands outlines and filaments well-oriented for control myoblasts and undirected for patient-derived myoblasts correlate with α-actinin IF expression and localization, that spreads along the entire myotube length. This confirms, as a cytoskeletal protein,

its contribution to Z-disk formation, and its necessary role to establish cell preservation from mechanical stress and controlling cell movement. Its similar expression in both normal and pathological myoblasts, as a muscle-specific protein, could further remark the major role that myogenic differentiation and its related factors have in LGMDD2 pathogenesis.

In conclusion, the results obtained so far are very promising, not only because they align with previous studies but also because significant differences have been detected between healthy and patient-derived myoblasts, which warrant further investigation. The main purpose of this work was to deepen the understanding of the pathogenetic mechanism of LGMDD2, caused by the TNPO3 mutation, with a particular focus on myogenic differentiation by evaluating both the expression of MRFs and specific muscle proteins. Myogenic differentiation appears to play a key role in the disease's onset, as cells from patients predominantly exhibit dysregulation of myogenic factors, suggesting that interactions between these factors and pathology-related proteins could trigger LGMDD2 itself. Moreover, the use of a 3D model proves to be successful, not only because it replicates the pathology in a 3D environment that faithfully mimics the *in vivo* skeletal muscle system and surpasses the limitations of 2D cultures, but also because 3D scaffolds could potentially provide an alternative to animal models in the future. The adaptability and reproducibility of this system make it a valuable tool for *in vitro* modeling, not just to explore pathogenetic pathways but also to test new drugs, facilitating the development of personalized medicine approaches and reducing the need for preclinical animal testing, thus accelerating the transition to clinical trials.

Taken together, our results highlight the distinct myogenic behaviors of LGMDD2 in both 2D and 3D systems, characterized by an early stimulus to differentiate in 2D, altered differentiation in 3D, abnormal splicing factor localization, and impaired structural development. The upregulation of myogenic markers at later stages, combined with persistent dysregulation of muscle-specific proteins and splicing factors, suggests that LGMDD2 myoblasts attempt to compensate for the impaired differentiation process, although the overall structural and functional outcomes remain compromised. These findings provide crucial insights into the molecular mechanisms underlying LGMDD2 pathogenesis and underscore potential targets for therapeutic intervention.

2.2. Development of a Micro-Pillar System for Culturing Functional Human Skeletal Muscle Microtissues: Insights into LGMDD2 Pathophysiology

Introduction

Although significant progress has been made toward predictive *in vitro* models for liver, lung, and cardiac tissues, functional models for skeletal muscle have lagged behind, hindering drug development for numerous disorders affecting muscles and movement. The development of human *in vitro* systems for basic biological studies and drug discovery is driven by the need to improve patient outcomes while reducing the ethical concerns associated with animal testing. Though animal models have advanced our understanding of disease mechanisms, they often fail to predict human drug responses due to species-specific differences (McGreevy J. et al., 2015, DiMasi J. A. et al., 2003). This issue was highlighted by the market withdrawal of the cholesterol-lowering drug cerivastatin, which caused fatal rhabdomyolysis in humans despite being well-tolerated in mice (Furberg CD. et al., 2001). Furthermore, skeletal muscle plays a central role in diseases such as diabetes, obesity, and various dystrophies, and influences organ-organ interactions, including cognition, inflammation, cancer, and aging, through the secretion of contraction-dependent myokines, thus, it is crucial to develop accurate human skeletal muscle models for drug testing and disease research (Balakrishnan R, Thurmond D. C. 2022, Isaac R. et al., 2021). While efforts to develop 2D culture systems for human myoblasts have been well-established, these models face limitations. They struggle to maintain long-term structural integrity (Eberli D. et al., 2009, Smith, A. S. T. *et al*., 2014), lack the architecture of native muscle, and require complex media components to initiate contractions (Falcone, S. *et al*., 2014). Additionally, although the contractile force of single *in vitro* cultured human myofibers can be measured, these systems are limited in their ability to investigate biochemical changes or cell-matrix interactions, which are crucial in pathologies such as muscular dystrophies and muscle wasting disorders (Guo, X. *et al*., 2014). Three-dimensional (3D) culture models have been developed to address some of these challenges (Vandenburgh, H. *et al*., 2008, 2009, Maffioletti, S. M. *et al*., 2018, Takahashi H. et al., 2018)). In rodent models, 3D skeletal muscle cultures have demonstrated measurable contractile force and have been applied to drug testing and disease modeling (Afshar Bakooshli, M. *et al*., 2019). Madden L et al, 2015 successfully bioengineered muscle bundles using cells from human biopsies, which were grown on polymer frames in the laboratory. The bioengineered muscle tissues responded to electrical and chemical signals and exhibited contractile behaviors similar to those of normal muscle, closely mimicking the structure and signaling properties of healthy muscle in humans. Building on these innovations, we have developed a novel 3D human skeletal muscle

device with a micro-pillar system for functional analysis on LGMDD2. Our approach allows for the bulk production of human muscle microtissues using a simple, reproducible casting process that integrates easily into standard workflows and requires fewer cells. Immortalized human myoblasts, including both healthy and LGMDD2 cells, self-organize into multi-nucleated, striated myotubes that respond to electrical and biochemical stimuli with kinetics and maturation levels similar to those observed in larger formats. Importantly, our micro-pillar system enables non-invasive, in situ measurement of contractile force over time, allowing for longitudinal studies that were previously not feasible. This advancement fills a critical gap in the development of functional human skeletal muscle models, supporting not only fundamental research but also drug discovery and toxicity studies, with the potential to significantly improve therapeutic outcomes.

Materials and Methods

Micropillar fabrication and applications

The micropillar system was a custom-designed elastomeric insert for a 12-well plate, where each well consists of an elliptical inner chamber with two vertical posts at either end, acting as tendon-like anchor points to establish uniaxial tension and direct micro-tissue formation and compaction in remodeling SKM. 3D SKM were obtained using immortalized human myoblast CTRL and LGMDD2 suspended in a hydrogel mix (patent). The cell-hydrogel suspension was pipetted into the well chambers, surrounding the posts. 3D myoblasts were fixed, labeled, and imaged with confocal microscopy following our previous protocol. Z-stack images were captured, and myotube diameters were quantified using NIH ImageJ. Samples were collected, lysed in RIPA buffer with protease inhibitors, and total protein concentration was measured using a BCA assay kit, following previous protocol. Western blot analysis was performed on 20-25 µg of protein run on a 4-12% SDS-PAGE gel, as previously described.

Electrical stimulation of micro-pillar system

Two electrodes were sterilized and inserted behind the posts in each well to generate an electric field parallel to the myotubes. 3D SKM were stimulated with square pulses at a 20% duty cycle, 5 V amplitude, and frequencies of 0.5 Hz and 10 Hz for twitch and tetanus contractions. Post deflection movies were recorded using an iPhone SE at 10X magnification and analyzed using

Python script to determine post displacement in pixels indicating the tension generated by contracting SKM.

Results

Evaluating skeletal muscle development in 3D micro-pillar system

We report a novel *in vitro* platform, referred to as the micro-pillar system, which facilitates the reproducible culture of contractile human skeletal muscle microtissues (hSKMTs) using CTRL and LGMDD2 immortalized human myoblasts to investigate muscle physiology and functionality. The micro-pillar system consists of a custom-designed elastomeric 12-well plate where each well contains an elliptical chamber with two vertical posts at either end. The plates are fabricated using a multi-step casting process based on a 3D-printed design, resulting in a reusable polyurethane (PU) negative mold for the generation of plates containing up to 12 wells. This process allows for single-step polydimethylsiloxane (PDMS) casting within three hours (Figure 1A). Three-dimensional (3D) hSKMTs were engineered by suspending purified human myoblast cells (Figure 1B) in a hydrogel mixture (patent) and pipetting the cell-hydrogel suspension into the micro-pillar system wells, filling the area around the posts. The posts act as tendon-like anchors, creating uniaxial tension in the remodeling hSKMTs and guiding microtissue formation and compaction. A hook at the top of each post ensures that hSKMTs remain anchored during cell migration, as cells seeded on hook-less posts detach within two days. The bottom of the slanted tips of the micro-posts determines the position of the hSKMTs post-remodeling. Within seven days in differentiation media, hSKMTs consistently migrated to the area below the slanted tip and remained stable for an additional week. The micro-pillar system was optimized for bulk production of hSKMT arrays, facilitating in-dish functional analyses. Remodeling of the 3D hSKMTs began within two days in myogenic growth media and continued through the subsequent week in differentiation media. By Day 10, myoblasts had formed aligned, multi-nucleated myotubes, as confirmed by a-actinin and phalloidin immunofluorescence. By Day 7 of differentiation, the majority of cells were post-mitotic and cross-striated myotubes had formed. However, LGMDD2 showed abnormal fiber structure, cluster of a-actinin and less striation. (Figure 1C-D).

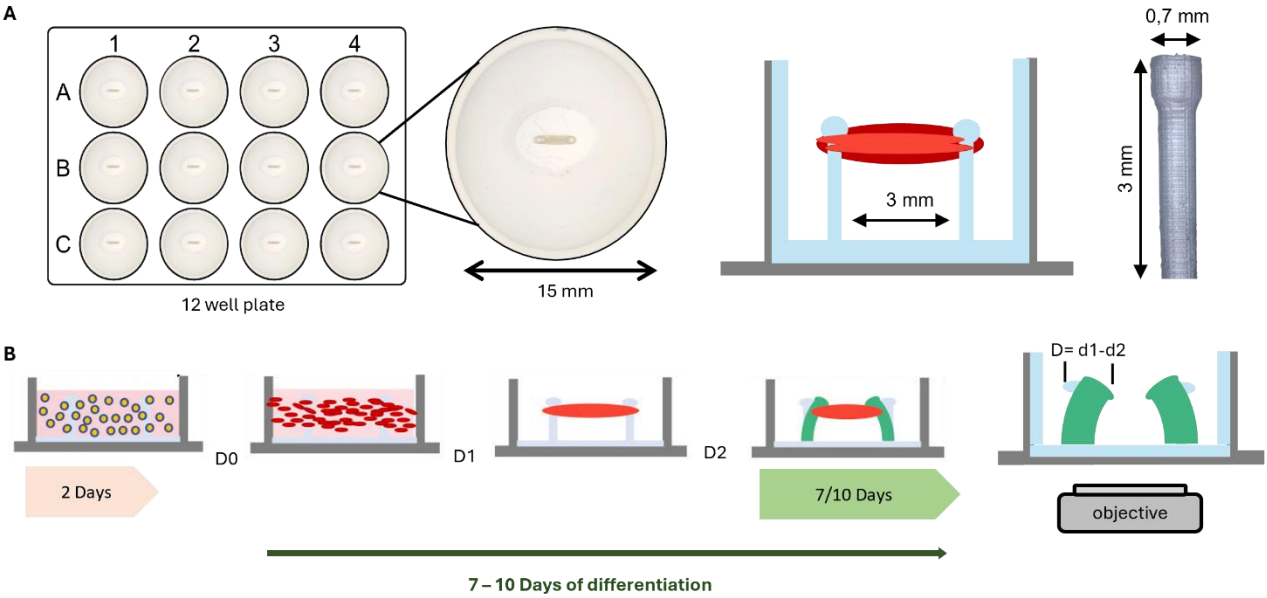
A
1
2
3
4
A
B
C
12 well plate
15 mm
3 mm
0,7 mm
3 mm
B
D0
D1
D2
2 Days
7/10 Days
D= d1-d2
objective
7 – 10 Days of differentiation

C

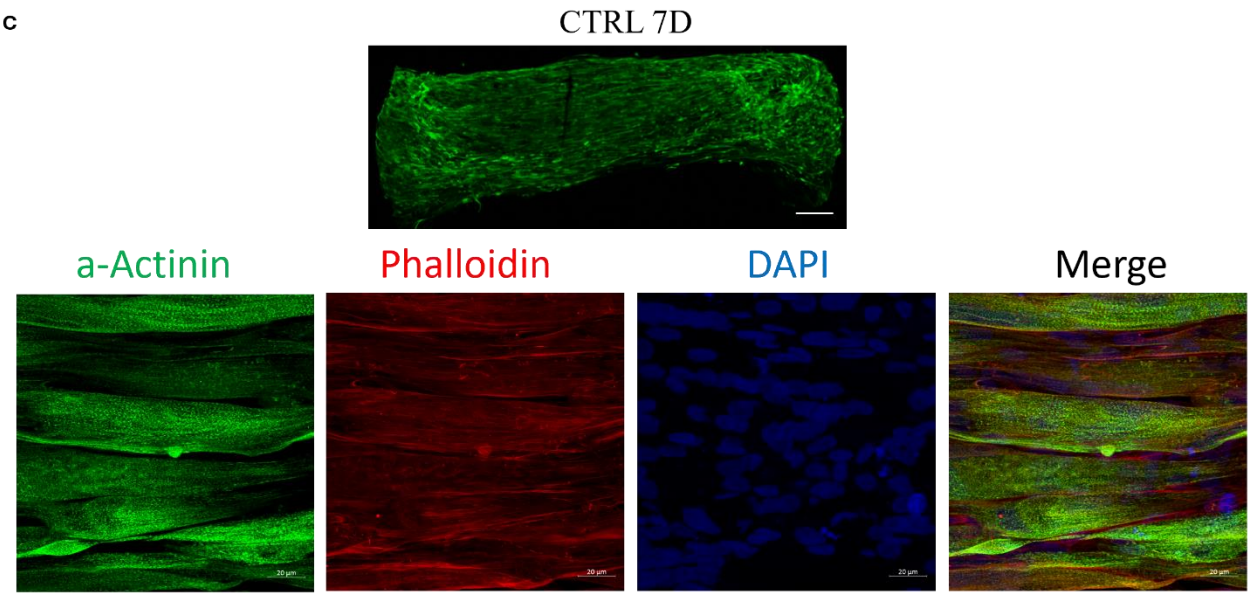
CTRL 7D
a-Actinin
Phalloidin
DAPI
Merge

D

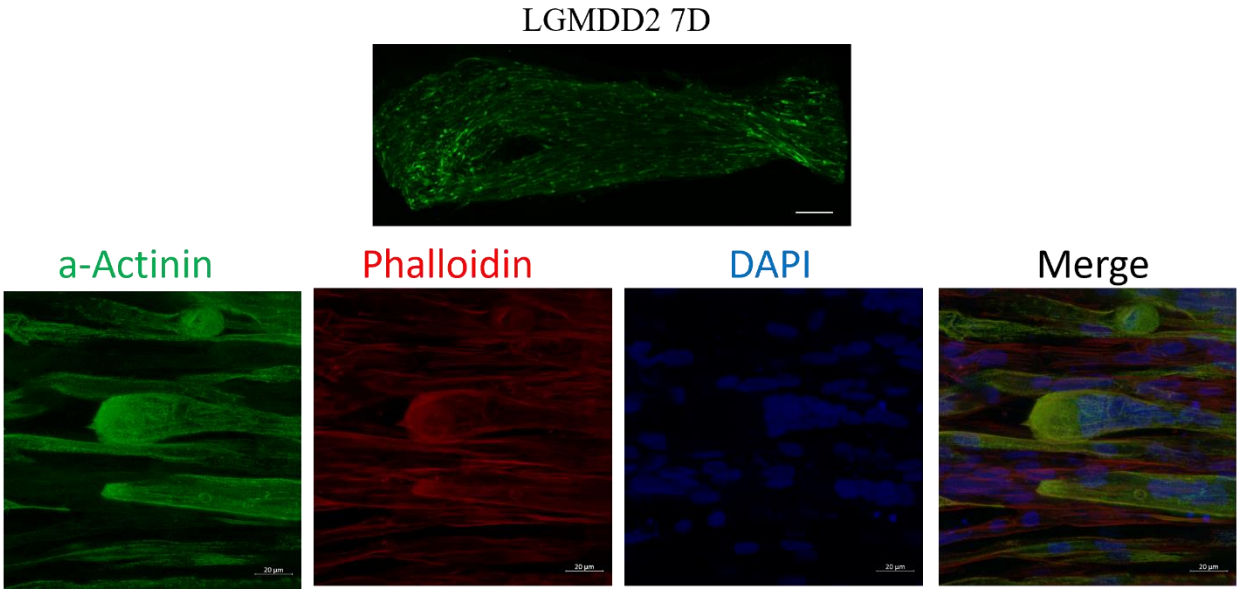
LGMDD2 7D
a-Actinin
Phalloidin
DAPI
Merge

Figure 1. Diagram representation of micro-pillar system (A). Diagram representation of hSKMTs development with 3D micro-pillar system (B). hSKMTs CTRL after 7 days of differentiation, wide image (magnification 5x, scale bar = 100 µm), Investigation of a-actinin and phallodin by confocal microscopy. IF double staining for a-actnin (in green) and phalloidin (in red). Nuclei are counterstained with Hoechst. Scale bar: 20µm. *(C).* hSKMTs LGMDD2 after 7 days of differentiation, wide image (magnification 5x, scale bar = 100 µm), Investigation of a-actinin and phallodin by confocal microscopy. IF double staining for a-actnin (in green) and phalloidin (in red). Nuclei are counterstained with Hoechst. Scale bar: 20µm. *(D).*

Myotube width was stable between Days 7 and 10, and structural maturation was indicated by the higher expression of peripheral nuclei in CTRL compared to LGMDD2 (Fig. 2A). Moreover, MYHC isoforms, including embryonic and neonatal (3;8), slow (7), and adult forms (1;2), were upregulated in LGMDD2 at both time points, with MYHC protein levels remaining elevated (Fig. 2B-C). However, markers of atrophy and autophagy were also elevated in LGMDD2 (Fig. 2D), indicating a distinct pathophysiological response.

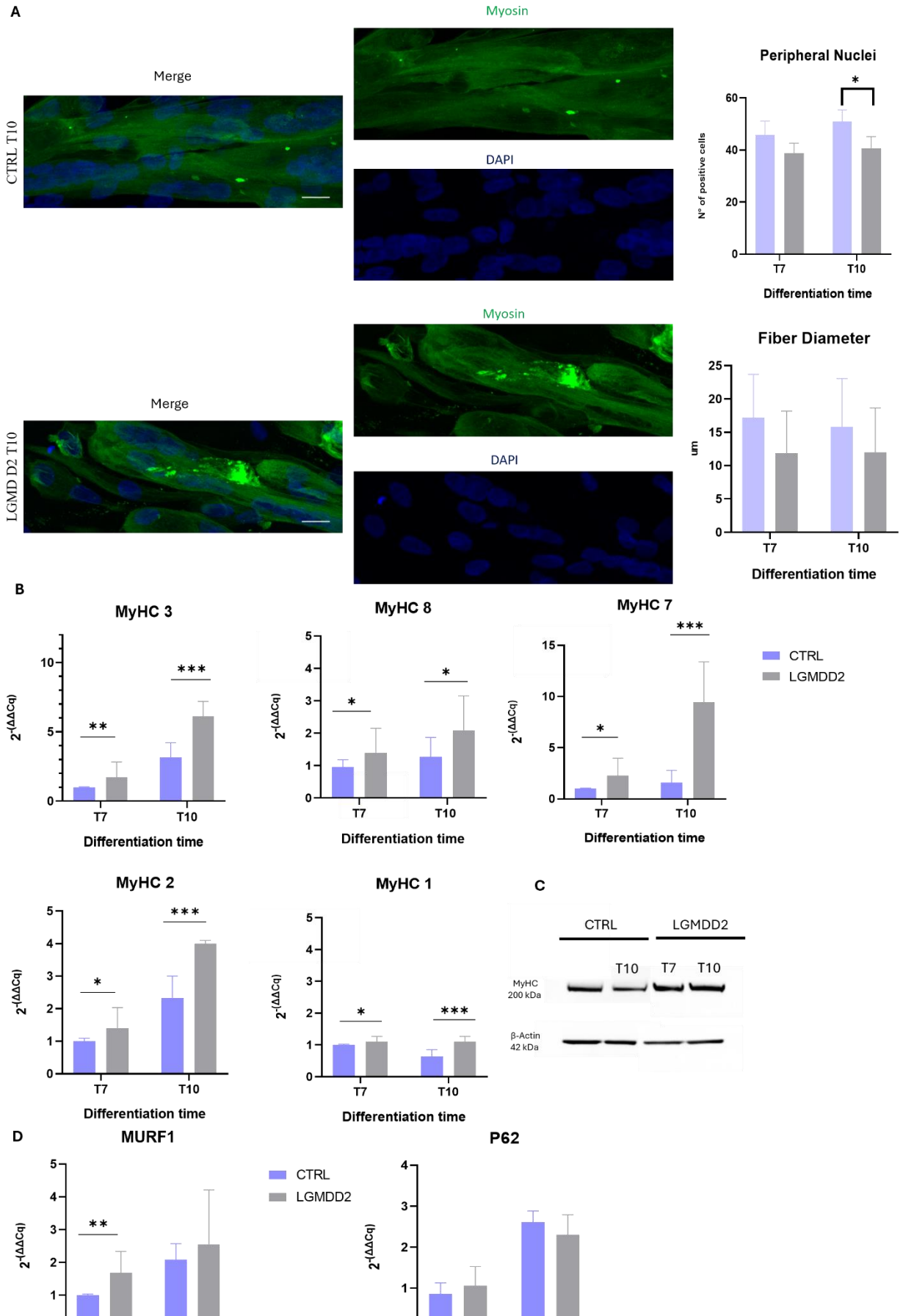
A
Myosin
Merge
CTRL T10
DAPI
Peripheral Nuclei
N° of positive cells
Differentiation time
Myosin
Merge
LGMD D2 T10
DAPI
Fiber Diameter
um
Differentiation time
B
MyHC 3
MyHC 8
MyHC 7
CTRL
LGMDD2
MyHC 2
MyHC 1
C
CTRL
LGMDD2
MyHC 200 kDa
β-Actin 42 kDa
D
MURF1
P62
CTRL
LGMDD2

Figure 2. hSKMTs CTRL and LGMDD2 after 10 days of differentiation, investigation of myosin heavy chain (green) by confocal microscopy. Nuclei are counterstained with Hoechst. Scale bar: 20µm. Graphic representation of peripheral nuclei and fiber diameter *(A)*. Graphic representation of myosin heavy chain isoforms (MyHC 3, 8, 7, 2, 1), relative gene expression levels evaluated by Real Time q-PCR at T7-T10 (late stage) of myogenic differentiation (B). Gene expression was normalized on the RPS18 housekeeping gene. T-test (unpaired, two tailed): * $p \leq 0,05$; *** $p \leq 0.001$. Western blotting analysis for MyHC in total protein fraction. Expression levels normalized on β-actin (C). Graphic representation of atrophy (MURF1) and autophagy (P62) markers, relative gene expression levels evaluated by Real Time q-PCR at T7-T10 (late stage). Scale bar = 20 µm

Contractile force generation of hSKMT with CTRL and LGMDD2 myoblast cells

The amplitude of induced contractile force by electrical or chemical stimulation is a key parameter used to evaluate skeletal muscle function both *in vivo* and *ex vivo* on isolated muscle fibers (Fuglevand et al., 1999; Bottinelli and Reggiani, 2000).Our material property enables the measurement of hSKMT contractile force by assessing the degree of post deflection caused by hSKMT contraction in response to electrical and biochemical stimuli. The mechanical modulus of the micro-post design can be fine-tuned by adjusting the PDMS monomer-to-curing agent ratio, allowing for the customization of post deflection properties. We also developed a Python-based post-tracking script to non-invasively quantify hSKMT strength through video analysis of post deflection. The semi-automated, unbiased tracking method confirmed that the absolute and specific tetanus contractile forces of hSKMT were consistent with previous reports for human skeletal muscle micro physiological systems at similar time points (Madden L. et al., 2015, Mills, R. J. *et al*. 2019) Both CTRL and LGMDD2 microtissues exhibited twitch and tetanus contractions in response to electrical stimulation (Fig. 3A). Using the post-tracking script, we observed that LGMDD2 contractile forces peaked early, reached 8uN, in the stimulation and then fluctuated and decreased over time, while the contractile forces in CTRL remained stable (Fig. 3B). Notably, LGMDD2 microtissues also demonstrated spontaneous contractions, consistent with clinical observations in LGMDD2 patients (video not shown).

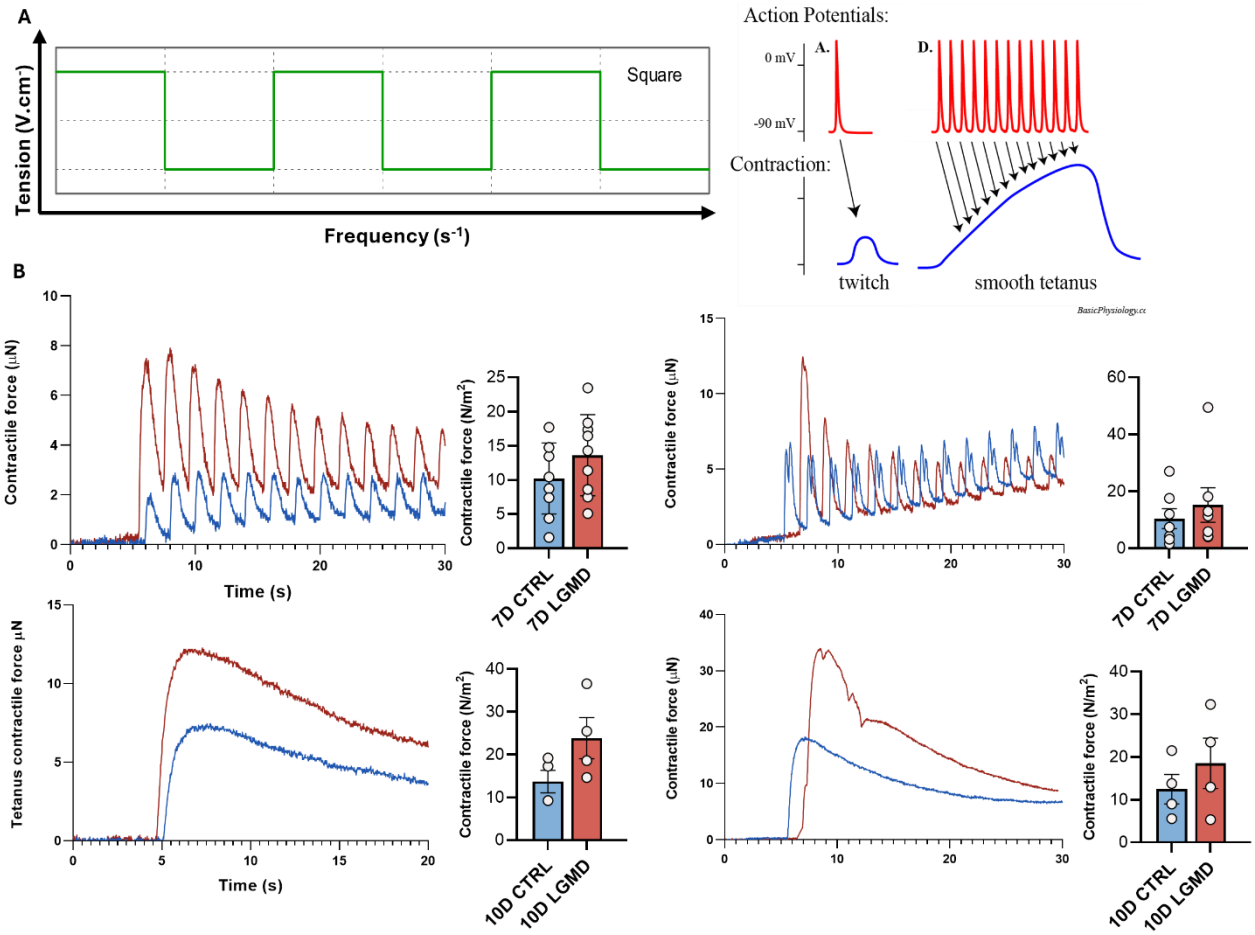

Figure 3. Non-invasive and in situ measurement of hSKMTs contractile force CTRL and LGMDD2 at 7 and 10 days (A). Upper. Representative line graph traces of the micro-post displacement during low frequency (0.5Hz) electrical stimulation of hSKMTs at Day 7, measured by the custom-written Python computer vision script. Bar graph quantification of the specific twitch contractile forces generated by hSKMTs at Day 7. Below. Representative line graph traces of the micro-post displacement during high frequency (20 Hz) electrical stimulation of hSKMTs at Day 10, measured by the custom-written Python computer vision script. Bar graph quantification of the specific tetanus contractile forces generated by hSKMTs at Day 10 (B).

Discussion

In this study, we developed and validated the micro-pillar system, a novel *in vitro* platform designed for the culture of contractile human skeletal muscle microtissues (hSKMTs). The system enables reproducible and scalable production of hSKMTs using CTRL and LGMDD2 immortalized human myoblasts, providing an essential tool for the investigation of muscle physiology and disease, as well as for drug development. The platform's innovative design, which includes an elastomeric 12-well plate with two vertical posts in each well, allows for the generation of 3D muscle microtissues that recapitulate key structural and functional properties of human skeletal

muscle. The results from our experiments show that the micro-pillar system supports the self-organization of hSKMTs, which compact and align around the posts, mimicking the architecture of native muscle tissue. Myotube formation was observed as early as day 7 of differentiation, with stable myotube width and structural maturation by day 10. CTRL tissues displayed an increased presence of peripheral nuclei, indicative of proper myotube development. This finding was corroborated by immunofluorescence analysis of α-actinin, which revealed well-organized and structurally mature myofibers in CTRL. In contrast, LGMDD2 at day 7 showed partial α-actinin striations with protein accumulation. By day 10, LGMDD2 fibers exhibited a phenotype consistent with *in vivo* pathology, characterized by cross-striations, branching, and fiber shrinkage, hallmark indicators of muscle atrophy typical of LGMDD2-affected patients. Interestingly, LGMDD2 demonstrated upregulated MYHC isoforms, with elevated levels of embryonic and neonatal forms even at late stages of maturation. Simultaneous expression of immature a mature MYHC isoforms confirmed the pathological status of the LGMDD2 model. The data obtained suggests continuous stimulation of the myogenic program, consistent with the altered myogenesis observed in our 3D bioprinting model. Additionally, LGMDD2 exhibited elevated markers of atrophy and autophagy, further reflecting the pathological characteristics of the disease and aligning with findings from our previous 3D model. Functionally, both CTRL and LGMDD2 microtissues responded to electrical stimulation with twitch and tetanus contractions. LGMDD2 microtissues generated higher overall contractile forces, driven by the upregulation of MYHC isoforms. However, the presence of immature fibers, which lack efficient contractile capacity, contributes to an imbalance in force generation, leading to the variability observed during the stimulation period. In contrast, CTRL microtissues maintained a stable and consistent contractile force, demonstrating a uniform response during the entire stimulation process. The platform's ability to track post deflection and quantify contractile forces in real time using a Python-based script presents a significant advancement in non-invasive, in situ force measurements. The mechanical properties of the posts were finely tuned by adjusting the PDMS composition, minimizing measurement errors and allowing for consistent force assessment across wells. The micro-pillar system's advantages include its rapid production process, reproducibility, and user-friendly design, which collectively make it an ideal candidate for high-throughput phenotypic screening. Moreover, the non-invasive nature of the contractile force measurements allows for longitudinal studies, enabling researchers to observe changes in muscle function over time. This capability addresses a critical limitation of existing methodologies, which often rely on endpoint assays for functional analysis. The micro-pillar system represents a significant advancement in the field of skeletal muscle research, offering a robust platform for studying muscle physiology and disease *in vitro*. Importantly, it provides a scalable solution for

phenotypic drug screening, which can accelerate the identification of therapeutic compounds for muscle disorders such as LGMDD2. Looking forward, further optimization of the micro-pillar system could enhance its utility in broader applications, such as the study of metabolic and neuromuscular diseases. Integration with advanced imaging techniques and the development of smartphone-based applications for data acquisition could further increase the system's throughput and accessibility. Additionally, by incorporating patient-derived cells, the platform could serve as a personalized medicine tool, enabling the testing of drugs tailored to individual patient profiles. Overall, the micro-pillar system holds significant promise for advancing skeletal muscle research and therapeutic development.

Acknowledgements

I would like to express my deepest gratitude to my supervisors for their invaluable guidance and support, which have been essential to the successful completion of this project.

A heartfelt thanks to the Cenacchi Group (Roberta Costa, Rodia Maria Teresa, Papa Valentina, Lomabardi Sara) at the University of Bologna for their unwavering support and trust throughout my journey; they are truly remarkable individuals.

I am also grateful to the Biomaterials and Polymer Science Research Group at the University of Bologna's Department of Chemistry "Giacomo Ciamician" for providing laboratory facilities, access to instruments, scientific expertise, and consultation, as well as assistance with scientific writing and research activities.

A special thanks to Professor Tobias Cramer (University of Bologna) for his valuable contributions to the analysis and for being a part of this project.

I would also like to acknowledge Typeone Biomaterials s.r.l. for their collaboration and for providing the collagen hydrogel essential to my research.

Lastly, I extend my sincere thanks to Professor Edoardo Malfatti (Université Paris-Est) for being a guide during my time abroad and for his enthusiastic support of my work.

References

Abasi, S.; Aggas, J.R.; Venkatesh, N.; Vallavanatt, I.G.; Guiseppi-Elie, A. Design, fabrication and testing of an electrical cell stimulation and recording apparatus (ECSARA) for cells in electroculture. *Biosensors and Bioelectronics* **2020**, *147*, 111793. https://doi.org/10.1016/J.BIOS.2019.111793.

Afshar Bakooshli, M.; Jalili, R.; Drowley, L.; Siri, L.; Khademhosseini, A.; Gilbert, P.M. A 3D culture model of innervated human skeletal muscle enables studies of the adult neuromuscular junction. *eLife* **2019**, *8*, e44530.

Afshar, M.E.; Abraha, H.Y.; Bakooshli, M.A.; Davoudi, S.; Thavandiran, N.; Tung, K.; Ahn, H.; Ginsberg, H.J.; Zandstra, P.W.; Gilbert, P.M. A 96-well culture platform enables longitudinal analyses of engineered human skeletal muscle microtissue strength. *Sci. Rep.* **2020**, *10*, 1–16. https://doi.org/10.1038/s41598-020-62837-8.

Agarwal, S.; Saha, S.; Balla, V.K.; Pal, A.; Barui, A.; Bodhak, S. Current Developments in 3D Bioprinting for Tissue and Organ Regeneration–A Review. *Front. Mech. Eng.* **2020**, *6*, 589171. https://doi.org/10.3389/fmech.2020.589171.

Aggarwal, B.B.; Danda, D.; Gupta, S.; Gehlot, P. Models for prevention and treatment of cancer: Problems vs promises. *Biochem. Pharmacol.* **2009**, *78*, 1083–1094. https://doi.org/10.1016/j.bcp.2009.05.027.

Alarcin, E.; Bal-Öztürk, A.; Avci, H.; Ghorbanpoor, H.; Dogan Guzel, F.; Akpek, A.; Yesiltas, G.; Canak-Ipek, T.; Avci-Adali, M. Current Strategies for the Regeneration of Skeletal Muscle Tissue. *Int. J. Mol. Sci.* **2021**, *22*, 5929. https://doi.org/10.3390/ijms22115929.

Alessandri, M.; Lizzo, G.; Gualandi, C.; Mangano, C.; Giuliani, A.; Focarete, M.; Calzà, L. Influence of biological matrix and artificial electrospun scaffolds on proliferation, differentiation and trophic factor synthesis of rat embryonic stem cells. *Matrix Biol.* **2014**, *33*, 68–76. https://doi.org/10.1016/j.matbio.2013.08.001.

Allen, D.G.; Lamb, G.D.; Westerblad, H. Skeletal muscle fatigue: Cellular mechanisms. *Physiol. Rev.* **2008**, *88*, 287–332. https://doi.org/10.1152/PHYSREV.00015.

Angelini, C. LGMD. Identification, description and classification. *Acta Myol.* **2020**, *39*, 207–217. https://doi.org/10.36185/2532-1900-024.

Asfour, H.A.; Allouh, M.Z.; Said, R.S. Myogenic regulatory factors: The orchestrators of myogenesis after 30 years of discovery. *Exp. Biol. Med.* **2018**, *243*, 118–128. https://doi.org/10.1177/1535370217749494.

Aubol, B.E.; Chakrabarti, S.; Ngo, J.; Shaffer, J.; Nolen, B.; Fu, X.-D.; Ghosh, G.; Adams, J.A. Processive phosphorylation of alternative splicing factor splicing factor 2. *Proc. Natl. Acad. Sci. USA* **2003**. https://doi.org/10.1073/pnas.1635129100.

Aviss, K.; Gough, J.; Downes, S. Aligned electrospun polymer fibres for skeletal muscle regeneration. *Eur. Cells Mater.* **2010**, *19*, 193–204. https://doi.org/10.22203/ecm.v019a19.

Bacáková, L.; Filová, E.; Rypácek, F.; Svorcík, V.; Starý, V. Cell adhesion on artificial materials for tissue engineering. *Physiol. Res.* **2004**, *53* (Suppl. 1), S35–S45.

Badodi, S.; Baruffaldi, F.; Ganassi, M.; Battini, R.; Molinari, S. Phosphorylation-dependent degradation of MEF2C contributes to regulate G2/M transition. *Cell Cycle* **2015**, *14*, 1517–1528. https://doi.org/10.1080/15384101.2015.1026519.

Balakrishnan, R.; Thurmond, D.C. Mechanisms by which skeletal muscle myokines ameliorate insulin resistance. *Int. J. Mol. Sci.* **2022**, *23*, 4636. https://doi.org/10.3390/ijms23094636.

Barton, E.R.; Pacak, C.A.; Stoppel, W.L.; Kang, P.B. The ties that bind: Functional clusters in limb-girdle muscular dystrophy. *Skeletal Muscle* **2020**, *10*(1). https://doi.org/10.1186/s13395-020-00240-7.

Beier, J.P.; Klumpp, D.; Rudisile, M.; Dersch, R.; Wendorff, J.H.; Bleiziffer, O.; Arkudas, A.; Polykandriotis, E.; Horch, R.E.; Kneser, U. Collagen matrices from sponge to nano: New perspectives for tissue engineering of skeletal muscle. *BMC Biotechnol.* **2009**, *9*, 34. https://doi.org/10.1186/1472-6750-9-34.

Bentzinger, C.F.; Wang, Y.X.; Rudnicki, M.A. Building muscle: Molecular regulation of myogenesis. *Cold Spring Harb. Perspect. Biol.* **2012**, *4*, a008342. https://doi.org/10.1101/cshperspect.a008342.

Berkes, C.A.; Tapscott, S.J. (2005). MyoD and the transcriptional control of myogenesis. *Semin. Cell Dev. Biol.* 16(4–5), 585–595. https://doi.org/10.1016/j.semcdb.2005.07.006

Berthiaume, F.; Maguire, T.J.; Yarmush, M.L. Tissue engineering and regenerative medicine: History, progress, and challenges. *Annu. Rev. Chem. Biomol. Eng.* **2011**, *2*, 403–430. https://doi.org/10.1146/annurev-chembioeng-061010-114257.

Biressi, S.; Filareto, A.; Rando, T.A. Stem cell therapy for muscular dystrophies. *J. Clin. Investig.* **2020**, *130*, 5652–5664. https://doi.org/10.1172/jci142031.

Blaeser, A.; Duarte Campos, D.F.; Puster, U.; Richtering, W.; Stevens, M.M.; Fischer, H. Controlling shear stress in 3D bioprinting is a key factor to balance printing resolution and stem cell integrity. *Adv. Healthc. Mater.* **2016**, *5*, 326–333. https://doi.org/10.1002/adhm.201500511.

Bloise, N.; Berardi, E.; Gualandi, C.; Zaghi, E.; Gigli, M.; Duelen, R.; Ceccarelli, G.; Cortesi, E.E.; Costamagna, D.; Bruni, G.; et al. Ether-oxygen containing electrospun microfibrous and sub-microfibrous scaffolds based on poly(butylene 1,4-cyclohexanedicarboxylate) for skeletal muscle tissue engineering. *Int. J. Mol. Sci.* **2018**, *19*, 3212. https://doi.org/10.3390/ijms19103212.

Braun, T.; Buschhausen-Denker, G.; Bober, E.; Tannich, E.; Arnold, H.H.; Buckingham, M. (1989a). A novel human muscle factor related to but distinct from MyoD1 induces myogenic conversion in 1OT1/2 fibroblasts. *EMBO J.* 8, 3.

Buckingham, M.; Rigby, P.W.J. Gene regulatory networks and transcriptional mechanisms that control myogenesis. *Dev. Cell* **2014**, *28*, 225–238. https://doi.org/10.1016/j.devcel.2013.12.020.

Cenacchi, G.; Peterle, E.; Fanin, M.; Papa, V.; Salaroli, R.; Angelini, C. Ultrastructural changes in LGMD1F. *Neuropathology* **2013**, *33*(3), 276–280. https://doi.org/10.1111/neup.12003.
Chal, J.; Pourquié, O. Making muscle: Skeletal myogenesis in vivo and in vitro. *Development* **2017**, *144*, 2104–2122. https://doi.org/10.1242/dev.151035.

Chan, E.C.; Kuo, S.-M.; Kong, A.M.; Morrison, W.A.; Dusting, G.J.; Mitchell, G.M.; Lim, S.Y.; Liu, G.-S. Three dimensional collagen scaffold promotes intrinsic vascularisation for tissue engineering applications. *PLOS ONE* **2016**, *11*, e0149799. https://doi.org/10.1371/journal.pone.0149799.

Charrasse, S.; Causeret, M.; Comunale, F.; Bonet-Kerrache, A.; Gauthier-Rouvière, C. Rho GTPases and cadherin-based cell adhesion in skeletal muscle development. *J. Muscle Res. Cell Motil.* **2003**, *24*, 309–313.

Chan, B.P.; Leong, K.W. Scaffolding in tissue engineering: General approaches and tissue-specific considerations. *Eur. Spine J.* **2008**, *17* (Suppl. 4), 467–479. https://doi.org/10.1007/s00586-008-0745-3.

Chen, F.J.; Hsiao, Y.S.; Liao, I.H.; Liu, C.T.; Wu, P.I.; Lin, C.Y.; Cheng, N.C.; Yu, J. Rational design of a highly porous electronic scaffold with concurrent enhancement in cell behaviors and differentiation under electrical stimulation. *J. Mater. Chem. B* **2021**, *9*(37), 7674–7685. https://doi.org/10.1039/D1TB01260F.

Chen, W.; Nyasha, M.R.; Koide, M.; Tsuchiya, M.; Suzuki, N.; Hagiwara, Y.; Aoki, M.; Kanzaki, M. In vitro exercise model using contractile human and mouse hybrid myotubes. *Scientific Reports* **2019**, *9*(1), 1–9. https://doi.org/10.1038/s41598-019-48316-9.

Choi, J.S.; Lee, S.J.; Christ, G.J.; Atala, A.; Yoo, J.J. The influence of electrospun aligned poly(ε-caprolactone)/collagen nanofiber meshes on the formation of self-aligned skeletal muscle myotubes. *Biomaterials* **2008**, *29*, 2899–2906. https://doi.org/10.1016/j.biomaterials.2008.03.031.

Christ, F.; Thys, W.; De Rijck, J.; Gijsbers, R.; Albanese, A.; Arosio, D.; Emiliani, S.; Rain, J.C.; Benarous, R.; Cereseto, A.; Debyser, Z. Transportin-SR2 imports HIV into the nucleus. *Curr. Biol.* **2008**, *18*, 1192–1202. https://doi.org/10.1016/j.cub.2008.07.079.

Colapicchioni, V.; Millozzi, F.; Parolini, O.; Palacios, D. Nanomedicine, a valuable tool for skeletal muscle disorders: Challenges, promises, and limitations. *WIREs Nanomedicine Nanobiotechnology* **2022**, *14*, e1777. https://doi.org/10.1002/wnan.1777.

Collinsworth, A.M.; Zhang, S.; Kraus, W.E.; Truskey, G.A. Apparent elastic modulus and hysteresis of skeletal muscle cells throughout differentiation. *Am. J. Physiol. Physiol.* **2002**, *283*, C1219–C1227. https://doi.org/10.1152/ajpcell.00502.2001.

Cook, A.; Bono, F.; Jinek, M.; Conti, E. Structural biology of nucleocytoplasmic transport. *Annu. Rev. Biochem.* **2007**, *76*, 647–671. https://doi.org/10.1146/annurev.biochem.76.052705.161529.

Corbu, A.; Scaramozza, A.; Badiali-DeGiorgi, L.; Tarantino, L.; Papa, V.; Rinaldi, R.; D'Alessandro, R.; Zavatta, M.; Laus, M.; Lattanzi, G.; et al. Satellite cell characterization from aging human muscle. *Neurol. Res.* **2010**, *32*, 63–72. https://doi.org/10.1179/174313209x385725.

Cortelli, G.; Patruno, L.; Cramer, T.; Murgia, M.; Fraboni, B.; De Miranda, S. Atomic force microscopy nanomechanics of hard nanometer-thick films on soft substrates: Insights into stretchable conductors. *ACS Appl. Nano Mater.* **2021**, *4*(8), 8376–8382. https://doi.org/10.1021/acsanm.1c00163.

Cosgrove, B.D.; Mui, K.L.; Driscoll, T.P.; Caliari, S.R.; Mehta, K.D.; Assoian, R.K.; Burdick, J.A.; Mauck, R.L. N-cadherin adhesive interactions modulate matrix mechanosensing and fate commitment of mesenchymal stem cells. *Nat. Mater.* **2016**, *15*, 1297–1306. https://doi.org/10.1038/nmat4725.

Costa, R.; Rodia, M.T.; Vianello, S.; Santi, S.; Lattanzi, G.; Angelini, C.; Pegoraro, E.; Cenacchi, G. Transportin 3 (TNPO3) and related proteins in limb girdle muscular dystrophy D2 muscle biopsies: A morphological study and pathogenetic hypothesis. *Neuromuscul. Disord.* **2020**, *30*, 685–692. https://doi.org/10.1016/j.nmd.2020.05.006.

Cronin, E.M.; Thurmond, F.A.; Bassel-Duby, R.; Williams, R.S.; Wright, W.E.; Nelson, K.D.; Garner, H.R. Protein-coated poly(L-lactic acid) fibers provide a substrate for differentiation of human skeletal muscle cells. *J. Biomed. Mater. Res.* **2004**, *69A*, 373–381. https://doi.org/10.1002/jbm.a.30009.

Das, R.; Curry, E.J.; Le, T.T.; Awale, G.; Liu, Y.; Li, S.; Contreras, J.; Bednarz, C.; Millender, J.; Xin, X.; Rowe, D.; Emadi, S.; Lo, K.W.H.; Nguyen, T.D. Biodegradable nanofiber bone-tissue scaffold as remotely-controlled and self-powering electrical stimulator. *Nano Energy* **2020**, *76*, 105028. https://doi.org/10.1016/J.NANOEN.2020.105028.

de la Serna, I.L.; Ohkawa, Y.; Berkes, C.A.; Bergstrom, D.A.; Dacwag, C.S.; Tapscott, S.J.; Imbalzano, A.N. (2005). MyoD targets chromatin remodeling complexes to the myogenin locus prior to forming a stable DNA-bound complex. *Mol. Cell. Biol.* 25(10), 3997–4009. https://doi.org/10.1128/mcb.25.10.3997-4009.2005.

DiMasi, J.A.; Hansen, R.W.; Grabowski, H.G. The price of innovation: new estimates of drug development costs. *J. Health Econ.* **2003**, *22*, 151–185.

Dixon, D.T.; Gomillion, C.T. 3D-Printed conductive polymeric scaffolds with direct current electrical stimulation for enhanced bone regeneration. *J. Biomed. Mater. Res. Part B Appl. Biomater.* **2023**, *111*(7), 1351–1364. https://doi.org/10.1002/JBM.B.35239.

Dumont, N.A.; Bentzinger, C.F.; Sincennes, M.; Rudnicki, M.A. Satellite Cells and Skeletal Muscle Regeneration. In: Terjung, R. (Ed.) *Comprehensive Physiology*; Wiley, 2015; pp. 1027–1059. https://doi.org/10.1002/cphy.c140068.

Eberli, D.; Soker, S.; Atala, A.; Yoo, J.J. Optimization of human skeletal muscle precursor cell culture and myofiber formation in vitro. *Methods* **2009**, *47*, 98–103.

Edmondson, D.G.; et al. (1994). Myogenin and MRF4 are involved in the expression of muscle-specific genes. *Mol. Cell. Biol.* 14(9), 6180–6190.

El-Sherbiny, I.M.; Yacoub, M.H. Hydrogel scaffolds for tissue engineering: Progress and challenges. *Glob. Cardiol. Sci. Pract.* **2013**, *38*. https://doi.org/10.5339/gcsp.2013.38.

Emery, A.E.H. The muscular dystrophies. *Lancet* **2002**, *359*(9307), 687–695. https://doi.org/10.1016/S0140-6736(02)07815-7.

Engler, A.J.; Sen, S.; Sweeney, H.L.; Discher, D.E. Matrix elasticity directs stem cell lineage specification. *Cell* **2006**, *126*, 677–689. https://doi.org/10.1016/j.cell.2006.06.044.

Evans, D.J.R.; Britland, S.; Wigmore, P.M. Differential response of fetal and neonatal myoblasts to topographical guidance cues in vitro. *J. Cell Sci.* **1999**, *112*, 438–442. https://doi.org/10.1007/s004270050275.

Falcone, S. et al. N-WASP is required for Amphiphysin-2/BIN1-dependent nuclear positioning and triad organization in skeletal muscle and is involved in the pathophysiology of centronuclear myopathy. *EMBO Mol. Med.* **2014**, *6*, 1455–1475.

Frantz, C., Stewart, K. M., & Weaver, V. M. (2010). The extracellular matrix at a glance. *Journal of Cell Science*, 123(24), 4195–4200. https://doi.org/10.1242/jcs.023820.

Frontera, W. R., & Ochala, J. (2015). Skeletal muscle: A brief review of structure and function. *Behavior Genetics*, 45(2), 183–195. https://doi.org/10.1007/s00223-014-9915-y.

Furberg, C.D.; Pitt, B. Withdrawal of cerivastatin from the world market. *Curr. Control Trials Cardiovasc. Med.* **2001**, *2*(5), 205–207. https://doi.org/10.1186/cvm-2-5-205.

Gaebel, R.; Ma, N.; Liu, J.; Guan, J.; Koch, L.; Klopsch, C.; Gruene, M.; Toelk, A.; Wang, W.; Mark, P.; Wang, F.; Chichkov, B.; Li, W.; Steinhoff, G. Patterning human stem cells and endothelial cells with laser printing for cardiac regeneration. *Biomaterials* **2011**, *32*, 9218–9230. https://doi.org/10.1016/j.biomaterials.2011.08.071.

Gamez, J.; Navarro, C.; Andreu, A.L.; Fernandez, J.M.; Palenzuela, L.; Tejeira, S.; Fernandez-Hojas, R.; Schwartz, S.; Karadimas, C.; DiMauro, S.; Hirano, M.; Cervera, C. Autosomal dominant limb-girdle muscular dystrophy: a large kindred with evidence for anticipation. *Neurology* **2001**, *56*(4), 450–454. https://doi.org/10.1212/wnl.56.4.450.

Ganji, Y.; Li, Q.; Quabius, E.S.; Böttner, M.; Selhuber-Unkel, C.; Kasra, M. Cardiomyocyte behavior on biodegradable polyurethane/gold nanocomposite scaffolds under electrical stimulation. *Mater. Sci. Eng. C* **2016**, *59*, 10–18. https://doi.org/10.1016/J.MSEC.2015.09.074.

Georganopoulou, D.G.; Moisiadis, V.G.; Malik, F.A.; Mohajer, A.; Dashevsky, T.M.; Wuu, S.T.; Hu, C.K. A journey with LGMD: From protein abnormalities to patient impact. *Protein J.* **2021**, *40*, 466–488. https://doi.org/10.1007/s10930-021-10006-9.

Gibertini, S.; Ruggieri, A.; Saredi, S.; Salerno, F.; Blasevich, F.; Napoli, L.; Moggio, M.; Nigro, V.; Morandi, L.; Maggi, L.; Mora, M. Long term follow-up and further molecular and histopathological studies in the LGMD1F sporadic TNPO3-mutated patient. *Acta Neuropathol. Commun.* **2018**, *6*, 141. https://doi.org/10.1186/s40478-018-0648-4.

Gillies, A.R.; Lieber, R.L. Structure and function of the skeletal muscle extracellular matrix: Skeletal Muscle ECM. *Muscle Nerve* **2011**, *44*, 318–331. https://doi.org/10.1002/mus.22094.

Gorbe, A.; Becker, D.L.; Dux, L.; Krenacs, L.; Krenacs, T. In differentiating prefusion myoblasts, connexin43 gap junction coupling is upregulated before myoblast alignment and then reduced in post-mitotic cells. *Histochem.* **2005**, *125*, 705–716. https://doi.org/10.1007/s00418-005-0121-x.

Gorbe, A.; Becker, D.L.; Dux, L.; Stelkovics, E.; Krenács, L.; Bagdi, E.; Krenacs, T. Transient upregulation of connexin43 gap junctions and synchronized cell cycle control precede myoblast fusion in regenerating skeletal muscle in vivo. *Histochem.* **2005**, *123*, 573–583. https://doi.org/10.1007/s00418-004-0745-2.

Görlich, D.; Kutay, U. Transport between the cell nucleus and the cytoplasm. *Annu. Rev. Cell Dev. Biol.* **1999**. Available online: https://www.annualreviews.org

Gotti, C.; Sensini, A.; Fornaia, G.; Gualandi, C.; Zucchelli, A.; Focarete, M.L. Biomimetic hierarchically arranged nanofibrous structures resembling the architecture and the passive mechanical properties of skeletal muscles: A step forward toward artificial muscle. *Front. Bioeng. Biotechnol.* **2020**, *8*, 767. https://doi.org/10.3389/fbioe.2020.00767.

Grasman, J.M.; Zayas, M.J.; Page, R.L.; Pins, G.D. Biomimetic scaffolds for regeneration of volumetric muscle loss in skeletal muscle injuries. *Acta Biomater.* **2015**, *25*, 2–15. https://doi.org/10.1016/j.actbio.2015.07.038.

Gualandi, C.; Govoni, M.; Foroni, L.; Valente, S.; Bianchi, M.; Giordano, E.; Pasquinelli, G.; Biscarini, F.; Focarete, M.L. Ethanol disinfection affects physical properties and cell response of electrospun poly(l-lactic acid) scaffolds. *Eur. Polym. J.* **2012**, *48*, 2008–2018. https://doi.org/10.1016/j.eurpolymj.2012.09.016.

Guex, A.; Kocher, F.; Fortunato, G.; Körner, E.; Hegemann, D.; Carrel, T.; Tevaearai, H.; Giraud, M. Fine-tuning of substrate architecture and surface chemistry promotes muscle tissue development. *Acta Biomater.* **2012**, *8*, 1481–1489. https://doi.org/10.1016/j.actbio.2011.12.033.

Guillotin, B.; Souquet, A.; Catros, S.; Duocastella, M.; Pippenger, B.; Bellance, S.; Bareille, R.; Rémy, M.; Bordenave, L.; Amédée, J.; Guillemot, F. Laser assisted bioprinting of engineered tissue with high cell density and microscale organization. *Biomaterials* **2010**, *31*, 7250–7256. https://doi.org/10.1016/j.biomaterials.2010.05.055.

Gungor-Ozkerim, P.S.; Inci, I.; Zhang, Y.S.; Khademhosseini, A.; Dokmeci, M.R. Bioinks for 3D bioprinting: an overview. *Biomater. Sci.* **2018**, *6*, 915–946. https://doi.org/10.1039/C7BM00765E.

Guo, X. et al. In vitro differentiation of functional human skeletal myotubes in a defined system. *Biomater. Sci.* **2014**, *2*, 131–138.

Halper, J.; Kjaer, M. Basic components of connective tissues and extracellular matrix: elastin, fibrillin, fibulins, fibrinogen, fibronectin, laminin, tenascins and thrombospondins. *Adv. Exp. Med. Biol.* **2014**, *802*, 31–47. https://doi.org/10.1007/978-94-007-7893-1_3.

Han, W.M.; Jang, Y.C.; García, A.J. Engineered matrices for skeletal muscle satellite cell engraftment and function. *Matrix Biol.* **2017**, *60–61*, 96–109. https://doi.org/10.1016/j.matbio.2016.06.001.

Hardy, J.G.; Cornelison, R.C.; Sukhavasi, R.C.; Saballos, R.J.; Vu, P.; Kaplan, D.L.; Schmidt, C.E. Electroactive Tissue Scaffolds with Aligned Pores as Instructive Platforms for Biomimetic Tissue Engineering. *Bioengineering* **2015**, *2*(1), 15–34. https://doi.org/10.3390/BIOENGINEERING2010015.

Hardy, J.G.; Geissler, S.A.; Aguilar, D.; Villancio-Wolter, M.K.; Mouser, D.J.; Sukhavasi, R.C.; Cornelison, R.C.; Tien, L.W.; Preda, R.C.; Hayden, R.S.; Chow, J.K.; Nguy, L.; Kaplan, D.L.; Schmidt, C.E. Instructive Conductive 3D Silk Foam-Based Bone Tissue Scaffolds Enable Electrical Stimulation of Stem Cells for Enhanced Osteogenic Differentiation. *Macromol. Biosci.* **2015**, *15*(11), 1490–1496. https://doi.org/10.1002/MABI.201500171.

Hardy, J.G.; Sukhavasi, R.C.; Aguilar, D.; Villancio-Wolter, M.K.; Mouser, D.J.; Geissler, S.A.; Nguy, L.; Chow, J.K.; Kaplan, D.L.; Schmidt, C.E. Electrical stimulation of human mesenchymal stem cells on biomineralized conducting polymers enhances their differentiation towards osteogenic outcomes. *J. Mater. Chem. B* **2015**, *3*(41), 8059–8064. https://doi.org/10.1039/C5TB00714C.

Harrison, R.G. The outgrowth of the nerve fiber as a mode of protoplasmic movement. *J. Exp. Zool.* **1959**, *142*, 5–73. https://doi.org/10.1002/jez.1401420103.

Hernández-Hernández, J.M.; García-González, E.G.; Brun, C.E.; Rudnicki, M.A. The myogenic regulatory factors, determinants of muscle development, cell identity and regeneration. *Semin. Cell Dev. Biol.* **2017**, *72*, 10–18. https://doi.org/10.1016/j.semcdb.2017.11.010.

Huang, N.F.; Patel, S.; Thakar, R.G.; Wu, J.; Hsiao, B.S.; Chu, B.; Lee, R.J.; Li, S. Myotube assembly on nanofibrous and micropatterned polymers. *Nano Lett.* **2006**, *6*, 537–542. https://doi.org/10.1021/nl060060o.

Hauschka, S.D.; Konigsberg, I.R. The influence of collagen on the development of muscle clones. *Proc. Natl. Acad. Sci. USA* **1966**, *55*(1), 119–126. https://doi.org/10.1073/pnas.55.1.119.

Holmes, A.M.; Creton, S.; Chapman, K. Working in partnership to advance the 3Rs in toxicity testing. *Toxicology* **2010**, *267*(1–3), 14–19. https://doi.org/10.1016/J.TOX.2009.11.006.

Hospodiuk, M.; Dey, M.; Sosnoski, D.; Ozbolat, I.T. The bioink: A comprehensive review on bioprintable materials. *Biotechnol. Adv.* **2017**, *35*, 217–239. https://doi.org/10.1016/j.biotechadv.2016.12.006.

Huxley, H.; Hanson, J. Changes in the cross-striations of muscle during contraction and stretch and their structural interpretation. *Nature* **1954**, *173*(4412), 973–976. https://doi.org/10.1038/173973a0.

Jeong, S.I.; Kim, B.-S.; Kang, S.W.; Kwon, J.H.; Lee, Y.M.; Kim, S.H.; Kim, Y.H. In vivo biocompatibility and degradation behavior of elastic poly(l-lactide-co-ε-caprolactone) scaffolds. *Biomaterials* **2004**, *25*, 5939–5946. https://doi.org/10.1016/j.biomaterials.2004.01.057.

Judson, R.N.; Rossi, F.M.V. Towards stem cell therapies for skeletal muscle repair. *NPJ Regen. Med.* **2020**, *5*, 10. https://doi.org/10.1038/s41536-020-0094-3.

Jun, I.; Jeong, S.; Shin, H. The stimulation of myoblast differentiation by electrically conductive sub-micron fibers. *Biomaterials* **2009**, *30*(11), 2038–2047. https://doi.org/10.1016/J.BIOMATERIALS.2008.12.063.

Kaji, H.; Ishibashi, T.; Nagamine, K.; Kanzaki, M.; Nishizawa, M. Electrically induced contraction of C2C12 myotubes cultured on a porous membrane-based substrate with muscle tissue-like stiffness. *Biomaterials* **2010**, *31*(27), 6981–6986. https://doi.org/10.1016/J.BIOMATERIALS.2010.05.071.

Kang, M.S.; Lee, S.H.; Park, W.J.; Lee, J.E.; Kim, B.; Han, D.-W. Advanced techniques for skeletal muscle tissue engineering and regeneration. *Bioengineering* **2020**, *7*, 99. https://doi.org/10.3390/bioengineering7030099.

Kapałczyńska, M.; Kolenda, T.; Przybyła, W.; Zajączkowska, M.; Teresiak, A.; Filas, V.; Ibbs, M.; Bliźniak, R.; Łuczewski, Ł.; Lamperska, K. 2D and 3D Cell Cultures—A Comparison of Different Types of Cancer Cell Cultures. Arch. Med. Sci. 2018, 14, 910–919. https://doi.org/10.5114/aoms.2016.63743

Khademhosseini, A.; Langer, R.; Borenstein, J.; Vacanti, J.P. Microscale technologies for tissue engineering and biology. *Proc. Natl. Acad. Sci. USA* **2006**, *103*, 2480–2487. https://doi.org/10.1073/pnas.0507681102.

Kovanen, V. Intramuscular extracellular matrix: complex environment of muscle cells. *Exerc. Sport Sci. Rev.* **2002**, *30*, 20–25. https://doi.org/10.1097/00003677-200201000-00005.

Kozeka, K.; Ontell, M. (1981). The three-dimensional cytoarchitecture of developing murine muscle spindles. *Dev. Biol.* 87.

Krewski, D.; Acosta, D.; Andersen, M.; Anderson, H.; Bailar, J.C.; Boekelheide, K.; Brent, R.; Charnley, G.; Cheung, V.G.; Green, S.; Kelsey, K.T.; Kerkvliet, N.I.; Li, A.A.; McCray, L.; Meyer, O.; Patterson, R.D.; Pennie, W.; Scala, R.A.; Solomon, G.M.; Zeise, L. Toxicity testing in the 21st century: a vision and a strategy. *J. Toxicol. Environ. Health Part B* **2010**, *13*(2–4), 51–138. https://doi.org/10.1080/10937404.2010.483176.

Kwee, B.J.; Mooney, D.J. Biomaterials for skeletal muscle tissue engineering. *Curr. Opin. Biotechnol.* **2017**, *47*, 16–22. https://doi.org/10.1016/j.copbio.2017.05.003.

Lai, M.-C.; Lin, R.-I.; Tarn, W.-Y. Transportin-SR2 mediates nuclear import of phosphorylated SR proteins. *Proc. Natl. Acad. Sci. USA* **2001**, *28*(18). https://doi.org/10.1073/pnas.181354098.

Langelaan, M.L.P.; Boonen, K.J.M.; Rosaria-Chak, K.Y.; van der Schaft, D.W.J.; Post, M.J.; Baaijens, F.P.T. Advanced maturation by electrical stimulation: Differences in response between C2C12 and primary muscle progenitor cells. *J. Tissue Eng. Regenerative Med.* 2011, 5, 529–539. https://doi.org/10.1002/TERM.345.

Langer, R.; Vacanti, J.P. Tissue engineering. *Science* **1993**, *260*, 920–926. https://doi.org/10.1126/science.8493529

Lee, J.M.; Suen, S.K.Q.; Ng, W.L.; Ma, W.C.; Yeong, W.Y. Bioprinting of collagen: Considerations, potentials, and applications. *Macromol. Biosci.* 2021, 21.

Lev, R.; Seliktar, D. Hydrogel biomaterials and their therapeutic potential for muscle injuries and muscular dystrophies. *J. R. Soc. Interface* 2018, 15, 20170380. https://doi.org/10.1098/rsif.2017.0380.

Lemarié, L.; Anandan, A.; Petiot, E.; Marquette, C.; Courtial, E.-J. Rheology, simulation and data analysis toward bioprinting cell viability awareness. *Bioprinting* 2021, 21, e00119.

Li, H.; Wen, F.; Wong, Y.S.; Boey, F.Y.C.; Subbu, V.S.; Leong, D.T.; Ng, K.W.; Ng, G.K.L.; Tan, L.P. Direct laser machining-induced topographic pattern promotes up-regulation of myogenic markers in human mesenchymal stem cells. *Acta Biomater.* 2011, 8, 531–539. https://doi.org/10.1016/j.actbio.2011.09.029.

Lin, J.C.; Tarn, W.Y. RBM4 down-regulates PTB and antagonizes its activity in muscle cell-specific alternative splicing. *J. Cell Biol.* **2011**, *193*, 509–520. https://doi.org/10.1083/jcb.201007131

Lin, J.-C.; Tarn, W.-Y. Multiple roles of RBM4 in muscle cell differentiation. *Front. Biosci.* **2012**, *4*.

Liu, J.; Saul, D.; Böker, K.O.; Ernst, J.; Lehman, W.; Schilling, A.F. Current methods for skeletal muscle tissue repair and regeneration. *BioMed Res. Int.* 2018, 1–11. https://doi.org/10.1155/2018/1984879.

Madden, L.; Juhas, M.; Kraus, W. E.; Truskey, G. A.; Bursac, N. Bioengineered Human Myobundles Mimic Clinical Responses of Skeletal Muscle to Drugs. *eLife* 2015, 4, e04885. https://doi.org/10.7554/eLife.04885.

Maertens, G.N.; Cook, N.J.; Wang, W.; Hare, S.; Gupta, S.S.; Öztop, I.; Lee, K.E.; Pye, V.E.; Cosnefroy, O.; Snijders, A.P.; Ramani, V.N.K.; Fassati, A.; Engelman, A.; Cherepanov, P. Structural basis for nuclear import of splicing factors by human Transportin 3. *Proc. Natl. Acad. Sci. USA* **2014**, *111*, 2728–2733. https://doi.org/10.1073/pnas.1320755111.

Maffioletti, S.M. et al. Three-dimensional human iPSC-derived artificial skeletal muscles model muscular dystrophies and enable multilineage tissue engineering. *Cell Rep.* 2018, 23, 899–908.

Mandrycky, C.; Wang, Z.; Kim, K.; Kim, D.H. 3D bioprinting for engineering complex tissues. *Biotechnol. Adv.* **2016**, *34*, 422–434. https://doi.org/10.1016/j.biotechadv.2015.12.011.

Martínez, E.; Lagunas, A.; Mills, C.; Rodríguez-Seguí, S.; Estévez, M.; Oberhansl, S.; Comelles, J.; Samitier, J. Stem cell differentiation by functionalized micro- and nanostructured surfaces. *Nanomedicine* 2009, 4, 65–82. https://doi.org/10.2217/17435889.4.1.65.

Mathur, A.B.; Collinsworth, A.M.; Reichert, W.M.; Kraus, W.E.; Truskey, G.A. Endothelial, cardiac muscle and skeletal muscle exhibit different viscous and elastic properties as determined by atomic force microscopy. *J. Biomech.* 2001, 34, 1545–1553. https://doi.org/10.1016/s0021-9290(01)00149-x.

Mauro, A. Satellite cell of skeletal muscle fibers. *J. Cell Biol.* 1961, 9, 493–495. https://doi.org/10.1083/jcb.9.2.493.

McClure, M.J.; Ramey, A.N.; Rashid, M.; Boyan, B.D.; Schwartz, Z. Integrin-α7 signaling regulates connexin 43, M-cadherin, and myoblast fusion. *Am. J. Physiol. Cell Physiol.* 2019, 316, C876–C887. https://doi.org/10.1152/ajpcell.00282.2018.

McGreevy, J.W.; Hakim, C.H.; McIntosh, M.A.; Duan, D. Animal models of Duchenne muscular dystrophy: From basic mechanisms to gene therapy. *Dis. Model. Mech.* 2015, 8, 195–213.

Melià, M.J.; Kubota, A.; Ortolano, S.; Vílchez, J.J.; Gámez, J.; Tanji, K.; Bonilla, E.; Palenzuela, L.; Fernández-Cadenas, I.; Pristoupilová, A.; García-Arumí, E.; Andreu, A.L.; Navarro, C.; Hirano, M.; Martí, R. Limb-girdle muscular dystrophy 1F is caused by a microdeletion in the transportin 3 gene. *Brain* 2013, 136, 1508–1517. https://doi.org/10.1093/brain/awt074.

Meriggioli, M.N.; Roubenoff, R. Prospect for pharmacological therapies to treat skeletal muscle dysfunction. *Behav. Genet.* 2015, 45, 234–242. https://doi.org/10.1007/S00223-014-9926-8/FIGURES/2.

Mertens, J.P.; Sugg, K.B.; Lee, J.D.; Larkin, L.M. Engineering muscle constructs for the creation of functional engineered musculoskeletal tissue. *Regen. Med.* 2014, 9, 89–100. https://doi.org/10.2217/rme.13.81.

Mills, R.J. et al. Development of a human skeletal micro muscle platform with pacing capabilities. *Biomaterials* 2019, 198, 217–227.

Moncaut, N.; Rigby, P.W.J.; Carvajal, J.J. (2013). Dial M(RF) for myogenesis. *FEBS J.* 280(17), 3980–3990. https://doi.org/10.1111/febs.12379.

Motohashi, N., Asakura, Y., & Asakura, A. (2014). Isolation, culture, and transplantation of muscle satellite cells. *Journal of Visualized Experiments*, 85. https://doi.org/10.3791/50846.

Mukherjee, S.; Gualandi, C.; Focarete, M.L.; Ravichandran, R.; Venugopal, J.R.; Raghunath, M.; Ramakrishna, S. Elastomeric electrospun scaffolds of poly(l-lactide-co-trimethylene carbonate) for myocardial tissue engineering. *J. Mater. Sci. Mater. Med.* 2011, 22, 1689–1699. https://doi.org/10.1007/s10856-011-4351-2.

Mukund, K., & Subramaniam, S. (2020). Skeletal muscle: A review of molecular structure and function, in health and disease. *Wiley Interdisciplinary Reviews: Systems Biology and Medicine*, 12(1). https://doi.org/10.1002/wsbm.1462.

Murphy, S.V.; Atala, A. 3D bioprinting of tissues and organs. *Nat. Biotechnol.* 2014, 32, 773–785. https://doi.org/10.1038/nbt.2958.

Naidu, P.S.; Ludolph, D.; To, R.; Hinterberger, T.; Konieczny, S.F. Myogenin and MEF2 function synergistically to activate the MRF4 promoter during myogenesis. *Mol. Cell Biol.* 1995, 15, 2707–2718.

Narayanan, N.; Jiang, C.; Wang, C.; Uzunalli, G.; Whittern, N.; Chen, D.; Jones, O.G.; Kuang, S.; Deng, M. Harnessing fiber diameter-dependent effects of myoblasts toward biomimetic scaffold-based skeletal muscle regeneration. *Front. Bioeng. Biotechnol.* 2020, 8, 203. https://doi.org/10.3389/fbioe.2020.00203.

Nigro, V.; Aurino, S.; Piluso, G. (2011). Limb girdle muscular dystrophies: Update on genetic diagnosis and therapeutic approaches. *Curr. Opin. Neurol.* 24(5), 429–436. https://doi.org/10.1097/WCO.0b013e32834aa38d

Norwood, F.L.M.; Harling, C.; Chinnery, P.F.; Eagle, M.; Bushby, K.; Straub, V. (2009). Prevalence of genetic muscle disease in Northern England: in-depth analysis of a muscle clinic population. *Brain* 132(11), 3175–3186. https://doi.org/10.1093/brain/awp236

O'Connell, C.D.; Zhang, B.; Onofrillo, C.; Duchi, S.; Blanchard, R.; Quigley, A.; Bourke, J.; Gambhir, S.; Kapsa, R.; Di Bella, C.; Choong, P.; Wallace, G.G. Tailoring the mechanical properties

of gelatin methacryloyl hydrogels through manipulation of the photocrosslinking conditions. *Soft Matter* 2018, 14, 2142–2151.

Ostrovidov, S.; Shi, X.; Sadeghian, R.B.; Salehi, S.; Fujie, T.; Bae, H.; Ramalingam, M.; Khademhosseini, A. Stem cell differentiation toward the myogenic lineage for muscle tissue regeneration: A focus on muscular dystrophy. *Stem Cell Rev. Rep.* **2015**, *11*, 866–884. https://doi.org/10.1007/s12015-015-9618-4.

Ozbolat, I.T. Scaffold-based or scaffold-free bioprinting: Competing or complementing approaches? *J. Nanotechnol. Eng. Med.* 2015, 6, 024701. https://doi.org/10.1115/1.4030414.

Pacilio, S.; Costa, R.; Papa, V.; Rodia, M.T.; Gotti, C.; Pagnotta, G.; Cenacchi, G.; Focarete, M.L. Electrospun Poly(L-lactide-co-ε-caprolactone) scaffold potentiates C2C12 myoblast bioactivity and acts as a stimulus for cell commitment in skeletal muscle myogenesis. *Bioengineering* 2023, 10, 239. https://doi.org/10.3390/BIOENGINEERING10020239.

Pagnotta, G.; Graziani, G.; Baldini, N.; Maso, A.; Focarete, M.L.; Berni, M.; Biscarini, F.; Bianchi, M.; Gualandi, C. Nanodecoration of electrospun polymeric fibers with nanostructured silver coatings by ionized jet deposition for antibacterial tissues. *Mater. Sci. Eng. C* 202

Patel, K.H.; Dunn, A.J.; Talovic, M.; Haas, G.J.; Marcinczyk, M.; Elmashhady, H.; Kalaf, E.G.; Sell, S.A.; Garg, K. Aligned nanofibers of decellularized muscle ECM support myogenic activity in primary satellite cells in vitro. *Biomed. Mater.* **2019**, *14*, 035010. https://doi.org/10.1088/1748-605x/ab0b06.

Penning, J.; Dijkstra, H.; Pennings, A. Preparation and properties of absorbable fibres from l-lactide copolymers. *Polymer* **1993**, *34*, 942–951. https://doi.org/10.1016/0032-3861(93)90212-s.

Pham, Q.P.; Sharma, U.; Mikos, A.G. Electrospun Poly(ε-caprolactone) Microfiber and Multilayer Nanofiber/Microfiber Scaffolds: Characterization of Scaffolds and Measurement of Cellular Infiltration. *Biomacromolecules* **2006**, *7*, 2796–2805. https://doi.org/10.1021/bm060680j.

Pieri, A.; Byerley, A.M.; Musumeci, C.R.; Salemizadehparizi, F.; Vanderhorst, M.A.; Wuertz-Kozak, K. Electrospinning and 3D bioprinting for intervertebral disc tissue engineering. *JOR Spine* **2020**. https://doi.org/10.1002/jsp2.1117.

Pires, F.; Ferreira, Q.; Rodrigues, C.A.V.; Morgado, J.; Ferreira, F.C. Neural stem cell differentiation by electrical stimulation using a cross-linked PEDOT substrate: Expanding the use of biocompatible conjugated conductive polymers for neural tissue engineering. *Biochim. Biophys. Acta* **2015**, *1850*(6), 1158–1168. https://doi.org/10.1016/J.BBAGEN.2015.01.020.

Potthoff, M.J.; Olson, E.N. (2007). MEF2: A central regulator of diverse developmental programs. *Development* 134(23), 4131–4140. https://doi.org/10.1242/dev.008367

Poyatos-García, J.; Blázquez-Bernal, Á.; Selva-Giménez, M.; Bargiela, A.; Espinosa-Espinosa, J.; Vázquez-Manrique, R.P.; Bigot, A.; Artero, R.; Vilchez, J.J. CRISPR-Cas9 Editing of a TNPO3 Mutation in a Muscle Cell Model of Limb-Girdle Muscular Dystrophy Type D2. *Mol. Ther. Nucleic Acids* **2023**, *31*, 324–338. doi:10.1016/j.omtn.2023.01.004.

Prabhakaran, M.P.; Ghasemi-Mobarakeh, L.; Jin, G.; Ramakrishna, S. Electrospun conducting polymer nanofibers and electrical stimulation of nerve stem cells. *J. Biosci. Bioeng.* **2011**, *112*(5), 501–507. https://doi.org/10.1016/J.JBIOSC.2011.07.010.

Puertas-Bartolomé, M.; Mora-Boza, A.; García-Fernández, L. Emerging Biofabrication Techniques: A Review on Natural Polymers for Biomedical Applications. *Polymers* **2021**, *13*, 1209. https://doi.org/10.3390/polym13081209.

Qian, H.; Bei, J.; Wang, S. Synthesis, characterization and degradation of ABA block copolymer of l-lactide and ε-caprolactone. *Polym. Degrad. Stab.* **2000**, *68*, 423–429. https://doi.org/10.1016/s0141-3910(00)00031-8.

Rezvani Ghomi, E.; Nourbakhsh, N.; Akbari Kenari, M.; Zare, M.; Ramakrishna, S. Collagen-based biomaterials for biomedical applications. *J. Biomed. Mater. Res. B Appl. Biomater.* **2021**, *109*, 1986–1999.

Rudnicki, M.A.; Jaenisch, R. The MyoD family of transcription factors and skeletal myogenesis. *BioEssays* **1995**, *17*, 203–209. https://doi.org/10.1002/bies.950170306.

Isaac, R.; Gomes Reis, F.C.; Ying, W.; Olefsky, J.M. Exosomes as mediators of intercellular crosstalk in metabolism. *Cell Metab.* **2021**.

Sanes, J.R. The Basement Membrane/Basal Lamina of Skeletal Muscle. *J. Biol. Chem.* **2003**, *278*, 12601–12604. https://doi.org/10.1074/jbc.r200027200.

Sandmann, T.; Jensen, L.J.; Jakobsen, J.S.; Karzynski, M.M.; Eichenlaub, M.P.; Bork, P.; Furlong, E.E. A temporal map of transcription factor activity: mef2 directly regulates target genes at all stages of muscle development. *Dev. Cell* **2006**, *10*(6), 797–807. https://doi.org/10.1016/j.devcel.2006.04.009.

Schindelin, J.; Arganda-Carreras, I.; Frise, E.; Kaynig, V.; Longair, M.; Pietzsch, T.; Preibisch, S.; Rueden, C.; Saalfeld, S.; Schmid, B.; et al. Fiji: An open-source platform for biological-image analysis. *Nat. Methods* **2012**, *9*, 676–682. https://doi.org/10.1038/nmeth.2019.

Schmidt, M.; Schüler, S.C.; Hüttner, S.S.; von Eyss, B.; von Maltzahn, J. Adult stem cells at work: regenerating skeletal muscle. *Cell. Mol. Life Sci.* **2019**, *76*, 2559–2570. https://doi.org/10.1007/s00018-019-03093-6.

Semplicini, C.; Bertolin, C.; Bello, L.; Pantic, B.; Guidolin, F.; Vianello, S.; Catapano, F.; Colombo, I.; Moggio, M.; Gavassini, B.F.; et al. The clinical spectrum of CASQ1-related myopathy. *Neurology* **2018**, *91*, e1629–e1641. https://doi.org/10.1212/wnl.0000000000006387.

Sensini, A.; Santare, M.H.; Eichenlaub, E.; Bloom, E.; Gotti, C.; Zucchelli, A.; Cristofolini, L. Tuning the Structure of Nylon 6,6 Electrospun Bundles to Mimic the Mechanical Performance of Tendon Fascicles. *Front. Bioeng. Biotechnol.* **2021**, *9*, 626433. https://doi.org/10.3389/fbioe.2021.626433.

Scharner, J.; Zammit, P.S. The muscle satellite cell at 50: The formative years. *Skelet. Muscle* **2011**, *1*, 28. https://doi.org/10.1186/2044-5040-1-28.

Schwab, A.; Levato, R.; D'Este, M.; Piluso, S.; Eglin, D.; Malda, J. Printability and Shape Fidelity of Bioinks in 3D Bioprinting. *Chem. Rev.* **2020**, *120*, 11028–11055.

Seale, P.; Asakura, A.; Rudnicki, M.A. The Potential of Muscle Stem Cells. *Dev. Cell* **2001**, *1*, 333–342. https://doi.org/10.1016/S1534-5807(01)00049-1.

Sirivisoot, S.; Harrison, B.S. Skeletal myotube formation enhanced by electrospun polyurethane carbon nanotube scaffolds. *Int. J. Nanomed.* **2011**, *6*, 2483–2497. https://doi.org/10.2147/IJN.S24073.

Shirahama, H.; Lee, B.H.; Tan, L.P.; Cho, N.-J. Precise Tuning of Facile One-Pot Gelatin Methacryloyl (GelMA) Synthesis. *Sci. Rep.* **2016**, *6*, 31036.

Smith, A.S.T.; et al. A multiplexed chip-based assay system for investigating the functional development of human skeletal myotubes in vitro. *J. Biotechnol.* **2014**, *185*, 15–18.

So, J.Y.; Lee, J.; Ahn, Y.; Kang, D.; Jung, W.; Bae, W.G. The synergistic effect of biomimetic electrical stimulation and extracellular-matrix-mimetic nanopattern for upregulating cell activities. *Biosens. Bioelectron.* **2020**, *167*, 112470. https://doi.org/10.1016/J.BIOS.2020.112470.

Sordini, L.; Garrudo, F.F.F.; Rodrigues, C.A.V.; Linhardt, R.J.; Cabral, J.M.S.; Ferreira, F.C.; Morgado, J. Effect of electrical stimulation conditions on neural stem cells differentiation on cross-linked PEDOT films. *Front. Bioeng. Biotechnol.* **2021**, *9*, 591838. https://doi.org/10.3389/fbioe.2021.591838.

Sorushanova, A.; Delgado, L.M.; Wu, Z.; Shologu, N.; Kshirsagar, A.; Raghunath, R.; Mullen, A.M.; Bayon, Y.; Pandit, A.; Raghunath, M.; Zeugolis, D.I. The collagen suprafamily: From biosynthesis to advanced biomaterial development. *Adv. Mater.* **2019**, *31*, 1801651. https://doi.org/10.1002/adma.201801651.

Srinivasan, S.P.; Neef, K.; Treskes, P.; Liakopoulos, O.J.; Stamm, C.; Cowan, D.B.; Madershahian, N.; Kuhn, E.; Slottosch, I.; Wittwer, T.; et al. Enhanced gap junction expression in myoblast-containing engineered tissue. *Biochem. Biophys. Res. Commun.* **2012**, *422*, 462–468. https://doi.org/10.1016/j.bbrc.2012.05.016.

Ström, A.-C.; Weis, K. Importin-like nuclear transport receptors. *Genome Biol.* **2001**, *2*(6), reviews/3008. https://doi.org/10.1186/gb-2001-2-6-reviews-3008.

Suzuki, K.; Brand, N.J.; Allen, S.; Khan, M.A.; Farrell, A.O.; Murtuza, B.; El Oakley, R.; Yacoub, M.H. Overexpression of connexin 43 in skeletal myoblasts: Relevance to cell transplantation to the heart. *J. Thorac. Cardiovasc. Surg.* **2001**, *122*, 759–766. https://doi.org/10.1067/mtc.2001.116210.

Takahashi, H.; Shimizu, T.; Okano, T. Engineered human contractile myofiber sheets as a platform for studies of skeletal muscle physiology. *Sci. Rep.* **2018**, *8*, 1–11. https://doi.org/10.1038/s41598-018-23523-9.

Tajbakhsh, S. (2009). Skeletal muscle stem cells in developmental versus regenerative myogenesis. *Journal of Internal Medicine*, 266(4), 372–389. https://doi.org/10.1111/j.1365-2796.2009.02158.x.

Tandon, N.; Cannizzaro, C.; Chao, P.H.G.; Maidhof, R.; Marsano, A.; Au, H.T.H.; Radisic, M.; Vunjak-Novakovic, G. Electrical stimulation systems for cardiac tissue engineering. *Nat. Protoc.* **2009**, *4*, 155–173. https://doi.org/10.1038/nprot.2008.183.

Theocharis, A. D., Skandalis, S. S., Gialeli, C., & Karamanos, N. K. (2016). Extracellular matrix structure. *Advanced Drug Delivery Reviews*, 97, 4–27. https://doi.org/10.1016/j.addr.2015.11.001.

Tian, S.; Zhao, H.; Lewinski, N. Key parameters and applications of extrusion-based bioprinting. *Bioprinting* **2021**, *23*, e00156. https://doi.org/10.1016/j.bprint.2021.e00156.

Torella, A.; Fanin, M.; Mutarelli, M.; Peterle, E.; Del Vecchio Blanco, F.; Rispoli, R.; Savarese, M.; Garofalo, A.; Piluso, G.; Morandi, L.; Ricci, G.; Siciliano, G.; Angelini, C.; Nigro, V. Next-generation sequencing identifies transportin 3 as the causative gene for LGMD1F. *PLoS One* **2013**, *8*, e83800. https://doi.org/10.1371/journal.pone.0083800.

Turner, N.J.; Badylak, S.F. Regeneration of skeletal muscle. *Cell Tissue Res.* **2012**, *347*, 759–774. https://doi.org/10.1007/s00441-011-1185-7.

Ulery, B.D.; Nair, L.S.; Laurencin, C.T. Biomedical applications of biodegradable polymers. *J. Polym. Sci. Part B: Polym. Phys.* **2011**, *49*, 832–864. https://doi.org/10.1002/polb.22259.

Vacanti, C.A. The history of tissue engineering. *J. Cell. Mol. Med.* **2006**, *10*, 569–576. https://doi.org/10.1111/j.1582-4934.2006.tb00421.x.

Van der Kooi, A.J. (2017). Limb-Girdle Muscular Dystrophy: The Genetic Landscape. *Nature Reviews Neurology*, 13(4), 220–221. https://doi.org/10.1038/nrneurol.2017.9

Vandenburgh, H. et al. Drug-screening platform based on the contractility of tissue-engineered muscle. *Muscle Nerve* **2008**, *37*, 438–447. https://doi.org/10.1002/mus.20933.

Vandenburgh, H. et al. Automated drug screening with contractile muscle tissue engineered from dystrophic myoblasts. *FASEB J.* **2009**, *23*, 3325–3334. https://doi.org/10.1096/fj.09-136077.

Velleman, S.G. The role of the extracellular matrix in skeletal development. *Poultry Sci.* **2000**, *79*, 985–989. https://doi.org/10.1093/ps/79.7.985.

Venturino, I.; Vurro, V.; Bonfadini, S.; Moschetta, M.; Perotto, S.; Sesti, V.; Criante, L.; Bertarelli, C.; Lanzani, G. Skeletal muscle cells opto-stimulation by intramembrane molecular transducers. *Commun. Biol.* **2023**, *6*, 1–11. https://doi.org/10.1038/s42003-023-05538-y.

Vihinen, P., & Kähäri, V. M. (2002). Matrix metalloproteinases in cancer: Prognostic markers and therapeutic targets. *International Journal of Cancer*, 99(2), 157–166. https://doi.org/10.1002/ijc.10329.

Wang, L.; Wu, Y.; Guo, B.; Ma, P. X. Nanofiber Yarn/Hydrogel Core–Shell Scaffolds Mimicking Native Skeletal Muscle Tissue for Guiding 3D Myoblast Alignment, Elongation, and Differentiation. *ACS Nano* 2015, 9, 9167–9179. https://doi.org/10.1021/acsnano.5b03290.

Witt, S.H.; Granzier, H.; Witt, C.C.; Labeit, S. MURF-1 and MURF-2 Target a Specific Subset of Myofibrillar Proteins Redundantly: Towards Understanding MURF-Dependent Muscle Ubiquitination. *J. Mol. Biol.* **2005**, *350*(4), 713–722. doi:10.1016/j.jmb.2005.05.021.

Wu, T.; Zhang, J.; Wang, Y.; Sun, B.; Guo, X.; Morsi, Y.; El-Hamshary, H.; El-Newehy, M.; Mo, X. Development of Dynamic Liquid and Conjugated Electrospun Poly(L-lactide-co-caprolactone)/Collagen Nanoyarns for Regulating Vascular Smooth Muscle Cells Growth. *J. Biomed. Nanotechnol.* **2017**, *13*, 303–312. https://doi.org/10.1166/jbn.2017.2352.

Yang, D.; Faraz, F.; Wang, J.; Radacsi, N. Combination of 3D Printing and Electrospinning Techniques for Biofabrication. *Adv. Mater. Technol.* **2022**, *7*, 2101309. https://doi.org/10.1002/admt.202101309.

Zammit, P.S. (2017). Function of the myogenic regulatory factors Myf5, MyoD, Myogenin and MRF4 in skeletal muscle, satellite cells and regenerative myogenesis. *Semin. Cell Dev. Biol.* 72, 19–32. https://doi.org/10.1016/j.semcdb.2017.11.011

Zhang, W.; Liu, Y.; Zhang, H. Extracellular Matrix: An Important Regulator of Cell Functions and Skeletal Muscle Development. *Cell Biosci.* **2021**, *11*, 65. https://doi.org/10.1186/s13578-021-00579-4.

Zhang, M.; Zhu, B.; Davie, J. Alternative Splicing of MEF2C Pre-mRNA Controls Its Activity in Normal Myogenesis and Promotes Tumorigenicity in Rhabdomyosarcoma Cells. *J. Biol. Chem.* **2015**, *290*, 310–324. https://doi.org/10.1074/jbc.m114.606277.

Zhao, C.; Wu, Z.; Chu, H.; Wang, T.; Qiu, S.; Zhou, J.; Zhu, Q.; Liu, X.; Quan, D.; Bai, Y. Thiol-Rich Multifunctional Macromolecular Crosslinker for Gelatin-Norbornene-Based Bioprinting. *Biomacromolecules* **2021**, *22*, 2729–2739. https://doi.org/10.1021/acs.biomac.1c00134.

Zheng, Z.; Eglin, D.; Alini, M.; Richards, G.R.; Qin, L.; Lai, Y. Visible light-induced 3D bioprinting technologies and corresponding bioink materials for tissue engineering: A review. *Engineering* 2021, *7*, 966–978. https://doi.org/10.1016/j.eng.2020.05.021.